Nanoscale Spectroscopic Imaging of Carriers and Heat in Photocatalysts

Thesis by

Levi D. Palmer

In Partial Fulfillment of the Requirements for
the degree of
Doctor of Philosophy in Chemistry

CALIFORNIA INSTITUTE OF TECHNOLOGY
Pasadena, California

2026
(Defended April 8, 2026)

Levi D. Palmer
ORCID: 0000-0002-7228-4263

ACKNOWLEDGEMENTS

This work is a testament to my friends and family who uplifted me before and throughout this Ph.D. You all believed in me even when I did not always believe in myself. This work is dedicated to me and you, and it is a reminder of the things we can achieve together. You gave me the courage to dream big and aim for the stars.

In many ways, growing up in rural Minnesota was unique. The tight-knit, small-town atmosphere provided, for some, a rich sense of community designed as a solid foundation for our careers. I want to thank Mrs. Angela Klein for teaching me to be an excellent writer, Ganley's for giving me a strong work ethic, and BSA Troop 102 for showing me nature's beauty. Most importantly, I want to thank Pastor Clint M. Evans. I will always remember the many times you said, "don't forget me when you win the Nobel Prize." You inspire my curiosity. Although this is not the Nobel Prize, we will get there one day! I miss you, brother.

I need to thank my undergraduate research advisor, Professor Renee R. Frontiera, for taking me under her wing. You helped me not only think deeply and creatively about research, but also to discover my own life goals and passions. Thank you, Dr. Kajari Bera, for encouraging me to email Renee (multiple times) as my Gen. Chem. TA! Your belief in me changed my trajectory and connected me with Dr. James Brooks. Jamie, thank you for being the kindest and most patient mentor. I learned many analytical skills from you including data analysis and the scientific method. I still laugh at the time during group meeting when I said we did an experiment to "prove" our hypothesis and everyone shouted in unison "TEST" because we can always be wrong. Thank you to the entire Frontiera Lab, especially Dr. Bailey Nebgen, for your lasting friendship.

Many friends and mentors in my undergraduate years inspired my goals of earning a Ph.D. I want to highlight my college roommate, Jake Ellingson, for showing your dedication to science and learning. Your pure enjoyment of science and ceaseless work ethic have always amazed me. And thank you to Professor Harry Atwater, Professor Giulia Tagliabue, the Atwater Lab, and the Amgen Cohort for a dream summer in California.

Moving to California alone during COVID-19 was both exciting and frightening. It often felt like I aimlessly started a new life. I owe a lot to the entire Cushing Lab for being more than a laboratory and more like a home. Thank you to Drs. Hanzhe Liu, Jonathan Michelson, and Danika Nimlos for being my initial mentors and friends. Thank you to Professor Ye-Jin Kim for teaching me the practical aspects of UEM and for always being willing to give feedback on my work and future directions. You inspire me to take big risks and to tackle grand challenges. I was honored to meet your lab and friends in Korea, and my mom and I were grateful for your hospitality. Thank you to my cohort Dr. Emily Hwang, Dr. Nathan Harper, Hamilton Evans, and Wonseok Lee for learning and growing with me. Most importantly, thank you to Wonseok for supporting me every day. You were by my side to troubleshoot quite literally every research question and to hear every one of my frustrations and celebrations on this journey. Thank you to Jocelyn Mendes and Nicholas Heller for your emotional support and friendship. I still remember when we virtually recruited you during the pandemic and convinced you to join the Cushing Lab! Thank you to Amy Lin, Audrey Washington, and Natan Spear for your fun and energetic spirits. You fostered a positive, inclusive, and engaging lab dynamic to cultivate a supportive environment for mentees. The future of the Cushing Lab is incredibly bright, and I am proud of my first-year mentees, Claude Zheng and Kevin Alexander for their early successes. Your excitement, curiosity, and eagerness have been reinvigorating in my final months at Caltech. You remind me of the reasons I want to be a PI, and I am wishing you all the best in your Ph.Ds.

Outside the Cushing Lab, I am grateful for many friends who supported me and my personal growth. The CCID and PRISM, especially Devon and Taso, brought energy and life to campus. You helped make Caltech feel more human, rather than the scientific humanoid reality that exists in Caltech's bubble. When deciding between different graduate schools, I knew that you would be a critical support system for me at Caltech. Also, thank you to Dr. Prashant Bhat, Dr. Josh Zak, Dr. Alex Winnett, and Natasha Reich, Zac Chase, and Dr. Madeline Meier for the fun retreats, nights out, and community. Prashant, you have been in my corner since day one, always keeping me motivated but also ready to have fun at any moment. You are the most diligent person I have ever met, and your work is really paying off! I am so proud of you and look forward to your continued success.

I am also thankful for the teamwork and friends I met through the Liquid Sunlight Alliance and the Ensembles of Photosynthetic Nanoreactors. Your connection helped me look forward to every Zoom meeting, conference, and All-Hands event. I am proud of all the students and postdocs doing incredible things—Drs. Katie Luedecke, Marija Zorich, Justin Bui, Kyra Yap, Frank Alcorn, Colton Sheehan, Allison Smith, Jennifer Urbine, and John Mangum. You amaze me, and I'm thankful to have learned so much from you while having fun. Thank you to the LiSA and EPN PIs for being wonderful and supportive, especially Drs. Annie Greenaway, Emily Warren, John Gregoire, A. Alec Talin, and Prof. Joe Patterson. I am also incredibly thankful to the entire solar fuels and microscopy communities, which are filled with the most collaborative, kind, and engaging people. This includes our DOE program managers who made my Ph.D. research possible through various funding opportunities.

I want to thank my advisor, Professor Scott Cushing, for actively choosing to create the best lab culture on campus. Your joyfully unfiltered mindset oftentimes gave me the courage to take big risks and fail because I knew that I wouldn't be judged if I missed the mark. The entire lab is thankful for you and proud of your great successes. I still laugh at the time you told us to be more positive during recruitment because you said, "WE'RE RICH!" and we needed to act like it. Your successes and mentality are an inspiration. Thank you for offering endless opportunities for career/life advice, even starting in my undergraduate years.

To my Argonne National Laboratory mentor, Dr. Tom Gage—you are unbelievably talented, fun, and down-to-earth! Thank you for teaching me the ins-and-outs of electron microscopy. Your mentorship was pivotal in my Ph.D. and set me on a new path. You amplified my scientific impact and helped me discover a lot about myself and my science. Thank you for managing the incredible resources at CNM and for being a great friend and mentor.

I would also like to thank my thesis committee, Professors Ryan Hadt, Brian Stoltz, and Shane Ardo, for their emotional support and career advice. Looking back at my candidacy report years later was truly humbling, so I thank you for your patience and guidance. You were always so flexible, even meeting over Zoom last-minute when I got food poisoning. I need to give an extra shoutout to Prof. Shane Ardo for commuting up to Caltech for every

meeting. While balancing family time on top of directing our research center, you actively saved the planet by turning the world EPN Blue. Thank you all for your recommendations—you set me up for success in my next journey!

Patrick, you carried me through this Ph.D. and kept me grounded every day. You have been teaching me to be my biggest cheerleader, rather than just my biggest critic. I am inspired by your focus and devotion to your craft. I rely on your positive drive like a crutch. Thank you for your patience and your generosity for everyone around you, and thank you for being the best daddy to our kitties, Pumpkin and Mango Kiwi Coconutter. You are the loves of my life and the lights in my world.

Lastly, I would not have made it here without my family. I wish every day that we lived closer together, but you never cease to support me from across the country. I love you all more than I can describe. Mom and Dad, thank you for raising me to work hard and be courteous to others. You provided the foundation, home, and community that made me who I am today. Thank you, Abigail and Sonja, for being the best sisters ever. You are always there when I need a good laugh or cry. You do the most for me, even while working unbelievably hard on your separate endeavors. To all my cousins, aunts, and uncles—I love you and am grateful for your wholehearted support of my authenticity. Thank you for getting lunches with me on campus, always hosting the best parties, and even housing me for short periods of time. Finally, to my grandparents, I love you. Grandma Mabel and Grandpa Floyd, thank you for raising the most incredible four women who each support me endlessly. Especially Grandma, thank you for teaching me good judgement in adulthood. You inspire me to be my best self by taking care of others, being a good host, and leading with compassion. Grandma Joyce, you were the gentlest explorer. Thank you for always sharing the best stories and for teaching me to be grounded in myself and my values.

ABSTRACT

Photoexcited carriers (electrons and holes) perform photocatalytic solar energy conversion reactions when they transfer from a solid-state material and into a nearby or surface-adsorbed molecule. For example, light-driven water splitting occurs when a photocatalyst produces molecular hydrogen and oxygen from water because electron transfer drives hydrogen evolution, whereas hole transfer drives oxygen evolution. These photoexcited carriers often get trapped at nanoscale features such as dopants, defects, and grain boundaries, limiting their mobility and potentially reducing photocatalytic efficiency. However, identifying which nanoscale properties hinder solar energy conversion remains a key challenge as this requires a technique that can separately image carriers and photothermal heating on the timescale relevant to photocatalysis. Here, we develop photomodulated electron energy-loss spectroscopy (EELS) in the scanning transmission electron microscope (STEM) to map photocarrier and heat distributions at sub-nanometer length scales. This dissertation presents the experimental and computational developments critical for photomodulated STEM-EELS development. We first introduce EELS and the fundamental working principles of ultrafast and optically coupled TEM. We demonstrate the theoretical framework needed to differentiate carriers from photothermal heating in two systems: plasmonic core-shell nanoparticles and crystalline silicon. Then, we apply this method to image photoexcited carriers localized at surface oxygen vacancies and along select nanoparticle facets in water-splitting strontium titanate photocatalysts. We lastly perform optically coupled liquid phase TEM (LPTEM) of similar photocatalytic nanoparticles in carbon film liquid cells, aiming to expand this technique to operando measurements of photocatalysts in their working conditions. Overall, this thesis demonstrates photomodulated STEM-EELS as a tool for imaging photocatalytic structure–function relationships down to the atomic scale.

PUBLISHED CONTENT AND CONTRIBUTIONS

1) Palmer, L. D.; Lee, W.; Prasad, P. R.; Layne, B. W.; Wu, H.-H.; Chen, Z.; Wen, J.; Liu, Y.; Pan, X.; Talin, A. A.; Kudo, A.; Ardo, S.; Patterson, J. P.; Gage, T. E.; Cushing, S. K. Imaging nanoscale photocarrier traps in solar water splitting catalysts. Ver. 1. *arXiv*, Dec 31, 2025. https://doi.org/10.48550/arXiv.2512.24543.

   L.D.P. helped conceive the project, conducted all experiments, led the data analysis, wrote the manuscript, and prepared the figures.

2) Lee, W.†; Palmer, L. D.†; Gage, T. E.; Cushing, S. K. Imaging Nanoscale Carrier, Thermal, and Structural Dynamics with Time-Resolved and Ultrafast Electron Energy-Loss Spectroscopy. *Chem. Phys. Rev.* **2025**, *6*, 041303. https://doi.org/10.1063/5.0289128.

   L.D.P. helped conceive the project, performed all computations, supported the manuscript writing, and prepared the figures.

3) Palmer, L. D.; Lee, W.; Durham, D. B.; Fajardo, J., Jr.; Liu, Y.; Talin, A. A.; Gage, T. E.; Cushing, S. K. Nanoscale and Element-Specific Lattice Temperature Measurements using Core-Loss Electron Energy-Loss Spectroscopy. *ACS Phys. Chem. Au* **2025**, *5* (6), 589–598. https://doi.org/10.1021/acsphyschemau.5c00044.

   L.D.P. helped conceive the project, conducted all experiments, performed all computations, performed all data analysis, wrote the manuscript, and prepared the figures.

4) Palmer, L. D.; Lee, W.; Dong, C.L.; Liu, R.-S.; Wu, N.; Cushing, S. K. Determining Quasi-Equilibrium Electron and Hole Distributions from Plasmonic Photocatalysts using Photomodulated X-ray Absorption Spectroscopy. *ACS Nano* **2024**, *18* (13), 9344–9353. https://doi.org/10.1021/acsnano.3c08181.

   L.D.P. performed the data analysis and theory, wrote the manuscript, and prepared the figures.

5) Kim, Y.-J.; Palmer, L. D.; Lee, W.; Heller, N. J.; Cushing, S. K. Using electron energy-loss spectroscopy to measure nanoscale electronic and vibrational dynamics in a TEM. *J. Chem. Phys.* **2023**, *159*, 050901. https://doi.org/10.1063/5.0147356.

   L.D.P. wrote sections I, II, V; performed the computations; and prepared figures 1–7.

6) Palmer, L. D.†, Zheng, Y.†, Zhang, X., Alexander, K. H., Lee, W., Chen, J., Gage, T. E., Cushing, S. K. Optically Coupled Liquid-Phase Electron Microscopy and Thermometry of Light-Driven Water Evaporation. **2026**, In Preparation.

   L.D.P. helped conceive the project, supported all data collection, led the data analysis, wrote the initial draft of the manuscript's main text, prepared the figures.

TABLE OF CONTENTS

LIST OF FIGURES

LIST OF TABLES

NOMENCLATURE

a-C. Amorphous Carbon.

a-C:H. Hydrogenated Amorphous Carbon.

BSE. Bethe–Salpeter Equation.

CBM. Conduction Band Minimum.

CCD. Charge-Coupled Device.

CDEM. Charge Dynamics Electron Microscopy.

CMOS. Complementary Metal–Oxide–Semiconductor.

cDFPT. Constrained Density Functional Perturbation Theory.

DFPT. Density Functional Perturbation Theory.

DFT. Density Functional Theory.

DOS. Density of States.

e-Beam. Electron Beam.

EEG. Electron Energy-Gain.

EELS. Electron Energy-Loss Spectroscopy.

EFTEM. Energy-Filtered Transmission Electron Microscopy.

ELNES. Energy-Loss Near-Edge Structure.

EM. Electron Microscopy.

EM. Electromagnetic.

ETEM. Environmental TEM.

EXELFS. Extended Energy-Loss Fine Structure.

fs.	Femtosecond.
FWHM.	Full Width at Half Maximum.
LL.	Liouville–Lanczos.
LPTEM.	Liquid Phase TEM.
LSP.	Localized Surface Plasmon.
ns.	Nanosecond.
OCEAN.	Obtaining Core Excitations from the Ab initio electronic structure and the NIST BSE solver.
PEET.	Plasmon Energy Expansion Thermometry.
PINEM.	Photon-Induced Near-Field Electron Microscopy.
ps.	Picosecond.
q-EELS.	Momentum-Resolved EELS.
Quantum ESPRESSO.	Quantum Open-Source Package for Research in Electronic Structure, Simulation, and Optimization.
RF.	Radio Frequency.
SBR.	Signal-to-Background Ratio.
SNR.	Signal-to-Noise Ratio.
STEM.	Scanning Transmission Electron Microscopy.
TDDFPT.	Time-Dependent Density Functional Perturbation Theory.
TDDFT.	Time-Dependent Density Functional Theory.
TEM.	Transmission Electron Microscopy.
THz.	Terahertz.
Tr-q-EELS.	Time- and Momentum-Resolved Electron Energy-Loss Spectroscopy.
UED.	Ultrafast Electron Diffraction.

UEM. Ultrafast Electron Microscopy.

UV-VIS. Ultraviolet-Visible.

VASP. Vienna Ab initio Simulation Package.

VBM. Valence Band Maximum.

XAS. X-ray Absorption Spectroscopy.

XUV. Extreme Ultraviolet.

ZLP. Zero-Loss Peak.

CHAPTER 1

INTRODUCTION

Adapted with permission from the following:

Kim, Y.-J.; Palmer, L. D.; Lee, W.; Heller, N. J.; Cushing, S. K. Using electron energy-loss spectroscopy to measure nanoscale electronic and vibrational dynamics in a TEM. *J. Chem. Phys.* **2023**, *159*, 050901. https://doi.org/10.1063/5.0147356.

Lee, W.[†]; Palmer, L. D.[†]; Gage, T. E.; Cushing, S. K. Imaging Nanoscale Carrier, Thermal, and Structural Dynamics with Time-Resolved and Ultrafast Electron Energy-Loss Spectroscopy. *Chem. Phys. Rev.* **2025**, 6, 041303. https://doi.org/10.1063/5.0289128.

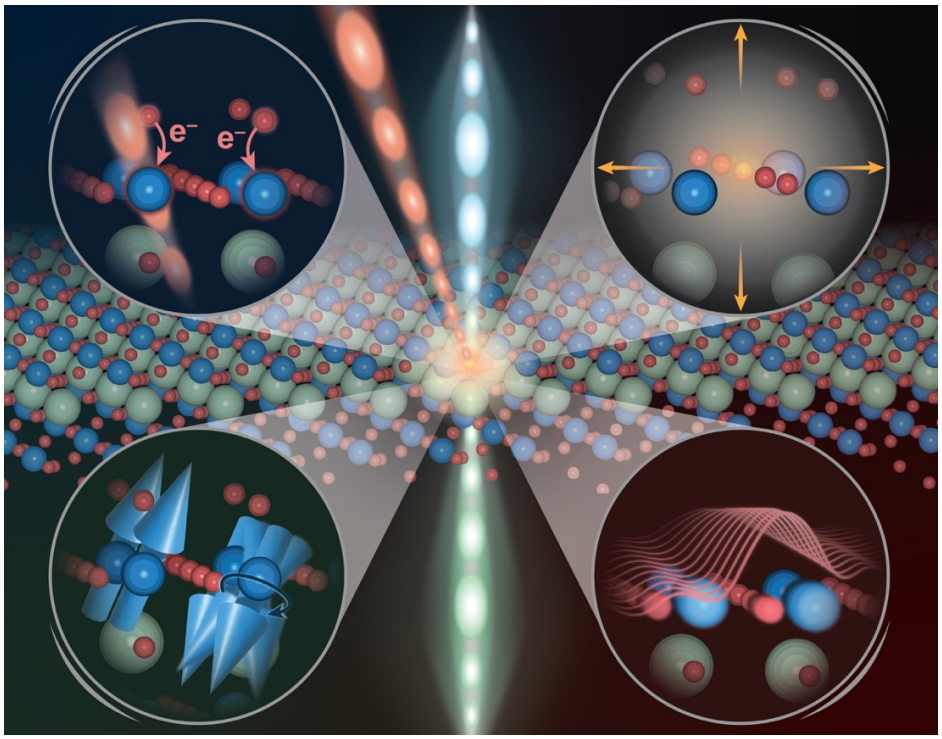

1.1 The Transmission Electron Microscope

The transmission electron microscope (TEM) is an instrument with inherent atomic-scale resolution, making it one of the most powerful tools available for characterizing the structural, chemical, and electronic properties of materials. Technological advancements in electron optics, specifically aberration correctors, from 2000–2010 have enabled these sub-angstrom resolutions.[1] In a TEM, a beam of high-energy electrons is typically accelerated to 60–300 keV before transmitting through a specimen. The specimen inelastically and elastically scatters the beam, and the resulting signals are used to form images, diffraction patterns, or spectra with sub-angstrom spatial resolution. An aberration-corrected TEM's footprint is typically 2.5–3 m in height and composed of a column of vacuum chambers. The microscope can be modified to allow specimen and/or gun photoexcitation for optically coupled TEM or ultrafast electron microscopy (UEM) (**Fig. 1.1**).[2]

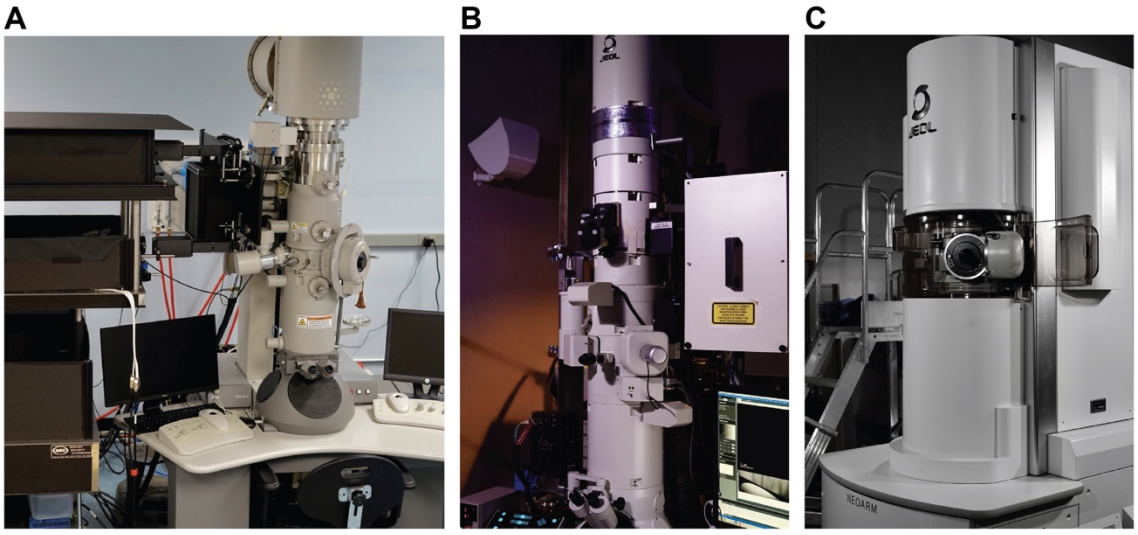

Figure 1.1. Images of optically coupled TEMs. (**A**) An original FEI Tecnai Femto prototype, branded as UEM-2, refurbished from Nobel Laureate Ahmed Zewail's laboratory. (**B**) A JEOL JEM-2100 Plus microscope with IDES ultrafast pulsing and specimen photoexcitation. (**C**) A JEOL NEOARM microscope with the IDES Luminary Micro specimen photoexcitation system.

TEMs are complex instruments that contain numerous electron lenses, apertures, and detectors all working synchronously (**Fig. 1.2**). The electromagnetic lenses shape and focus the electrons by applying a Lorentz force on the moving charged particles. The condenser lenses control the beam size and convergence angle at the specimen. Post-specimen objective lensing provides the primary image-forming stage, and projector lenses further magnify the transmitted beam onto the detectors. In scanning TEM (STEM) mode, scan coils raster a focused probe across the specimen, enabling data acquisition at each probe position. The apertures control the beam's coherence, current, or local acquisition. Multi-pole correctors adjust spherical (C*s*) aberrations and have pushed imaging resolution from angstrom to picometer scales, reaching the inherent thermal atomic vibration limit.[3,4]

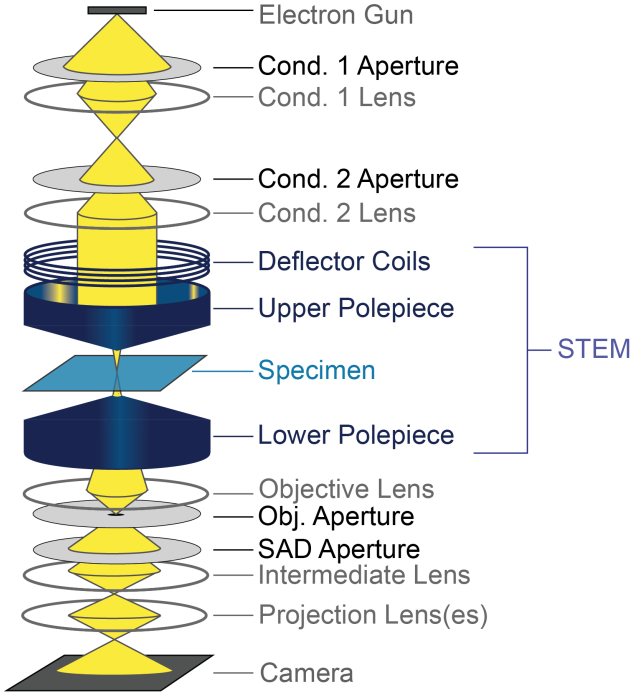

Figure 1.2. Electron optics in the S/TEM. Free electrons (yellow) are emitted and accelerated from an electron gun at the top of the microscope, shown here. The condenser (cond.) aperture and lenses help focus and shape the beam. Deflector coils scan the beam in STEM mode; descan coils are not depicted for clarity. After the specimen, the electrons are further collected and projected for various detection and imaging methods. The objective (obj.) aperture can optionally be inserted to block diffracted electrons and improve image

contrast. The selected area diffraction (SAD) aperture can be inserted to pass electrons from select specimen regions. A camera used for bright-field imaging and diffraction is shown; here, the direct beam is detected in the image plane.

The TEM's electron emission mechanism strongly influences the imaging coherence and electron energy-loss spectroscopy (EELS) resolution. Free electrons are generated inside the electron gun from a cathode via either thermionic or field emission (**Fig. 1.3A**). Thermionic guns heat a filament (commonly tungsten or LaB_6) to 2000–3000 K, producing a broad thermal distribution of electrons with bandwidths of 0.7–1.5 eV FWHM. Schottky emitters operate at lower temperatures (~1800 K) in the presence of a strong electric field, reducing the spectral bandwidth to 0.5–1.1 eV. Cold field emission guns (cFEGs) employ a nanostructured tungsten tip at ambient temperature in a strong electric field, enabling electron tunneling with the narrowest emission bandwidths (<0.5 eV) and highest coherence.[5,6] This improved spectral bandwidth fundamentally dictates the achievable EELS resolution. For reference, **Fig. 1.3B** estimates the energy ranges needed to measure select phenomena with EELS. Advanced TEMs often contain a high-current cFEG source with an electron monochromator to probe millielectronvolt phenomena such as atomic vibrations.

1.2 Electron Energy-Loss Spectroscopy (EELS)

Electron energy-loss spectroscopy (EELS) is performed by collecting electrons transmitted through a specimen and dispersing their energies using a magnetic prism spectrometer.[7,8] Many electrons that pass through the specimen scatter elastically, largely by diffraction. The largest feature in a thin specimen's EEL spectrum is the elastically scattered zero-loss peak (ZLP) at 0 eV (**Fig. 1.4**). The ZLP is used for aligning and calibrating the EELS energy, as its full width at half-maximum (FWHM) defines the EELS energy resolution. The more interesting features in EELS probe inelastically scattered electrons that transferred energy and momentum to the specimen by exciting a range of potential quasiparticle and electronic transitions. EELS excitations are broadly divided into two spectral regimes: low-loss and core-loss.

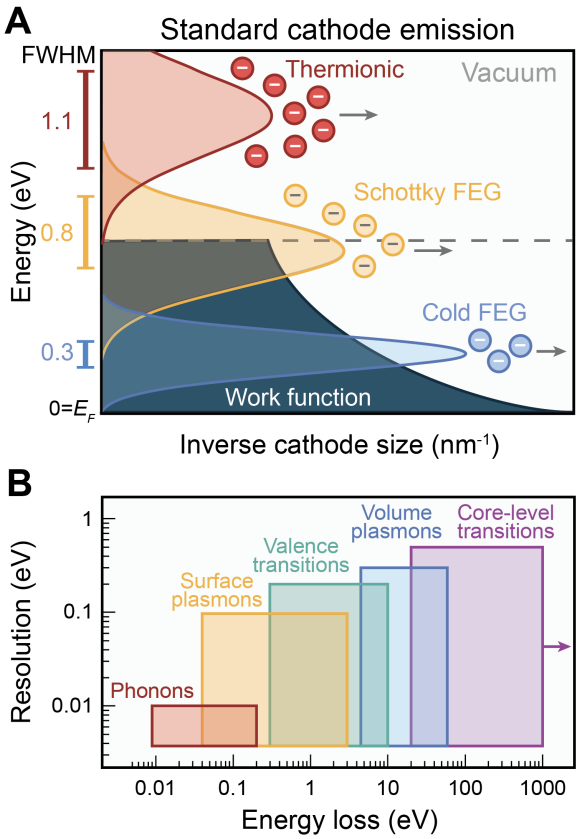

Figure 1.3. Cathode types and EELS resolutions. (**A**) Energy resolution of an electron beam versus inverse cathode size. A thermionic gun or field emission gun, FEG, generates an electron distribution in vacuum by extracting electrons around the Fermi level (E_F). The average emission bandwidth (FWHM) of each cathode is determined by its work function, which decreases as the size of the cathode decreases. The dashed line depicts the bulk work function. (**B**) The energy loss region and required energy resolution associated for elucidating select dynamics with EELS. Each excitation's fine structure peak separation and spectral bandwidth determine the resolution required for acquisition.

EELS can image a material's steady-state electronic and chemical properties (**Fig. 1.4**).[9] This includes low-loss (<50 eV) excitations like phonons or vibrational mode,[10,11] bonding states,[12] surface plasmons,[13,14] and intra/interband transitions.[15,16] The core-loss region (approximately >50 eV) measures the oxidation state and local coordination of atoms similar to X-ray spectroscopy.[17,18] When EELS is performed in a scanning TEM (STEM) during

STEM-EELS, the spectroscopic vibrational and electronic and excitations are imaged at picometer-to-micrometer resolutions. Traditionally, the tradeoff of electron-based imaging and spectroscopy has been specimen damage, but low-dose and cryogenic imaging can mitigate damage to allow measurements of beam-sensitive systems such as molecules, soft polymers, and biological complexes.[19,20]

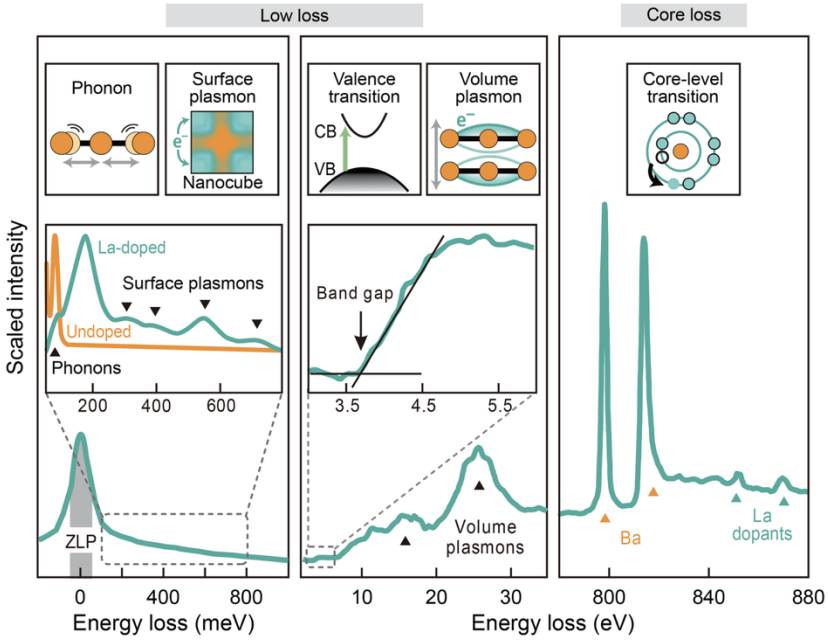

Figure 1.4. Monochromated EELS. EELS of a 5% La-doped $BaSnO_3$ nanocube (teal spectrum) shown in logarithmic vertical scale and schematics of the associated excitations probed. Phonons are visible in the spectrum of the undoped specimen (orange spectrum) and are otherwise screened by La dopants. Adapted from Ref. 9.

1.2.1 Low-Loss EELS Theory

Low-loss EELS largely probes a specimen's inter/intraband excitations and bulk plasmons. Low-energy phonons and surface plasmons are also measurable with monochromated, high-resolution EELS but are not within the scope of this thesis. Interpreting the complex electronic origin of low-loss EELS peaks is a significant challenge for most non-metallic and multi-element specimens. Also known as the loss function, low-loss EELS probes the negative imaginary component of the inverse dielectric function.[21,22] The loss function can

be directly expressed using the real (ϵ_1) and imaginary (ϵ_2) components of the dielectric function ($\epsilon = \epsilon_1 + \mathrm{i}\epsilon_2$) as:

$$\mathrm{Im}\left[-\frac{1}{\epsilon(\mathbf{q},\omega)}\right] = \frac{\epsilon_2}{\epsilon_1^2 + \epsilon_2^2}. \tag{1.1}$$

Physically, ϵ_1 represents the specimen's polarization when there is no absorption at that frequency, and ϵ_2 represents single-particle excitations (i.e., absorption). The loss function is therefore a direct reflection of the specimen's complex dielectric function as a function of momentum ($\mathbf{q}$) and frequency (ω). The TEM's free electron beam also induces longitudinal oscillations of the specimen's electron charge density. As a result, the loss function measures both the longitudinal (out-of-plane) and transverse (in-plane) components of the dielectric function. This unique sensitivity to longitudinal excitations enables EELS to probe dark or optically forbidden electronic transitions, as it is not constrained by the transverse dipole selection rules that apply to most optical spectroscopies.

As mentioned, low-loss EELS directly probes a plethora of excitations (e.g., vibrational modes, excitons, inter/intraband transitions, localized surface plasmons). In the low-loss energy range of approximately 5–50 eV, absorption features can become obscured by bulk plasmons, where the real part of the dielectric function becomes zero. These bulk plasmon peaks are generated when a specimen's free electron density is not polarizable and fails to screen the incoming electron beam's perturbation. As a result, either the valence or free electrons in the specimen oscillate.

The free electron and Drude models predict the loss function and the bulk plasmon energy (E_p) through the relation to its oscillation frequency (ω_p) and electron density (n):

$$E_p = \hbar\omega_p = \frac{h}{2\pi}\sqrt{\frac{ne^2}{m_e\epsilon_0}}. \tag{1.2}$$

Notably, the free electron model assumes electrons move freely in the specimen, which is a relatively accurate approximation for metals. Physical constants are Planck constant (h), the elementary charge (e), and the permittivity of free space (ε_0); the effective mass (m_e) can vary depending on the specimen.

The free electron model in **Eq. (1.2)** accurately captures the bulk plasmon energy in metals, where the absence of a bandgap permits conduction of the free electron gas.[23] In insulators, however, the free electron model breaks down because the loss function and E_p in **Eqs. (1.1)** and **(1.2)** are complicated by dielectric screening, excitons, and interband transitions. **Figure 1.5** depicts the complex dielectric function, loss function, and calculated plasmon energy for both a metal (aluminum) and insulator (hexagonal boron nitride).[24,25] The loss function was calculated *ab initio* using linearized time-dependent density functional theory (TDDFT).[26]

Figure 1.5B highlights the complexities of the loss function for insulators. Most notably, the Drude model fails to predict the loss function for insulating hBN, whereas an *ab initio* TDDFT approach produces a far more accurate result. The Drude model calculation was performed using the electron density for a standard Al and hBN unit cell. Further computational developments are needed to improve our understanding of insulators' loss functions, especially if attempting to use it as a means of resolving ultrafast carrier dynamics.

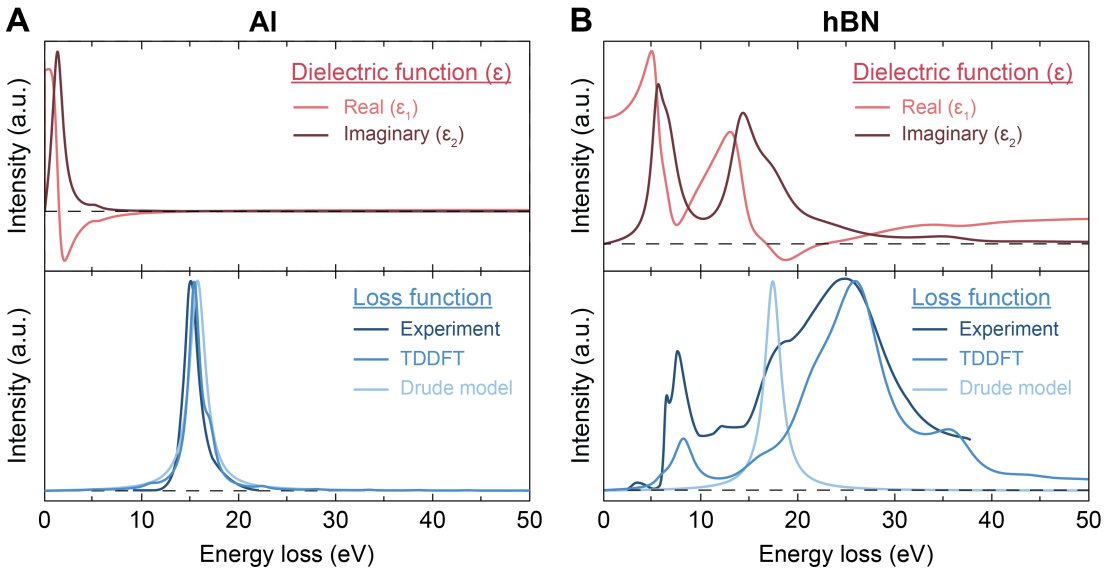

Figure 1.5. Comparing loss functions for a metal and an insulator. TDDFT-calculated dielectric function (top) and loss function (bottom) for (**A**) aluminum (Al) and (**B**) hexagonal boron nitride (hBN). The loss functions for each material are derived from first-principles TDDFT, the Drude model, and experiment. Al experiment adapted from Ref. 24. hBN experiment adapted from Ref. 25.

1.2.2 Core-Loss EELS Theory

The core-loss region of the EEL spectrum arises when incident electrons promote tightly bound core electrons into unoccupied states above the Fermi level. The fine structure of core-loss edges provides detailed information about materials' local electronic and crystalline structure. This fine structure near the edge onset, known as the energy-loss near-edge structure (ELNES), reflects the element-specific unoccupied density of states modified by core-hole effects, crystal field splitting, and chemical bonding. ELNES is directly analogous to the near-edge X-ray absorption fine structure (NEXAFS/XANES) measured by X-ray absorption spectroscopy (XAS). This thesis focuses on the ELNES region of core-loss EELS.

Core-loss EELS in a TEM now exceeds the combined spatial and energy resolutions of many comparable X-ray and synchrotron techniques. Modern aberration-corrected instruments equipped with cFEGs and electron monochromators enable core-loss measurements with <3 meV energy resolution and <40 pm spatial resolution.[27,28] These resolutions readily enable the identification of elemental distributions and oxidation states at single-atom dopant sites, interfaces, and defects. These measurements would otherwise be extremely difficult or impossible with X-ray spectroscopies that lack comparable spatial resolution and as such average over the spectral signatures of highly localized properties.

A key distinction between core-loss EELS and photon-based core-level spectroscopies is the momentum transfer (**q**) accessible to electrons (**Fig. 1.6**). Under the dipole approximation (small **q**), the EEL spectrum closely resembles an X-ray absorption spectrum. However, at larger momentum transfers, higher-order multipole contributions become significant, and transitions that are dipole-forbidden become observable. This allows core-loss EELS to probe a rich set of momentum-dependent excitations within a specimen's Brillouin zone.

Quantitative analysis of core-loss spectra is supported by *ab initio* simulation codes such as the OCEAN package, which solves the Bethe-Salpeter equation (BSE) to account for the core-hole/valence-electron exciton and many-body screening effects that govern the fine structure of core-level transitions.[29]

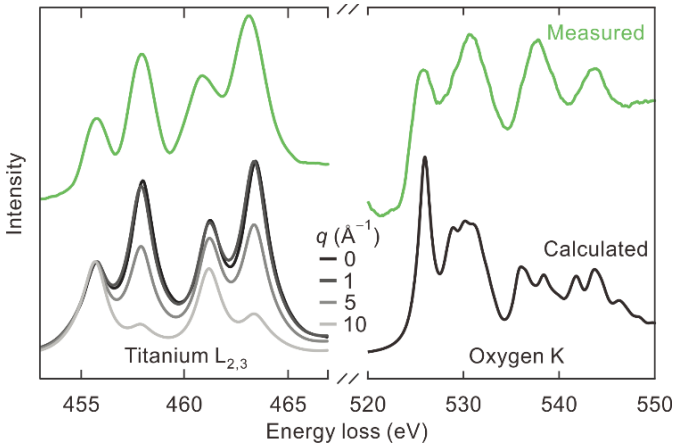

Figure 1.6. Measured and calculated EEL spectra of $SrTiO_3$. Measured EEL spectra (green) of $SrTiO_3$ nanoparticles are compared to OCEAN calculations (black). The spectra were acquired at small collection angles at zero momentum (q = 0 Å^{-1}) to match an X-ray absorption spectrum according to the dipole approximation. Finite momentum transfer is simulated as denoted in the legend. The measured spectrum was smoothed, and the calculated spectra were broadened to match the experiment.

For inelastic excitations outside of the bulk plasmon's energetic range, and at ultralow-loss and core-loss energies, the loss function is only dependent on the dielectric function's imaginary component.[30] As a result, an EEL spectrum is almost 1:1 comparable to infrared spectroscopy or XAS. The loss function in **Eq. 1.1** is therefore be represented by ϵ_2 for core-loss excitations because $\epsilon_1 \to 1$ and $\epsilon_2 \ll 1$:

$$\mathrm{Im}\left[-\frac{1}{\epsilon(\mathbf{q},\omega)}\right] = \frac{\epsilon_2}{\epsilon_1^2+\epsilon_2^2} \approx \epsilon_2(\mathbf{q},\omega). \tag{1.3}$$

We interpret Fermi's golden rule to understand the momentum dependence of core-loss EELS. Here, the transition rate $W_{i\to f}$ for a system transitioning from an initial state Ψ_i to a final state Ψ_f upon interaction with an incident electron of energy $\hbar\omega$ is given by **Eq. 1.4**:[31]

$$W_{i\to f} = \frac{2\pi}{\hbar}\left|\langle\Psi_f|\hat{T}|\Psi_i\rangle\right|^2\delta(E_f - E_i - \hbar\omega). \tag{1.4}$$

If we sum the transition rates across all potential initial (i) and final (f) states of the specimen's electronic structure, we readily relate **Eq. 1.3** and **1.4** as:

$$\epsilon_2(\mathbf{q},\omega) \propto \sum_{i,f} W_{i\to f}\,. \tag{1.5}$$

In **Eq. 1.4**, $\hat{T}$ is the transition operator for inelastic scattering, expressed as $\hat{T} = e^{\mathrm{i}\mathbf{q}\cdot\mathbf{r}}$. The delta function ($\delta$) accounts for energy conservation, indicating that the transition occurs when the energy of the final state (E_f) matches the energy of the initial state (E_i) plus the energy loss of probe electrons ($\hbar\omega$). The transition operator is alternatively expressed as through a Taylor series expansion:

$$\hat{T} = e^{\mathrm{i}\mathbf{q}\cdot\mathbf{r}} = 1 + \mathrm{i}\mathbf{q}\cdot\mathbf{r} - \frac{1}{2}(\mathbf{q}\cdot\mathbf{r})^2 + \cdots. \tag{1.6}$$

For small momentum transfer, higher-order terms can be neglected. Under the dipole approximation and assuming the initial core-level and final state wavefunctions are atomic-like, **Eq. 1.4** can be simplified as:

$$W_{i\to f} = \frac{2\pi}{\hbar}\left|\langle\Psi_f|\mathbf{q}\cdot\mathbf{r}|\Psi_i\rangle\right|^2\delta(E_f - E_i - \hbar\omega). \tag{1.7}$$

As a result, the core-loss EELS transition probability depends quadratically on the momentum vector, $\mathbf{q}$. These momentum-dependent excitations are probed by tilting the specimen or by sampling the q-vector in the specimen's diffraction plane.[25,32–34] Momentum-resolved EELS uniquely probes phonon and carrier dynamics within select Brillouin zones.

1.3 Ultrafast and Optically Coupled EELS

Until this point, Chapter 1 has primarily treated EELS as a probe of ground-state properties. In an optically coupled TEM, however, EELS can be extended into the time domain by using a laser pulse to drive the specimen out of equilibrium while a delayed electron pulse probes the photoinduced spectral changes. Ultrafast EELS directly probes how photoexcited dynamics shift and broaden low-loss and core-loss spectra. The temporal resolution is set by the pump–probe cross-correlation, timing jitter, and electron-pulse broadening. Different optically coupled TEM methods access unique photodynamics in semiconductors as shown in **Fig. 1.7**.

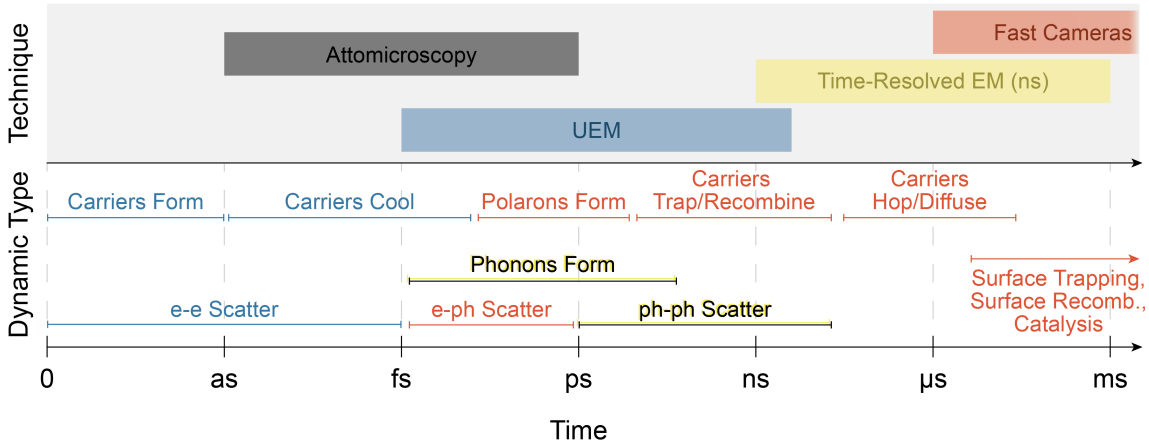

Figure 1.7. Optically coupled TEM techniques used to probe select photodynamics. (Top) Optically coupled TEM techniques each achieve unique temporal resolutions. (Bottom) Photoexcitation leads to a cascade of atomic processes and ultrafast dynamics. Purely electronic (blue), nuclear (yellow), and electron-nuclear coupled (red) dynamics are listed. The words electron and phonon are abbreviated as e and ph, respectively.

Attosecond-to-femtosecond dynamics are dominated by coherent optical field interactions, hot carrier generation, and electron–electron scattering. The first tens of attoseconds after specimen photoexcitation are so brief that even atomic nuclei are frozen in time, meaning phonons and molecular vibrations have not yet begun. To put these timescales into perspective, an attosecond is to a second, as a second is to approximately 31.7 billion years. As shown in **Fig. 1.7**, attomicroscopy is the only optically coupled TEM method able to

detect attosecond processes.[35,36] This emerging technique relies on attosecond optical gating of electron pulses, where a laser pulse effectively gates or chops the electron down to 625 as. Attomicroscopy is technically a sub-field of UEM, and attosecond EELS measurements have not yet been demonstrated.

In a standard UEM, femtosecond laser pulses photoexcite the specimen and photo-trigger the electron gun (**Figure 1.8A**).[37–39] A mechanical delay stage controls the time delay between the pump and probe pulses to acquire femtosecond – picosecond dynamics. Real-space imaging in a UEM can be correlated with reciprocal and energy spaces via diffraction and spectroscopy, respectively. Ultrafast EELS is an emerging technique for spectroscopic measurements of photodynamics at nanometer length scales. Ultrafast low-loss EELS is highly sensitive to photocarrier populations, dielectric screening, plasmonic response, and temperature.[40–42] Ultrafast core-loss EELS has been reported to probe transient thermal, bonding, and charge dynamics.[43–45] Future ultrafast EELS studies are equipped to probe electron–phonon scattering, phonon–phonon scattering, and the onset of carrier trapping or polaron formation.

We highlight the unique applications of EELS in the UEM for measuring ultrafast light-induced processes (**Figs. 1.8B–E**). For example, charge dynamics electron microscopy (CDEM) is one technique that probes local electromagnetic fields induced by charge dynamics at nanometer spatial and femtosecond temporal scales (**Fig. 1.8B**).[46,47] CDEM probes the charge dynamics as the electron beam is broadened and accelerated by charge-induced plasmas and THz fields. Ultrafast low-loss EELS has also been used to measure changes to a material's carrier density due to photoexcitation while capturing both the electronic and structural effects (**Fig. 1.8C**).[40–42] Demonstrations also utilize a q-slit to probe photoexcited scattering and relaxation processes in reciprocal space using momentum-resolved ultrafast EELS (**Fig. 1.8D**).[32] Lastly, ultrafast core-loss EELS can accurately probe changes in the chemical bonding and coordination geometry of a material caused by photoexcitation, such as charge transfer and lattice changes (**Fig. 1.8E**).[43–45]

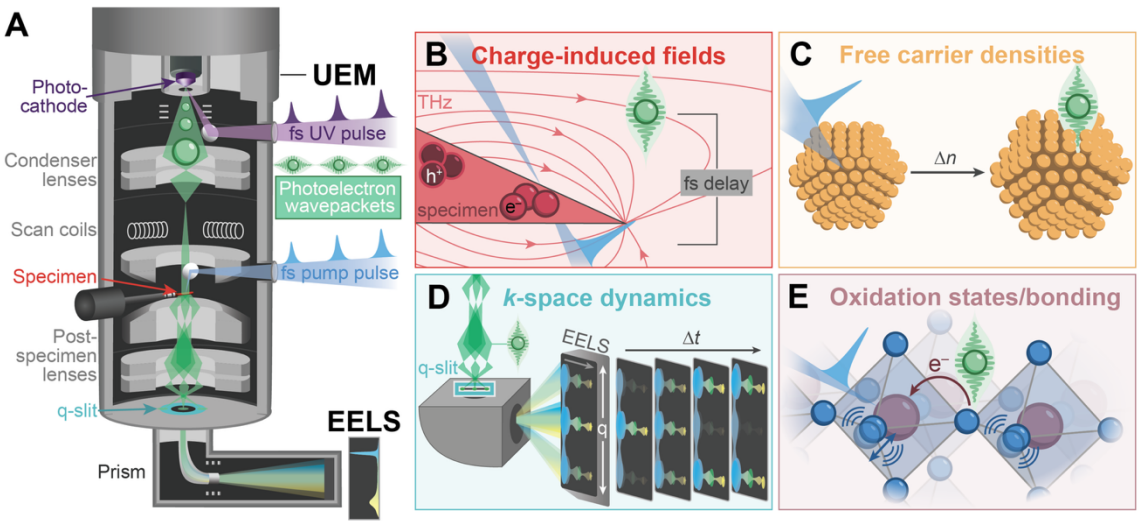

Figure 1.8. Time-resolved and ultrafast electron energy-loss spectroscopy (EELS) in the ultrafast electron microscope (UEM). (**A**) A standard UEM uses an ultraviolet (UV) pulse-triggered photocathode to generate ultrafast photoelectron wavepackets (green). Scan coils deflect the electron beam in scanning TEM (STEM). A femtosecond (fs) pump (blue) photoexcites the specimen (red) at fixed time delays relative to the photoelectron probe. A q-slit (teal) enables momentum-resolved EELS. Apertures are excluded for clarity. (**B–E**) Time-resolved and ultrafast EELS imaging methods. (**B**) CDEM maps charge-induced terahertz (THz) fields around a specimen. (**C**) Ultrafast low-loss EELS quantifies a material's free carrier density change due to thermal expansion or strain. (**D**) Time- and momentum-resolved EELS measures carrier dynamics in reciprocal space with a q-slit. (**E**) Ultrafast core-loss EELS probes photoinduced changes in oxidation state and bonding due to charge transfer and phonons.

At longer, nanosecond temporal delays, the dominant observables are excited-state population kinetics, carrier transport, and thermal diffusion. Time-resolved EM in the nanosecond regime is well suited to measure carrier trapping, recombination, phonon–phonon relaxation, and heat flow.[48–50] New fast direct electron detectors with high-speed readout now measure <1 μs timescales relevant to carrier hopping, diffusion, and trapping; and initial demonstrations have even imaged nanosecond heat diffusion kinetics.[51,52] **Figure 1.7** highlights these various optically coupled TEM methods, and additional reviews

highlight the full landscape of measurable chemical dynamics with optically coupled and ultrafast TEM.[30,53,54]

1.4 Outlook

This thesis develops and implements photomodulated EELS in the optically coupled TEM for studying steady-state photoexcited carrier and thermal dynamics in equilibrium. Our approach advances the field's understanding of complex and convoluted thermal and carrier effects on low-loss and core-loss EEL spectra. We first test this approach using photomodulated X-ray absorption spectra of plasmonic core-shell nanoparticles, distinguishing photothermal heating from electron transfer in the nanoparticle's outer shell. We further advance this methodology through careful temperature-dependent EELS control studies on silicon. Our experimental and computational results on crystalline silicon report that the temperature-dependent redshifts of core-loss EELS and X-ray edges result from a decrease of semiconductors' band gaps with temperature. Next, we apply these computational and experimental advancements to study the photomodulated thermal and carrier populations in doped $SrTiO_3$ nanoparticles that perform photocatalytic water splitting. Using the optically coupled TEM, we directly image photoexcited carriers trapped at the nanoparticle's surface oxygen vacancies. Lastly, we aim to expand these measurements to probe photocatalysts and their carrier dynamics in liquids. We perform optically coupled liquid phase TEM (LPTEM) measurements with catalysts in water encapsulated by amorphous carbon thin films, characterizing the water evaporation dynamics and thermal limitations of the thin support films. Our achievements make significant progress toward developing ultrafast and time-resolved EELS to image nanoscale photocatalytic dynamics occurring at femtosecond-to-second timescales.

Ultrafast EELS continues to advance as new instrumental capabilities are developed, offering a direct route to imaging light- and bias-driven dynamics at the nanoscale. Developments in RF and electrostatic beam blanking are improving probe brightness and coherence, while fast, event-based direct electron detectors are increasing EELS sensitivity. Extending ultrafast EELS to in situ and operando platforms such as environmental cells with gases,

liquids, and applied bias will be critical for studying photocatalytic and electrochemical processes under working conditions. Combining ultrafast EELS with cryogenic stages and low-dose acquisition strategies may minimize beam-induced specimen damage and expand the technique to soft matter, molecular, and biological systems. Together, advances in instrumentation, theory, and data analysis are positioning time-resolved and ultrafast EELS as a powerful spectroscopic tool for next-generation materials science, with broad impact across quantum materials, solar energy conversion, nanophotonics, and related fields.

1.5 References

(1) Muller, D. A. Structure and Bonding at the Atomic Scale by Scanning Transmission Electron Microscopy. *Nat. Mater.* **2009**, *8* (4), 263–270. https://doi.org/10.1038/nmat2380.

(2) Liu, H.; Baskin, J. S.; Zewail, A. H. Infrared PINEM Developed by Diffraction in 4D UEM. *Proc. Natl. Acad. Sci. U.S.A.* **2016**, *113* (8), 2041–2046. https://doi.org/10.1073/pnas.1600317113.

(3) Nguyen, K. X.; Jiang, Y.; Lee, C.-H.; Kharel, P.; Zhang, Y.; van der Zande, A. M.; Huang, P. Y. Achieving Sub-0.5-Angstrom–Resolution Ptychography in an Uncorrected Electron Microscope. *Science* **2024**, *383* (6685), 865–870. https://doi.org/10.1126/science.adl2029.

(4) Chen, Z.; Jiang, Y.; Shao, Y.-T.; Holtz, M. E.; Odstrčil, M.; Guizar-Sicairos, M.; Hanke, I.; Ganschow, S.; Schlom, D. G.; Muller, D. A. Electron Ptychography Achieves Atomic-Resolution Limits Set by Lattice Vibrations. *Science* **2021**, *372* (6544), 826–831. https://doi.org/10.1126/science.abg2533.

(5) Martin, E. E.; Trolan, J. K.; Dyke, W. P. Stable, High Density Field Emission Cold Cathode. *J. Appl. Phys.* **1960**, *31* (5), 782–789. https://doi.org/10.1063/1.1735699.

(6) Crewe, A. V.; Eggenberger, D. N.; Wall, J.; Welter, L. M. Electron Gun Using a Field Emission Source. *Rev. Sci. Instrum.* **1968**, *39* (4), 576–583. https://doi.org/10.1063/1.1683435.

(7) Heller, N. J.; Washington, A. J.; Cushing, S. K. *Electron Energy Loss Spectroscopy*; American Chemical Society, 2025. https://doi.org/10.1021/acsinfocus.7e9010.

(8) Kim, Y.-J.; Palmer, L. D.; Lee, W.; Heller, N. J.; Cushing, S. K. Using Electron Energy-Loss Spectroscopy to Measure Nanoscale Electronic and Vibrational

Dynamics in a TEM. *J. Chem. Phys.* **2023**, *159* (5), 050901. https://doi.org/10.1063/5.0147356.

(9) Yang, H.; Konečná, A.; Xu, X.; Cheong, S.-W.; Batson, P. E.; García de Abajo, F. J.; Garfunkel, E. Simultaneous Imaging of Dopants and Free Charge Carriers by Monochromated EELS. *ACS Nano* **2022**, *16* (11), 18795–18805. https://doi.org/10.1021/acsnano.2c07540.

(10) Hage, F. S.; Radtke, G.; Kepaptsoglou, D. M.; Lazzeri, M.; Ramasse, Q. M. Single-Atom Vibrational Spectroscopy in the Scanning Transmission Electron Microscope. *Science* **2020**, *367* (6482), 1124–1127. https://doi.org/10.1126/science.aba1136.

(11) Gadre, C. A.; Yan, X.; Song, Q.; Li, J.; Gu, L.; Huyan, H.; Aoki, T.; Lee, S.-W.; Chen, G.; Wu, R.; Pan, X. Nanoscale Imaging of Phonon Dynamics by Electron Microscopy. *Nature* **2022**, *606* (7913), 292–297. https://doi.org/10.1038/s41586-022-04736-8.

(12) Hachtel, J. A.; Huang, J.; Popovs, I.; Jansone-Popova, S.; Keum, J. K.; Jakowski, J.; Lovejoy, T. C.; Dellby, N.; Krivanek, O. L.; Idrobo, J. C. Identification of Site-Specific Isotopic Labels by Vibrational Spectroscopy in the Electron Microscope. *Science* **2019**, *363* (6426), 525–528. https://doi.org/10.1126/science.aav5845.

(13) Nelayah, J.; Kociak, M.; Stéphan, O.; García de Abajo, F. J.; Tencé, M.; Henrard, L.; Taverna, D.; Pastoriza-Santos, I.; Liz-Marzán, L. M.; Colliex, C. Mapping Surface Plasmons on a Single Metallic Nanoparticle. *Nat. Phys.* **2007**, *3* (5), 348–353. https://doi.org/10.1038/nphys575.

(14) Wu, Y.; Li, G.; Camden, J. P. Probing Nanoparticle Plasmons with Electron Energy Loss Spectroscopy. *Chem. Rev.* **2018**, *118* (6), 2994–3031. https://doi.org/10.1021/acs.chemrev.7b00354.

(15) Losquin, A.; Kociak, M. Link between Cathodoluminescence and Electron Energy Loss Spectroscopy and the Radiative and Full Electromagnetic Local Density of States. *ACS Photonics* **2015**, *2* (11), 1619–1627. https://doi.org/10.1021/acsphotonics.5b00416.

(16) García de Abajo, F. J.; Kociak, M. Probing the Photonic Local Density of States with Electron Energy Loss Spectroscopy. *Phys. Rev. Lett.* **2008**, *100* (10), 106804. https://doi.org/10.1103/PhysRevLett.100.106804.

(17) Tan, H.; Verbeeck, J.; Abakumov, A.; Van Tendeloo, G. Oxidation State and Chemical Shift Investigation in Transition Metal Oxides by EELS. *Ultramicroscopy* **2012**, *116*, 24–33. https://doi.org/10.1016/j.ultramic.2012.03.002.

(18) Tao, R.; Todorovic, R.; Liu, J.; Meyer, R. J.; Arnold, A.; Walkosz, W.; Zapol, P.; Romanenko, A.; Cooley, L. D.; Klie, R. F. Electron Energy-Loss Spectroscopy Study of Metallic Nb and Nb Oxides. *J. Appl. Phys.* **2011**, *110* (12), 124313. https://doi.org/10.1063/1.3665193.

(19) Pal, R.; Bourgeois, L.; Weyland, M.; Sikder, A. K.; Saito, K.; Funston, A. M.; Bellare, J. R. Chemical Fingerprinting of Polymers Using Electron Energy-Loss Spectroscopy. *ACS Omega* **2021**, *6* (37), 23934–23942. https://doi.org/10.1021/acsomega.1c02939.

(20) Yan, X.; Gadre, C. A.; Aoki, T.; Pan, X. Probing Molecular Vibrations by Monochromated Electron Microscopy. *Trends. Chem.* **2022**, *4* (1), 76–90. https://doi.org/10.1016/j.trechm.2021.10.004.

(21) Raether, H. *Excitation of Plasmons and Interband Transitions by Electrons*; Springer -Verlag Berlin Heidelberg, 1980. https://doi.org/10.1007/BFb0045951.

(22) Piprek, J. *Semiconductor Optoelectronic Devices: Introduction to Physics and Simulation*; Academic Press, Elsevier Science, San Diego, California, USA, 2003. https://doi.org/10.1016/C2009-0-22633-X.

(23) Li, H. Y.; Zhou, S. M.; Li, J.; Chen, Y. L.; Wang, S. Y.; Shen, Z. C.; Chen, L. Y.; Liu, H.; Zhang, X. X. Analysis of the Drude Model in Metallic Films. *Appl. Opt.* **2001**, *40* (34), 6307–6311. https://doi.org/10.1364/AO.40.006307.

(24) Eswara Moorthy, S. K.; Howe, J. M. Temperature Dependence of the Plasmon Energy in Liquid and Solid Phases of Pure Al and of an Al-Si Alloy Using Electron Energy-Loss Spectroscopy. *J. Appl. Phys.* **2011**, *110* (4), 043515. https://doi.org/10.1063/1.3624735.

(25) Nerl, H. C.; Guerrero-Felipe, J. P.; Valencia, A. M.; Elyas, K. F.; Höflich, K.; Koch, C. T.; Cocchi, C. Mapping the Energy-Momentum Dispersion of hBN Excitons and Hybrid Plasmons in hBN-WSe_2 Heterostructures. *npj 2D Mater. Appl.* **2024**, *8* (1), 68. https://doi.org/10.1038/s41699-024-00500-w.

(26) Timrov, I.; Vast, N.; Gebauer, R.; Baroni, S. turboEELS—A Code for the Simulation of the Electron Energy Loss and Inelastic X-Ray Scattering Spectra Using the Liouville–Lanczos Approach to Time-Dependent Density-Functional Perturbation Theory. *Comput. Phys. Commun.* **2015**, *196*, 460–469. https://doi.org/10.1016/j.cpc.2015.05.021.

(27) Jiang, Y.; Chen, Z.; Han, Y.; Deb, P.; Gao, H.; Xie, S.; Purohit, P.; Tate, M. W.; Park, J.; Gruner, S. M.; Elser, V.; Muller, D. A. Electron Ptychography of 2D Materials to Deep Sub-Ångström Resolution. *Nature* **2018**, *559* (7714), 343–349. https://doi.org/10.1038/s41586-018-0298-5.

(28) Dellby, N.; Quillin, S. C.; Krivanek, O. L.; Hrncirik, P.; Mittelberger, A.; Plotkin-Swing, B.; Lovejoy, T. C. Ultra-High Resolution EELS Analysis and STEM Imaging at 20 keV. *Microanal.* **2023**, *29* (Supplement_1), 626–627. https://doi.org/10.1093/micmic/ozad067.305.

(29) Vinson, J. Advances in the OCEAN-3 Spectroscopy Package. *Phys. Chem. Chem. Phys.* **2022**, *24* (21), 12787–12803. https://doi.org/10.1039/D2CP01030E.

(30) Lee, W.; Palmer, L. D.; Gage, T. E.; Cushing, S. K. Imaging Nanoscale Carrier, Thermal, and Structural Dynamics with Time-Resolved and Ultrafast Electron Energy-Loss Spectroscopy. *Chem. Phys. Rev.* **2025**, *6* (4), 041303. https://doi.org/10.1063/5.0289128.

(31) Groot, F. de; Kotani, A. *Core Level Spectroscopy of Solids*; CRC Press: Boca Raton, 2008. https://doi.org/10.1201/9781420008425.

(32) Barantani, F.; Claude, R.; Iyikanat, F.; Madan, I.; Sapozhnik, A. A.; Puppin, M.; Weaver, B.; LaGrange, T.; de Abajo, F. J. G.; Carbone, F. Ultrafast Momentum-Resolved Visualization of the Interplay between Phonon-Mediated Scattering and Plasmons in Graphite. *Sci. Adv.* **2025**, *11* (14), eadu1001. https://doi.org/10.1126/sciadv.adu1001.

(33) Tavabi, A. H.; Rosi, P.; Bertoni, G.; Rotunno, E.; Belsito, L.; Roncaglia, A.; Frabboni, S.; Gazzadi, G. C.; Karimi, E.; Tiemeijer, P.; Dunin-Borkowski, R. E.; Grillo, V. Demonstration of Angular-Momentum-Resolved Electron Energy-Loss Spectroscopy. *Nat. Commun.* **2025**, *16* (1), 6601. https://doi.org/10.1038/s41467-025-60804-3.

(34) Hage, F. S.; Nicholls, R. J.; Yates, J. R.; McCulloch, D. G.; Lovejoy, T. C.; Dellby, N.; Krivanek, O. L.; Refson, K.; Ramasse, Q. M. Nanoscale Momentum-Resolved Vibrational Spectroscopy. *Sci. Adv.* **2018**, *4* (6), eaar7495. https://doi.org/10.1126/sciadv.aar7495.

(35) Hui, D.; Alqattan, H.; Sennary, M.; Golubev, N. V.; Hassan, M. Th. Attosecond Electron Microscopy and Diffraction. *Sci. Adv.* **2024**, *10* (34), eadp5805. https://doi.org/10.1126/sciadv.adp5805.

(36) Yuan, M.; Alqattan, H.; Hui, D.; Sennary, M.; Pervak, V.; Golubev, N. V.; Hassan, M. T. Attomicroscopy Imaging and Control of Electron Motion in Graphene. Ver. 1. *arXiv,* November 5, 2024. https://doi.org/10.48550/arXiv.2411.02731.

(37) Kim, Y.-J.; Park, W.-W.; Nho, H.-W.; Kwon, O.-H. High-Resolution Correlative Imaging in Ultrafast Electron Microscopy. *Adv. Phys. X* **2024**, *9* (1), 2316710. https://doi.org/10.1080/23746149.2024.2316710.

(38) Barwick, B.; Park, H. S.; Kwon, O.-H.; Baskin, J. S.; Zewail, A. H. 4D Imaging of Transient Structures and Morphologies in Ultrafast Electron Microscopy. *Science* **2008**, *322* (5905), 1227–1231. https://doi.org/10.1126/science.1164000.

(39) Flannigan, D. J.; Zewail, A. H. 4D Electron Microscopy: Principles and Applications. *Acc. Chem. Res.* **2012**, *45* (10), 1828–1839. https://doi.org/10.1021/ar3001684.

(40) Kuwahara, M.; Mizuno, L.; Yokoi, R.; Morishita, H.; Ishida, T.; Saitoh, K.; Tanaka, N.; Kuwahara, S.; Agemura, T. Transient Electron Energy-Loss Spectroscopy of Optically Stimulated Gold Nanoparticles Using Picosecond Pulsed Electron Beam. *Appl. Phys. Lett.* **2022**, *121* (14), 143503. https://doi.org/10.1063/5.0108266.

(41) Vanacore, G. M.; van der Veen, R. M.; Zewail, A. H. Origin of Axial and Radial Expansions in Carbon Nanotubes Revealed by Ultrafast Diffraction and Spectroscopy. *ACS Nano* **2015**, *9* (2), 1721–1729. https://doi.org/10.1021/nn506524c.

(42) Zheng, D.; Zhu, C.; Li, Z.; Li, Z.; Li, J.; Sun, S.; Zhang, Y.; Wang, F.; Tian, H.; Yang, H.; Li, J. Ultrafast Lattice and Electronic Dynamics in Single-Walled Carbon Nanotubes. *Nanoscale Adv.* **2020**, *2* (7), 2808–2813. https://doi.org/10.1039/D0NA00269K.

(43) Piazza, L.; Ma, C.; Yang, H. X.; Mann, A.; Zhu, Y.; Li, J. Q.; Carbone, F. Ultrafast Structural and Electronic Dynamics of the Metallic Phase in a Layered Manganite. *Struct. Dyn.* **2013**, *1* (1), 014501. https://doi.org/10.1063/1.4835116.

(44) van der Veen, R. M.; Penfold, T. J.; Zewail, A. H. Ultrafast Core-Loss Spectroscopy in Four-Dimensional Electron Microscopy. *Struct. Dyn.* **2015**, *2* (2), 024302. https://doi.org/10.1063/1.4916897.

(45) Su, Z.; Baskin, J. S.; Zhou, W.; Thomas, J. M.; Zewail, A. H. Ultrafast Elemental and Oxidation-State Mapping of Hematite by 4D Electron Microscopy. *J. Am. Chem. Soc.* **2017**, *139* (13), 4916–4922. https://doi.org/10.1021/jacs.7b00906.

(46) Madan, I.; Dias, E. J. C.; Gargiulo, S.; Barantani, F.; Yannai, M.; Berruto, G.; LaGrange, T.; Piazza, L.; Lummen, T. T. A.; Dahan, R.; Kaminer, I.; Vanacore, G. M.; García de Abajo, F. J.; Carbone, F. Charge Dynamics Electron Microscopy: Nanoscale Imaging of Femtosecond Plasma Dynamics. *ACS Nano* **2023**, *17* (4), 3657–3665. https://doi.org/10.1021/acsnano.2c10482.

(47) Yannai, M.; Dahan, R.; Gorlach, A.; Adiv, Y.; Wang, K.; Madan, I.; Gargiulo, S.; Barantani, F.; Dias, E. J. C.; Vanacore, G. M.; Rivera, N.; Carbone, F.; García de Abajo, F. J.; Kaminer, I. Ultrafast Electron Microscopy of Nanoscale Charge Dynamics in Semiconductors. *ACS Nano* **2023**, *17* (4), 3645–3656. https://doi.org/10.1021/acsnano.2c10481.

(48) Sinha, S. K.; Khammari, A.; Picher, M.; Roulland, F.; Viart, N.; LaGrange, T.; Banhart, F. Nanosecond Electron Pulses in the Analytical Electron Microscopy of a Fast Irreversible Chemical Reaction. *Nat. Commun.* **2019**, *10* (1), 3648. https://doi.org/10.1038/s41467-019-11669-w.

(49) Picher, M.; Bücker, K.; LaGrange, T.; Banhart, F. Imaging and Electron Energy-Loss Spectroscopy Using Single Nanosecond Electron Pulses. *Ultramicroscopy* **2018**, *188*, 41–47. https://doi.org/10.1016/j.ultramic.2018.03.006.

(50) Durham, D. B.; Gage, T. E.; Horn, C. P.; Ma, X.; Liu, H.; Arslan, I.; Guha, S.; Phatak, C. Nanosecond Structural Dynamics during Electrical Melting of Charge Density Waves in 1T–TaS_2. *Phys. Rev. Lett.* **2024**, *132* (22), 226201. https://doi.org/10.1103/PhysRevLett.132.226201.

(51) Castioni, F.; Auad, Y.; Blazit, J.-D.; Li, X.; Woo, S. Y.; Watanabe, K.; Taniguchi, T.; Ho, C.-H.; Stéphan, O.; Kociak, M.; Tizei, L. H. G. Nanosecond Nanothermometry in an Electron Microscope. *Nano Lett.* **2025**, *25* (4), 1601–1608. https://doi.org/10.1021/acs.nanolett.4c05692.

(52) Jannis, D.; Hofer, C.; Gao, C.; Xie, X.; Béché, A.; Pennycook, T. J.; Verbeeck, J. Event Driven 4D STEM Acquisition with a Timepix3 Detector: Microsecond Dwell Time and Faster Scans for High Precision and Low Dose Applications. *Ultramicroscopy* **2022**, *233*, 113423. https://doi.org/10.1016/j.ultramic.2021.113423.

(53) Alcorn, F. M.; Jain, P. K.; van der Veen, R. M. Time-Resolved Transmission Electron Microscopy for Nanoscale Chemical Dynamics. *Nat. Rev. Chem.* **2023**, *7* (4), 256–272. https://doi.org/10.1038/s41570-023-00469-y.

(54) LaGrange, T.; Cattaneo, P.; Barwick, B.; Flannigan, D. J.; Weissenrieder, J.; Carbone, F. Laser-Driven Ultrafast Transmission Electron Microscopy. *Nat. Rev. Methods Primers* **2025**, *5* (1), 61. https://doi.org/10.1038/s43586-025-00431-w.

CHAPTER 2

DETERMINING QUASI-EQUILIBRIUM ELECTRON AND HOLE DISTRIBUTIONS OF PLASMONIC PHOTOCATALYSTS USING PHOTOMODULATED X-RAY ABSORPTION SPECTROSCOPY

Adapted with permission from the following:

Palmer, L. D.; Lee, W.; Dong, C.L.; Liu, R.-S.; Wu, N.; Cushing, S. K. Determining Quasi-Equilibrium Electron and Hole Distributions from Plasmonic Photocatalysts using Photomodulated X-ray Absorption Spectroscopy. *ACS Nano* **2024**, *18* (13), 9344–9353. https://doi.org/10.1021/acsnano.3c08181.

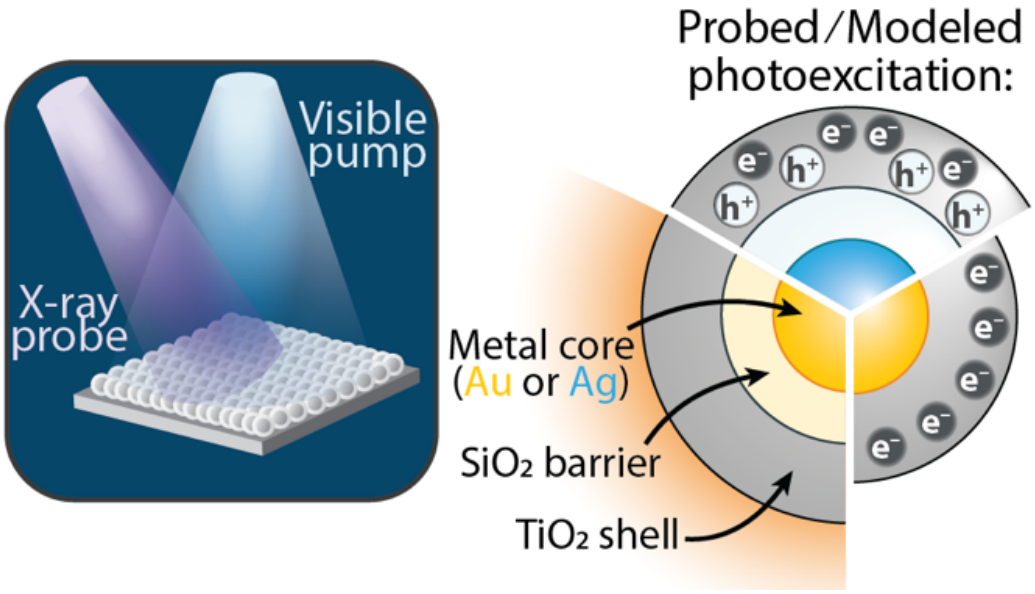

2.1 Introduction

A balance between carrier photoexcitation, thermalization, and recombination rates determines the quasi-equilibrium carrier distribution that controls photocatalytic and photovoltaic device efficiencies (**Figure 2.1**).[1–3] A quasi-equilibrium state occurs during the thermodynamic balance of the system's photoexcitation and relaxation. Photoexcited carriers are generally assumed to be fully thermalized to the band edges at the device's working conditions.[4] However, slowed hot carrier cooling through phonon bottlenecks,[5] surface state trapping,[6–9] or dielectric carrier Coulomb screening[10] can generate a non-thermal carrier quasi-equilibrium. In nanoscale junctions, photoexcited carriers can transfer between active layers or to surface catalysts on timescales shorter than carrier thermalization.[11,12] Transferring the quasi-equilibrium hot carrier population into surface reactants then modifies a semiconductor's photochemical reduction potential, tailoring resultant reaction products.[13] For example, plasmonic metal-semiconductor junctions have been used to increase semiconductors' photocatalytic product selectivity[14–16] and solar power conversion efficiency.[17,18]

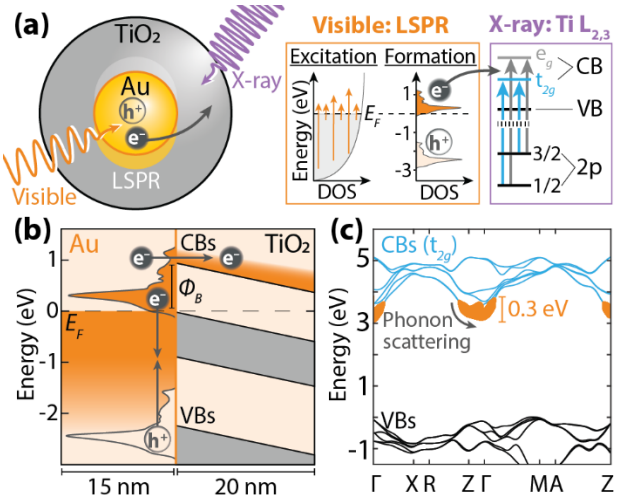

Figure 2.1. Photoexcited properties of plasmonic core-shell nanoparticles. (**a**) Continuous photoexcitation of a metal nanoparticle's localized surface plasmon resonance (LSPR) with visible light results in dynamic carrier excitation.[ref. 2] Hot carrier formation then occurs following electron-electron and electron-phonon scattering.[ref. 3] The hot carriers transfer into TiO_2 and can be probed with the Ti $L_{2,3}$ edge. (**b**) The hot carriers

transfer over the Au@TiO_2 Schottky barrier (ϕ_B) and fill the TiO_2 conduction bands (CBs) with an excess energy of 0.3 eV and subsequently (**c**) thermalize in the CBs through phonon scattering.

Measuring the quasi-equilibrium carrier distribution is therefore critical. However, few methods to date can characterize the equilibrium photoexcited carrier population with the same detail as ultrafast pump-probe methods like two-dimensional, terahertz, or photoemission spectroscopies.[19–22] While ultrafast spectroscopy is the conventional method for measuring carrier thermalization and recombination, ultrafast measurements sum over different relaxation pathways, often use a high peak power that exceeds the solar flux, and rely on laser sources that are more narrowband than the solar spectrum. When effects such as Fermi level pinning, defects, and surface states are present, it can be difficult to reconstruct steady-state carrier distributions using ultrafast measurements alone.

X-ray spectroscopy is one potential method for resolving carrier distributions and dynamics. Transient X-ray spectroscopy is now routinely used to measure element-specific electron and hole energies in multi-element catalysts.[23–26] Obtaining the same information should also be possible using steady-state, photomodulated X-ray spectroscopy.[27] However, measuring and interpreting photomodulated X-ray spectra are challenging tasks because the decreased photo-induced carrier concentration and slower repetition rate make the signal-to-noise ratio (SNR) significantly lower. Therefore, accurate excited-state X-ray theory is needed, even more so than for ultrafast X-ray spectroscopy, to interpret the small photomodulated spectral intensity within the experimental noise.

Previous investigations of plasmonic Au@TiO_2 nanoparticles and their photomodulated X-ray spectra suggest that quasi-equilibrium hot electron populations exist in TiO_2.[7,28,29] In our prior work, the photoexcited X-ray spectra were not modeled fully *ab initio* but were rather calculated using a semi-quantitative model of phase-space filling and lifetime effects.[29] Thermal and photoexcited hole effects were not included. Here, we use excited-state density functional theory (DFT) and Bethe-Salpeter equation (BSE) calculations to evaluate steady-state photomodulated X-ray spectra. To simulate hot electron X-ray spectra, we fill the DFT-

calculated conduction band states with electrons from the conduction band minimum (CBM) to a specified energy and calculate the corresponding spectrum with the BSE. Methods that model transient charge configurations *ab initio* instead use density functional perturbation theory and the Boltzmann transport equation to predict ultrafast charge redistribution following electron-phonon interactions and transport.[30] However, density functional perturbation theory is not used for modeling steady-state dynamics due to computational costs.

In this work, we test whether photomodulated, steady-state X-ray spectroscopy can be used to quantify quasi-equilibrium carrier distributions. X-ray absorption at the Ti $L_{2,3}$ edge is measured for each nanoparticle with modulated photoexcitation. An adiabatic approximation to the BSE is then used to predict the change in the X-ray spectrum for each possible photoexcited configuration. We use a mean squared error (MSE) analysis to compare the potential theoretical contributions of thermal, hot electron, and dipolar excitations to the signal from plasmonic core-shell nanoparticles designed to isolate each one of these effects. Even in the case of relatively noisy spectra, quasi-equilibrium hot carrier distributions are differentiated from photothermal heat. Separating electron from hole effects on a photothermal background is more difficult because of the hole's smaller perturbation to the Ti $L_{2,3}$ edge. Within experimental noise, electron versus hole populations were not separable with statistical significance. However, our calculations demonstrate that electrons and holes have distinct spectral features and could be differentiated with improved X-ray measurements, and we discuss the required experimental conditions for such measurements. Our findings suggest that photomodulated X-ray spectroscopy at non-time-resolved beamlines can be used to separate electron, hole, and thermal excitations, but continued improvement in experimental SNRs is needed when multiple photoexcited processes simultaneously exist.

2.2 Results and Discussion

A nanoparticle's localized surface plasmon resonance (LSPR) can be used to transfer energy to a semiconductor through multiple mechanisms. Here, a SiO_2 layer is used to systematically

control three such mechanisms between a Au or Ag nanoparticle core and a TiO_2 shell. For Au@TiO_2 nanoparticles, plasmonic hot electrons in Au can overcome the interfacial Schottky junction to inject into TiO_2 (**Figure 2.2a,d**).[3,31,32] Ag@SiO_2@TiO_2 nanoparticles use the plasmon's dipole moment to increase the light absorption rate in the tail of a semiconductor's absorption edge, creating electron-hole pairs (**Figure 2.2b,e**).[20,28] In Au@SiO_2@TiO_2 nanoparticles, a SiO_2 layer prevents carrier transfer from Au into TiO_2, so the TiO_2 shell only experiences heating from the Au core to provide a control experiment (**Figure 2.2c,f**).[28] Past work has verified that these core-shell nanoparticles isolate these excited-state effects.[28]

This paper theoretically interprets previously measured X-ray spectra of the nanoparticles synthesized and characterized in Ref. 28. In these previous measurements, the nanoparticles were reported to have a 15 nm radius Au or Ag core, a 10 nm thick SiO_2 insulating layer (not present in Au@TiO_2), and a 10 – 20 nm amorphous TiO_2 outer shell. UV–visible absorption spectroscopy was used to measure the LSPR center wavelength at 420 nm for Ag and 560 nm for Au **(Figure 2.2a-c)**.

The approximate interfacial band bending of each heterojunction is calculated using a 1D drift-diffusion model implemented in the Automat FOR Simulation of HETerostructures (AFORS-HET) (**Figure 2.2d-f**).[33] This approach does not consider nanoscale near-field or photoexcited effects. The approximate Schottky barriers are 0.9 eV for Au@TiO_2, 0.8 eV for Ag@SiO_2@TiO_2, and 0.7 eV for Au@SiO_2@TiO_2. The metal-semiconductor junction produces band bending and built-in electric fields in the TiO_2 and SiO_2 layers. The average built-in field estimated for the semiconducting layers is ~10^5 V/cm. The SiO_2 insulator acts as a carrier tunnelling barrier between the metal and TiO_2, and the Schottky barrier in such cases refers to the energetic barrier for electron transfer at the SiO_2-TiO_2 interface. Considering the ~4.4 eV Au-SiO_2 Schottky barrier, which exceeds the maximum hot electron energy by 3.2 eV, Au hot carriers would need to tunnel through SiO_2 to reach TiO_2. Similar junctions with a 4.8 nm SiO_2 oxide were previously measured to have a $<10^{-10}$ A/cm^2 tunneling current at 10^5 V/cm following an applied bias.[34] Therefore, as experimentally

observed, photoexcited electrons would not transfer to TiO_2 for the Au@SiO_2@TiO_2 system. See the Supporting Information for numerical input parameters and field calculation.

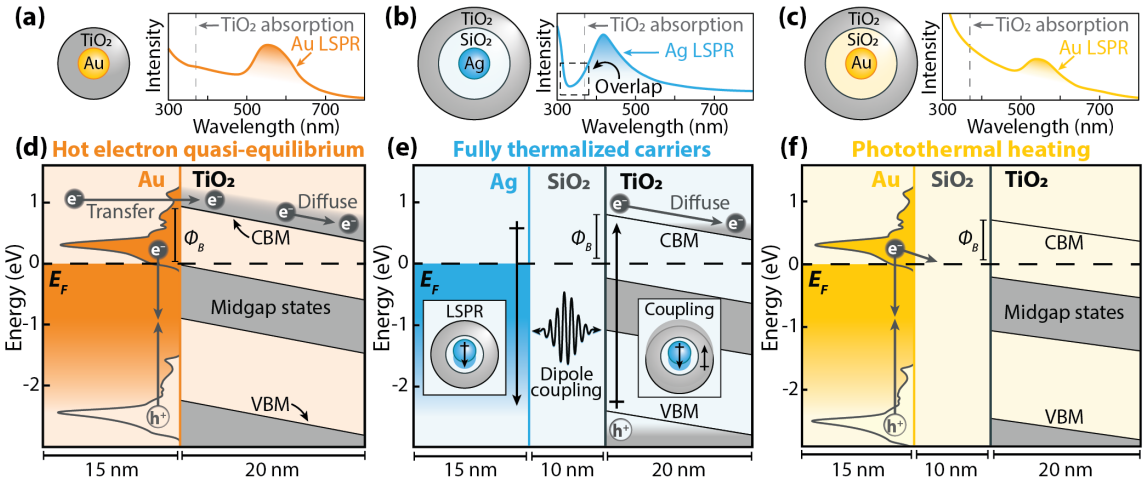

Figure 2.2. Plasmonic core-shell nanoparticle heterostructure characterization. (**a-c**) UV–visible absorption spectra for (a) Au@TiO_2, (b) Ag@SiO_2@TiO_2, and (c) Au@SiO_2@TiO_2 core-shell nanoparticles. The localized surface plasmon resonance (LSPR) and UV bandgap for amorphous TiO_2 (grey dashed line at 3.34 eV, 370 nm) are marked [refs. 43,44]. (**d-f**) Schematic representations of each nanoparticle's band alignment and hot carrier distribution (d) Hot electrons up to ~0.3 eV above the conduction band minimum (CBM), relative to the Schottky barrier (ϕ_B), have sufficient energy to transfer into TiO_2 directly.[ref. 3] (e) The Schottky barrier and SiO_2 layer prevent hot electron transfer. Instead, the localized electromagnetic field from the plasmon couples with a TiO_2 electron-hole excitation, and carriers are created at both the CBM and valence band maximum (VBM). (f) The SiO_2 layer prevents electron transfer into TiO_2.

The ground-state electronic structure and X-ray absorption of TiO_2 are first calculated as shown in **Figure 2.3**. The Ti $L_{2,3}$ X-ray absorption edge (456 – 468 eV) was measured, which corresponds to a core electron transition from Ti 2*p* to Ti 3*d* states (**Figure 2.1a, right**). The DFT calculated projected density of states (PDOS) for anatase TiO_2 is given in **Figure 2.3a**. A 1 eV scissor shift is applied to the bandgap. In the PDOS, the O 2*p* orbitals dominate the valence band and the Ti 3*d* orbitals compose the conduction band. The crystal field

characteristically splits the Ti 3*d* conduction band into the t_{2g} (blue shading) and e_g (grey shading) orbitals in the electronic structure and ground-state X-ray absorption (**Figure 2.3a,b**).[35]

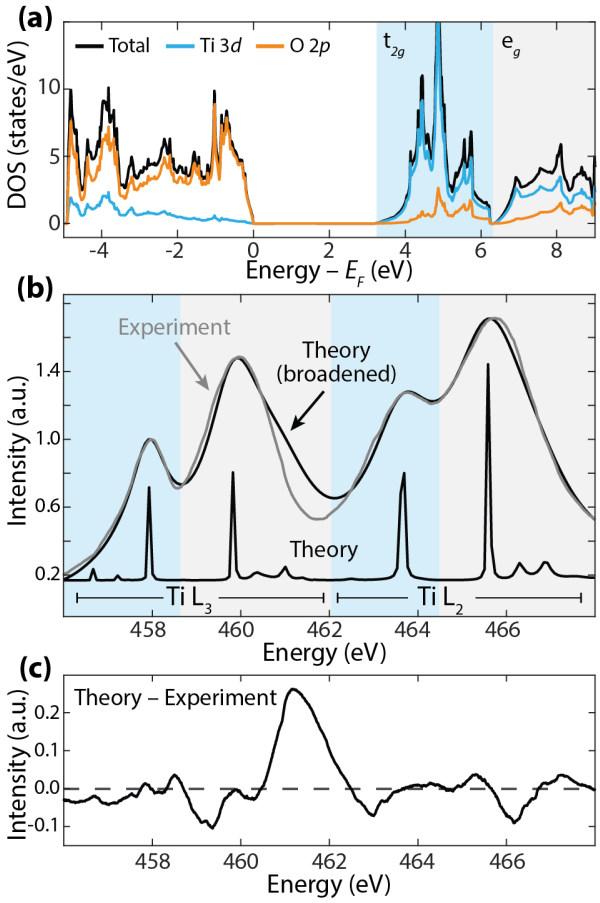

Figure 2.3. Calculation of TiO_2 electronic structure and X-ray absorption. (**a**) The DFT-calculated, projected density of states for anatase TiO_2. The Fermi level represents the valence band edge. (**b**) Calculated (black) and measured (grey) Ti $L_{2,3}$ X-ray spectra for TiO_2. The theory spectrum is broadened to match the experiment with the bottom spectrum being the unbroadened output. The blue and grey shading depict the Ti t_{2g} and e_g states, respectively. (**c**) The difference between theory and experiment.

Figure 2.3b compares the BSE simulated Ti $L_{2,3}$ edge to the measured ground-state Au@SiO_2@TiO_2 spectrum. An energy-dependent broadening method of the predicted spectrum was used to replicate the experimental core-hole lifetime broadening, which has a

3:2 broadening ratio (L_2:L_3) for the TiO_2 Ti $L_{2,3}$ edge (see Supporting Information).[36] According to the PDOS in **Figure 2.3a**, the photomodulated Ti $L_{2,3}$ edge predominantly probes photoexcited electrons over holes through the Ti 3*d* states; however, because of the screening and angular momentum coupling matrix elements in the X-ray transition Hamiltonian, holes will still perturb the core-to-valence transition excitons.[37,38]

This work approximates the nanoparticle's amorphous TiO_2 as purely anatase phase. Although 10 – 20 nm TiO_2 nanoparticles typically consist of a mixture of anatase and brookite, anatase is a slightly more stable phase, and this approximation reduces the otherwise insurmountable computational costs of excited-state X-ray BSE calculations for hundreds of atoms.[39–42] We find this to be a valid approximation due to the excellent match between the ground-state experiment and theory (**Figure 2.3b**). However, aspects of the amorphous phase electronic structure are not considered. First, there is a discrepancy between anatase and amorphous TiO_2 for the Ti L_3 e_g states at 461 eV (**Figure 2.3c**).[43] The core-hole exciton effects calculated by the BSE are therefore not accurately modeled at these energies and are not considered during the MSE analysis. Further, defect-induced midgap states (depicted in **Figure 2.2d-f**) are not modeled. Midgap states show little effect on the ground-state TiO_2 spectra but may appear as a shoulder of the L_2 t_{2g} peak at 463 eV (**Figure 2.3b,c**).

The previously measured X-ray spectra were collected using a light-on, light-off sequence with a 1-minute collection time per spectrum. A continuous-wave lamp, filtered below the 3.34 eV amorphous TiO_2 bandgap, was used to photoexcite the nanoparticles' LSPR.[44,45] Surface charging from photoexcitation creates a baseline drift in photomodulated spectra for the total electron yield detection method.[46] To account for charging, each spectrum is normalized to the edge onset maximum near 458 eV (grey dashed line in **Figure 2.4**) after the baseline background subtraction. The charging normalization creates artifacts directly below and above the X-ray absorption edge, so only the 458 – 466 eV range is compared to theory herein (see average spectra for all samples overlaid in Figure S5). Charging is not measured for the Au@SiO_2@TiO_2 sample, which confirms that only heat results from

photoexcitation. However, the insets of **Figure 2.4a** reflect that even the light-off spectra change after modulating photoexcitation, meaning residual charges may perturb the total electron yield acquisition even after sample relaxation.

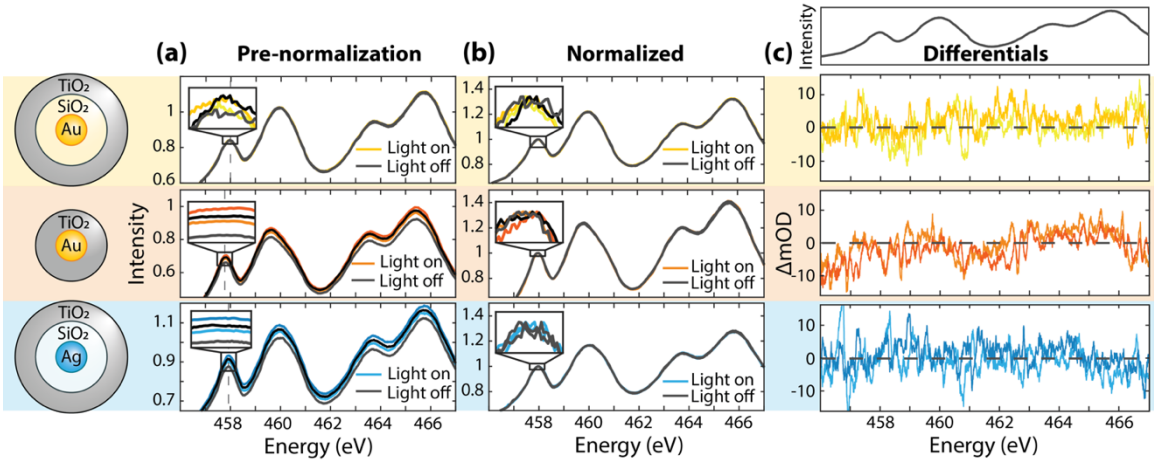

Figure 2.4. X-ray absorption spectra of core-shell nanoparticles with and without photoexcitation. (**a**) Raw, light on and light off Ti $L_{2,3}$ edge X-ray spectra of the amorphous TiO_2 outer shell. The spectral intensity increased throughout the data collection of all four spectra. The spectra are background-subtracted. Each inset magnifies the edge maxima intensity differences caused by charging. Each inset window size is 0.15 eV width but a variable amplitude. (**b**) Spectra from (a) normalized to the edge maximum near 458 eV (grey dashed line) to correct for charging that broadly increases the spectral amplitude. (**c**) Photoexcited differential spectra of the normalized data in (b) to highlight photomodulated energetic shifts in the $L_{2,3}$ edge. The lighter spectra are from the first light on/light off collection. The ground state experimental spectrum is shown above for reference.

The measured differential absorption, calculated as the log of spectra collected with the lamp on divided by those with the lamp off and averaged across two data sets, is used to identify photoexcited carrier and structural effects on the X-ray spectra (**Figure 2.4**). Because the total electron yield detection only probes the first ~4 nm of TiO_2, only carriers in surface trap states in the amorphous TiO_2 are probabilistically measured.[47] The spectra in **Figure 2.4** are relatively noisy due to the lower power of the excitation source and slower modulation time of the steady-state measurement. Therefore, we first test the accuracy of our *ab initio*

approach by comparing to a previous ultrafast X-ray absorption spectrum of anatase TiO_2 (Figure S1).[27] The measured transient spectrum is analyzed using an adiabatic approximation to excited-state effects in the BSE. This approach has been verified previously for other transient X-ray datasets and is described in the **Methods** section.[26,37,38] The ultrafast time slice is after carrier thermalization (1 ps). The proposed *ab initio* method accurately reproduces the transient X-ray spectrum at all energies besides 458 – 460 eV. The discrepancy is likely due to the reported onset of carrier transfer to midgap states (see Supporting Information). The electron, hole, and thermal signals are reproduced in this case, giving a baseline for the accuracy of the photomodulated data presented here.

Given this verification, we proceed to analyze the photomodulated spectra. Three differences are observed between each plasmonic excitation mechanism although it must be noted that, since only two averages are used, the statistical significance must be interpreted with caution. First, all nanoparticle's spectra have different amplitudes just after the L_3 edge at 458 eV. Second, the Au@TiO_2 has decreased absorption centered at 462 eV. Lastly, the Ag@SiO_2@TiO_2 nanoparticles have decreased absorption at 465.5 eV. We then investigate how these trends compare to the theoretically predicted photomodulated spectra, which is found to successfully model ultrafast dynamics (Figure S1).

The steady-state spectral signatures of photothermal effects are first compared to theory using the Au@SiO_2@TiO_2 experimental control (**Figure 2.5**). Photothermal heating arises from the heat produced by carrier thermalization in the metal nanoparticle after LSPR photoexcitation and relaxation.[48] The photomodulated Au@SiO_2@TiO_2 nanoparticle's experimental spectra lack the surface charging artifact that results from photoexcited carriers in the other two nanoparticle systems (**Figure 2.4a**), confirming that photoexcited carriers are not excited in TiO_2.

Heating is modeled through DFT and BSE calculations by an expansion of the TiO_2 lattice. Calculations are performed for lattice expansions equivalent to 2.5, 5.0, 10, 15, and 20 K temperature increases above 300 K (**Figure 2.5a**).[49] The spectrum's peak positions linearly redshift with increasing lattice temperature, increasing and decreasing the differential

intensity at pre- and post-edge regions, respectively. The spectrum mainly redshifts because of the Ti atoms' reduced crystal field. The simulated X-ray differential absorption for a 2.5 K lattice-expanded TiO_2 crystal is compared to the measured differential absorption in **Figure 2.5b**.

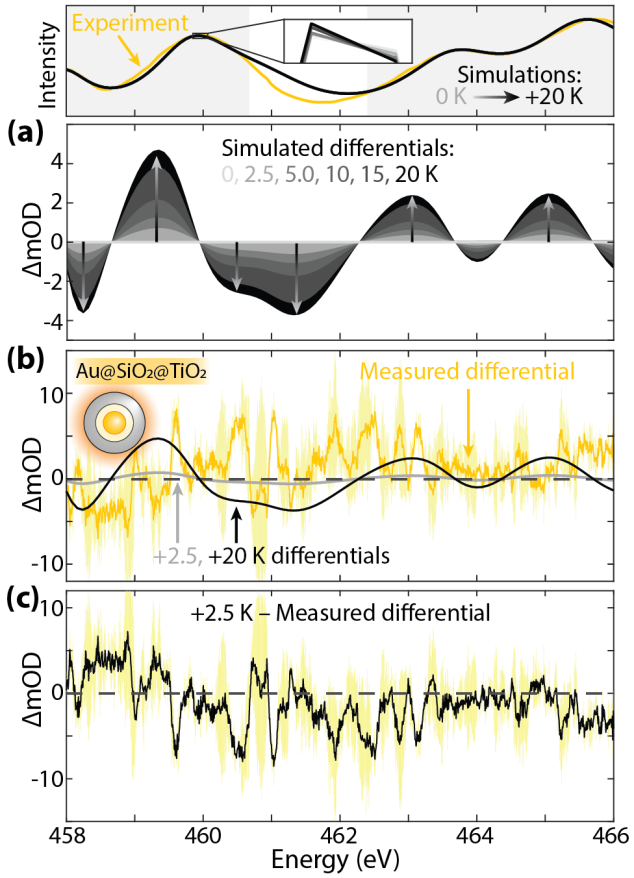

Figure 2.5. Photothermal effects on the Ti $L_{2,3}$ edge in Au@SiO_2@TiO_2. (Top) Raw spectra for reference. The spectral range analyzed by the MSE is shaded. (**a**) Simulated differential X-ray spectra for a 0 – 20 K anatase lattice expansion. The arrows highlight the differential amplitude change with an increasing lattice parameter. (**b**) The lattice-expanded differential spectra predicted for 2.5 and 20 K heating are compared to the Au@SiO_2@TiO_2 differential spectrum. The yellow shaded region depicts the experiment's standard deviation. (**c**) The measured differential subtracted from the optimized simulation differential at 2.5 K, selected using the MSE analysis. The experiment's standard deviation is included for reference.

The $Au@SiO_2@TiO_2$ nanoparticle temperature after photoexcitation was predicted to be +2.5 K through a MSE fit of all simulations in Figure S2. Subtracting the 2.5 K heating differential from the experiment (**Figure 2.5c)** reflects that the general spectral changes are reproduced. The heating simulation's largest disagreement results from the anatase TiO_2 approximation at 460 – 462 eV. The differential between theory and experiment shows bias, as in it is not centered around zero, so a statistical conclusion is difficult even if trends are similar by eye. The MSE fit predicts a ~2.5 K rise in the TiO_2 layer and is consistent, within an order of magnitude, with other studies reporting 7.7 K (theoretical)[50] and 2.6 ± 2.3 K (experimental)[51] heating of aqueous Au nanoparticles when using similar excitation densities. The thermal dissipation will of course differ in the vacuum environment for the experimental X-ray measurements.

Next, the $Au@TiO_2$ nanoparticle sample that has both photothermal and hot electron effects is examined. To simulate hot electron transfer in the $Au@TiO_2$ nanoparticles, electrons up to a specific energy above the TiO_2 CBM (0.0 eV for fully thermalized electrons, 0.1 eV, 0.3 eV, 0.45 eV, and 0.6 eV) are included in the BSE calculation (**Figure 2.6a**). We simulate spectra by approximating an average electron energy in the CBs and not a distribution. The added electrons change the core-hole screening and prevent X-ray transitions into the newly blocked states, leading to a complex differential absorption, as shown in **Figure 2.6b**. In **Figure 2.6b,** the intensity of the hot electrons' differential absorption is normalized to the total number of simulated hot electrons to better evaluate excited-state trends with increasing hot electron energy.

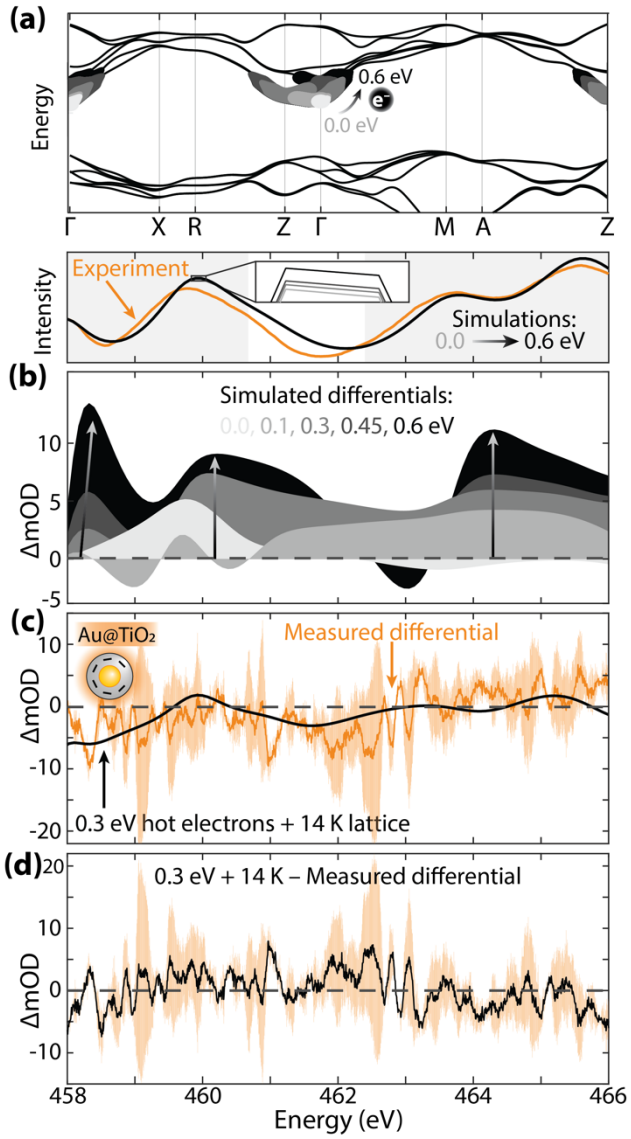

Figure 2.6. Hot electron effects on the Ti $L_{2,3}$ edge in Au@TiO_2. (**a**) Simulated hot electrons 0.0, 0.1, 0.3, 0.45, and 0.6 eV above the TiO_2 CBM (b, Top) Raw spectra for reference. The spectral range analyzed by the MSE is shaded. (**b**) Simulated differential X-ray spectra for each hot electron occupation in TiO_2. The spectral intensity is normalized to the number of electrons simulated in all but the thermalized (0.0 eV) case. (**c**) The optimized simulation with hot electrons 0.3 eV above the CBM with a 14 K lattice expansion is compared to the Au@TiO_2 measured differential absorption. The orange shaded region depicts the experiment's standard deviation. (**d**) The measured differential subtracted from the optimized simulation differential shown in (c) with the standard deviation.

Unlike photothermal heating, changes in TiO_2's simulated differential absorption are not perfectly linear with increasing electron energy (**Figure 2.6b**). Instead, spectral intensity increases with the hot electron energy and there are differential peaks from changes in the screening of the core-valence exciton and X-ray transitions blocked by hot electrons. The differential peaks are mainly a result of hot electrons affecting the screening and angular momentum components of the core-valence exciton when measured energies are above the hot carriers at the bottom of the t_{2g} bands (**Figure 2.6a**). The differential features blueshift as more hot electrons screen the exciton in the BSE. State-filling effects of hot electrons blocking X-ray transitions begin to appear at 463 eV when the simulated hot electrons fully occupy states above 0.45 eV.

The measured Au@TiO_2 nanoparticle differential absorption spectrum is compared to a simulated differential spectrum with 0.3 eV hot electrons and 14 K lattice expansion in **Figure 2.6c**. Compared to Au@SiO_2@TiO_2, the simulated X-ray spectrum with hot electrons has a new minimum around 462 eV, consistent with the measured spectral differences between samples with and without hot electrons (**Figure 2.4**). An MSE analysis was used to determine the most likely temperature and hot electron energy, based on the simulated spectra. Each modeled hot electron distribution is shown separately in Figure S9, and the differential X-ray spectra with both hot electrons and temperature simulated are in Figure S11. Here, the differential between the experiment and theory is centered around zero, but again the experimental results must be interpreted with some caution given the low number of averages. Using the MSE fit, the TiO_2 lattice temperature is found to be hotter than for the Au@SiO_2@TiO_2 nanoparticles, attributed to the larger plasmon intensity that leads to a greater level of hot electron thermalization in TiO_2 (Figure S3). Further, the 0.3 eV hot electron quasi-equilibrium distribution is consistent with recent studies, as steady-state and ultrafast Raman measurements estimate that hot electrons exceeding 0.32 and 0.34 eV, respectively, transfer from Au nanoparticles to nearby molecules.[52,53] An approximate calculation comparing the electron excitation and relaxation rates in the amorphous TiO_2 is given in the Supporting Information, but the main conclusions of **Figure 2.6** are that photothermal and hot electron effects can be differentiated within a relatively noisy spectrum.

Further light intensity-dependent control experiments would be necessary to quantify the hot electron concentration and would also be useful to clarify the nonlinear change with hot carrier concentration versus the temperature-induced shift. We approximate the measured hot electron density using the relative occupation of the state filling in the band structure. The state filling simulation for states up to 0.3 eV above the CBM best matches the experiment (**Figures 2.6c and S2b**). The integrated total DOS in this energy range is 150 states of the 10^4 total possible calculated conduction states. Using this number, and the measured DOS for nanocrystalline TiO_2 (8×10^{18} cm^{-3}), one can approximate an electron concentration of $\sim 10^{16}$ cm^{-3}.[54]

Lastly, the $Ag@SiO_2@TiO_2$ nanoparticle system is examined and is expected to have thermalized electron and hole pairs (**Figure 2.7**). This is the most challenging example to model as electrons, holes, and photothermal effects are present within the noisy experimental spectrum and the hole more weakly perturbs the spectrum than the electron since the probed Ti 2*p* states predominantly compose the conduction band (**Figure 2.3a**). The holes only change the screening and angular momentum components of the core-valence excitons in the X-ray spectrum without adding or blocking new transitions, usually the larger signal. The theoretical differential absorption in **Figure 2.7a** as compared to thermal and hot electron changes does demonstrate that adding holes to the calculation should have a measurable effect but experimentally requires a better SNR. Namely, introducing holes to a photoexcited electrons-only model produces an increase in the differential absorption largely at 462 eV and across the spectrum.

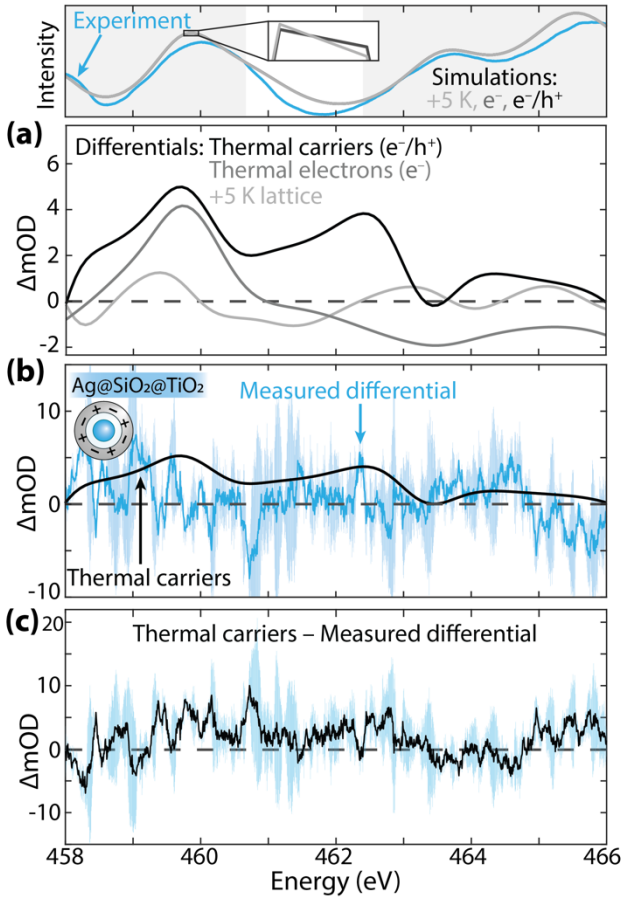

Figure 2.7. Thermalized electron plus hole effects on the Ti $L_{2,3}$ edge in $Ag@SiO_2@TiO_2$. (Top) Raw spectra for reference. The spectral range analyzed by the MSE is shaded. (**a**) Simulated differential spectra for a +5 K lattice expansion (light grey), thermalized electrons (grey), and thermalized carriers (black). The thermalized carriers are simulated at each respective band edge. (**b**) Thermalized carriers compared to the $Ag@SiO_2@TiO_2$ measured differential spectrum. The blue shaded region depicts the experiment's standard deviation. (**c**) The measured differential subtracted from the optimized simulation differential shown in (b) with the standard deviation.

The $Ag@SiO_2@TiO_2$ nanoparticles' measured differential absorption is compared to the simulated differential for thermalized carriers in **Figure 2.7b**. Calculating the differential absorption spectra and corresponding MSE for thermalized electrons, thermalized electron-hole pairs, and photothermal effects reveals that there is no statistical difference in the MSE

for the three calculations, despite the changes in the spectra between these three photoexcited effects (Figure S2c). The initial spectral features are well-captured in **Figure 2.7b**, but this alone is not enough to signify a statistical difference from the other models. The photo-charging indicates that the plasmonic resonance energy transfer effect is present as in previous reports, but a less noisy spectrum or a higher excitation density, which would exaggerate the pre-edge and hole effects, would be needed to differentiate all three models. We also plot the difference between the measured and calculated differentials in **Figure 2.7c**. The amplitude of the residual further reflects that the excited-state calculation is unable to model the experiment. However, **Figure 2.7a** indicates that the separation of electrons, holes, or electrons plus holes from photothermal effects should be possible in a quasi-equilibrium, photomodulated experiment.

Our theoretical analysis, verified by a comparison to ultrafast experiments (Figure S1), provides valuable guidance for comparing each photoexcited effect's spectrum to experimental X-ray data. Based on this analysis, future photomodulated spectroscopy measurements should aim for a photomodulated or differential SNR >2 or an average differential signal of ~5 mOD. The SNR in this work is 0.5, determined by dividing the average differential signal (1.4 mOD in **Figure 2.6c**) by the noise root-mean-squared (2.8 mOD in **Figure 2.6d**). Ultrafast studies have larger SNRs due to a higher impulse response, carrier density, and spectral chopping rate frequency, apparent in Figure S1. Additional synchrotron measurements with more extensive experimental controls would be necessary to accurately quantify the steady-state carrier equilibrium. These measurements could consider the following: a total fluorescence yield detection scheme to avoid sample charging artifacts, power-dependent photoexcitation measurements (to modulate the carrier density amplitude and temperature effects), and rapid photomodulation or extensive light-on/light-off measurements to confirm signal reproducibility. Ideal specimens would be nanometer-scale crystalline semiconductors with long carrier lifetimes or polaronic traps to increase the likelihood that atoms contributing X-ray signal are properly photoexcited (not bulk atoms in the ground state).

2.3 Conclusion

We used a set of plasmonic core-shell nanoparticles to test if a BSE-based analysis can differentiate heating, hot electron, and thermalized carrier effects in quasi-equilibrium, photomodulated X-ray absorption experiments. The lattice temperature and hot carrier energy were successfully separated and analyzed within a noisy experimental spectrum. Separating a thermalized electron and hole carrier distribution was not as successful, although this outcome is mainly due to a lower experimental signal and a spectral cancellation unique to the Ti $L_{2,3}$ edge. The BSE method proposed appears accurate enough to allow non-time-resolved X-ray beamlines to determine electron and hole effects, greatly expanding the realm of photoexcited studies. This is a particularly important advance for systems where defects, hot carrier effects, and junctions that control transport and surface catalysis through steady-state distributions are difficult to study with ultrafast spectroscopy. However, measuring quasi-equilibrium distributions requires a careful balance of the excitation rate, recombination rate, and photomodulation time. The results of our paper therefore give technical guidelines for measuring simultaneous electron, hole, and thermal quasi-equilibrium populations. The spectral signatures for each excited-state effect, and their intensity with excitation density, are particularly useful for future steady-state and ultrafast measurements of anatase TiO_2.

2.4 Methods

Core-Shell Nanoparticle Synthesis and Characterization

Core-shell metal@(SiO_2)@TiO_2 nanoparticles were synthesized and characterized previously, and this work is only a theoretical analysis of X-ray spectra for these same particles.[28] All experimental X-ray and UV–Vis spectra were collected at the time of these referenced, initial publications. Aqueous-phase UV–Vis absorption (Shimadzu 2550) measured the localized surface plasmon resonance and TiO_2 absorption onset for each particle (Figure S3).

Photodiode Heterojunction Modeling

A drift-diffusion model is used to simulate the metal-semiconductor junction for each core-shell nanoparticle design through the Automat FOR Simulation of HETerostructures (AFORS-HET) software v.2.5. This numerical simulation software uses a 1D drift-diffusion model based on self-consistent solutions to the Poisson equation to model the band bending, carrier tunneling, and junction properties.[55] See the Supporting Information for input parameters and the built-in field calculation.

X-ray Absorption Spectroscopy

The National Synchrotron Radiation Research Center (NSRRC) in Hsinchu, Taiwan, collected all Ti L edge X-ray spectra at the BL20A1 beamline in total electron yield mode (reflection geometry) depicted in Figure S4. Each specimen was mounted on conductive Cu tape without surface treatment. All secondary electrons were collected to generate the detected signal. The total Xe lamp power density was ~200 mW/cm^2 at the sample and ~10 mW/cm^2 across each plasmon resonance energy range. The photon flux was measured 1 m away from the lamp with an initial power of 500 W. The lamp was spectrally filtered to irradiate the sample with >400 nm light or below the TiO_2 bandgap, and non-AR coated optics were used as the entrance windows. The X-ray spectra were collected with a (lamp off), (lamp on), (lamp off), (lamp on) sequence for 48 s acquisition per spectrum. The X-ray analysis software at the beamline was used to subtract the background (X-ray scattering and electron emission) using a straight baseline fit below the absorption rising edge.

Ab Initio X-ray Theory

The X-ray absorption simulation package, Obtaining Core Excitations from the *Ab initio* electronic structure and the NIST BSE solver (OCEAN), was used to model the plasmonic and excited-state properties in TiO_2.[56,57] The package's workflow has been described previously.[37,38] A variable-cell relaxation of the TiO_2 anatase crystal structure was initially performed to define the suitable cell parameters. As part of the workflow, Quantum ESPRESSO[58,59] performed density functional theory (DFT) to calculate the ground-state electronic structure using a plane-wave basis set and a 350 Ry cutoff energy. The DFT used

Trouiller-Martins norm-conserving pseudopotentials, calculated using a Perdew-Wang local density approximation (LDA). A 16×16×12 *k*-point mesh was used with 248 total bands. The macroscopic dielectric constant was set to 5.62 for TiO_2 anatase.[60] The Haydock solver is used to calculate all X-ray spectra. The spin-orbit coupling for all BSE calculations was fixed as 4.5 eV. See the Supporting Information for input parameters of the cutoff energy convergence, BSE screening, variable-cell relaxation, and band structure calculations.

The standard OCEAN code can interpret static lattice heating by re-running the DFT and BSE calculations for lattice parameters that simulate an isotropic thermal lattice expansion. However, our previous reports discuss the modified BSE code that simulates excited-state electrons and holes.[26,37,38] The standard code is modified to output the band structure as a usable *k*-point mesh array with defined energy values for each *k*-point. This array is then evaluated and modified to include an excited-state carrier population through state filling. Specifically, photoexcited electrons are simulated by blocking available transitions in the conduction band while holes are simulated by opening or making states available in the valence band. It is worth noting that the state filling fully occupies each state whereas a partial occupation would more accurately depict a carrier density. We use an iterative approach to state filling in MATLAB, which fills all conduction states up to a specified energy or opens valence states for holes. However, this method is complicated for band structures with degenerate valleys across *k*-space because the *k*-point mesh in OCEAN is unsorted. In other words, degenerate valleys would be unavoidably filled with excited-state electrons, and the simulated excitation would not be momentum-specific.

After the X-ray absorption spectra are calculated, they are broadened to account for the experimental lifetime broadening of the TiO_2 Ti $L_{2,3}$ edge.[36] The theoretical differential absorption is then calculated as the log of the excited-state spectrum divided by the ground-state spectrum. The mean squared error (MSE) between the calculation and experiment is calculated using MATLAB's 'goodnessOfFit' function. See the Supporting Information for the lattice expansion parameters, state-filling simulations/scripts, spectral broadening procedure, and MSE calculations.

2.5 Supporting Information

The supporting information, containing figures and data labelled S[X], is available free of charge at: https://doi.org/10.22002/wheak-c7d39

2.6 References

(1) Shah, J. *Ultrafast Spectroscopy of Semiconductors and Semiconductor Nanostructures*; Cardona, M., Fulde, P., Von Klitzing, K., Queisser, H.-J., Merlin, R., Störmer, H., Series Eds.; Springer Series in Solid-State Sciences; Springer: Berlin, Heidelberg, 1999; Vol. 115. https://doi.org/10.1007/978-3-662-03770-6.

(2) Hartland, G. V.; Besteiro, L. V.; Johns, P.; Govorov, A. O. What's so Hot about Electrons in Metal Nanoparticles? *ACS Energy Lett.* **2017**, *2* (7), 1641–1653. https://doi.org/10.1021/acsenergylett.7b00333.

(3) Sundararaman, R.; Narang, P.; Jermyn, A. S.; Goddard III, W. A.; Atwater, H. A. Theoretical Predictions for Hot-Carrier Generation from Surface Plasmon Decay. *Nat. Commun.* **2014**, *5* (1), 5788. https://doi.org/10.1038/ncomms6788.

(4) Chen, S.; Wang, L.-W. Thermodynamic Oxidation and Reduction Potentials of Photocatalytic Semiconductors in Aqueous Solution. *Chem. Mater.* **2012**, *24* (18), 3659–3666. https://doi.org/10.1021/cm302533s.

(5) Li, M.; Bhaumik, S.; Goh, T. W.; Kumar, M. S.; Yantara, N.; Grätzel, M.; Mhaisalkar, S.; Mathews, N.; Sum, T. C. Slow Cooling and Highly Efficient Extraction of Hot Carriers in Colloidal Perovskite Nanocrystals. *Nat. Commun.* **2017**, *8* (1), 14350. https://doi.org/10.1038/ncomms14350.

(6) Zhang, Y.; He, S.; Guo, W.; Hu, Y.; Huang, J.; Mulcahy, J. R.; Wei, W. D. Surface-Plasmon-Driven Hot Electron Photochemistry. *Chem. Rev.* **2018**, *118* (6), 2927–2954. https://doi.org/10.1021/acs.chemrev.7b00430.

(7) Amidani, L.; Naldoni, A.; Malvestuto, M.; Marelli, M.; Glatzel, P.; Dal Santo, V.; Boscherini, F. Probing Long-Lived Plasmonic-Generated Charges in TiO_2/Au by High-Resolution X-Ray Absorption Spectroscopy. *Angew. Chem. Int. Ed.* **2015**, *54* (18), 5413–5416. https://doi.org/10.1002/anie.201412030.

(8) Priebe, J. B.; Karnahl, M.; Junge, H.; Beller, M.; Hollmann, D.; Brückner, A. Water Reduction with Visible Light: Synergy between Optical Transitions and Electron Transfer in Au-TiO_2 Catalysts Visualized by In Situ EPR Spectroscopy. *Angew. Chem. Int. Ed.* **2013**, *52* (43), 11420–11424. https://doi.org/10.1002/anie.201306504.

(9) Li, B.; Li, H.; Yang, C.; Ji, B.; Lin, J.; Tomie, T. Excited States in the Conduction Band and Long-Lifetime Hot Electrons in TiO_2 Nanoparticles Observed with Photoemission Electron Microscopy. *AIP Adv.* **2019**, *9* (8), 085321. https://doi.org/10.1063/1.5120378.

(10) Yin, J.; Maity, P.; Naphade, R.; Cheng, B.; He, J.-H.; Bakr, O. M.; Brédas, J.-L.; Mohammed, O. F. Tuning Hot Carrier Cooling Dynamics by Dielectric Confinement in Two-Dimensional Hybrid Perovskite Crystals. *ACS Nano* **2019**, *13* (11), 12621–12629. https://doi.org/10.1021/acsnano.9b04085.

(11) Besteiro, L. V.; Yu, P.; Wang, Z.; Holleitner, A. W.; Hartland, G. V.; Wiederrecht, G. P.; Govorov, A. O. The Fast and the Furious: Ultrafast Hot Electrons in Plasmonic Metastructures. Size and Structure Matter. *Nano Today* **2019**, *27*, 120–145. https://doi.org/10.1016/j.nantod.2019.05.006.

(12) Chang, L.; Besteiro, L. V.; Sun, J.; Santiago, E. Y.; Gray, S. K.; Wang, Z.; Govorov, A. O. Electronic Structure of the Plasmons in Metal Nanocrystals: Fundamental Limitations for the Energy Efficiency of Hot Electron Generation. *ACS Energy Lett.* **2019**, *4* (10), 2552–2568. https://doi.org/10.1021/acsenergylett.9b01617.

(13) Linic, S.; Chavez, S.; Elias, R. Flow and Extraction of Energy and Charge Carriers in Hybrid Plasmonic Nanostructures. *Nat. Mater.* **2021**, *20* (7), 916–924. https://doi.org/10.1038/s41563-020-00858-4.

(14) He, W.; Cai, J.; Jiang, X.; Yin, J.-J.; Meng, Q. Generation of Reactive Oxygen Species and Charge Carriers in Plasmonic Photocatalytic Au@TiO_2 Nanostructures with Enhanced Activity. *Phys. Chem. Chem. Phys.* **2018**, *20* (23), 16117–16125. https://doi.org/10.1039/C8CP01978A.

(15) Kamimura, S.; Miyazaki, T.; Zhang, M.; Li, Y.; Tsubota, T.; Ohno, T. (Au@Ag)@Au Double Shell Nanoparticles Loaded on Rutile TiO_2 for Photocatalytic Decomposition of 2-Propanol under Visible Light Irradiation. *Appl. Catal. B Environ.* **2016**, *180*, 255–262. https://doi.org/10.1016/j.apcatb.2015.06.037.

(16) Wei, D.; Tan, Y.; Wang, Y.; Kong, T.; Shen, S.; Mao, S. S. Function-Switchable Metal/Semiconductor Junction Enables Efficient Photocatalytic Overall Water Splitting with Selective Water Oxidation Products. *Sci. Bull.* **2020**, *65* (16), 1389–1395. https://doi.org/10.1016/j.scib.2020.04.042.

(17) Mali, S. S.; Shim, C. S.; Kim, H.; Patil, P. S.; Hong, C. K. In Situ Processed Gold Nanoparticle-Embedded TiO2 Nanofibers Enabling Plasmonic Perovskite Solar Cells to Exceed 14% Conversion Efficiency. *Nanoscale* **2016**, *8* (5), 2664–2677. https://doi.org/10.1039/C5NR07395B.

(18) Li, Y.; DiStefano, J. G.; Murthy, A. A.; Cain, J. D.; Hanson, E. D.; Li, Q.; Castro, F. C.; Chen, X.; Dravid, V. P. Superior Plasmonic Photodetectors Based on Au@MoS_2 Core–Shell Heterostructures. *ACS Nano* **2017**, *11* (10), 10321–10329. https://doi.org/10.1021/acsnano.7b05071.

(19) Pettine, J.; Maioli, P.; Vallée, F.; Del Fatti, N.; Nesbitt, D. J. Energy-Resolved Femtosecond Hot Electron Dynamics in Single Plasmonic Nanoparticles. *ACS Nano* **2023**, *17* (11), 10721–10732. https://doi.org/10.1021/acsnano.3c02062.

(20) Tan, S.; Argondizzo, A.; Ren, J.; Liu, L.; Zhao, J.; Petek, H. Plasmonic Coupling at a Metal/Semiconductor Interface. *Nat. Photon.* **2017**, *11* (12), 806–812. https://doi.org/10.1038/s41566-017-0049-4.

(21) Richter, J. M.; Branchi, F.; Valduga de Almeida Camargo, F.; Zhao, B.; Friend, R. H.; Cerullo, G.; Deschler, F. Ultrafast Carrier Thermalization in Lead Iodide Perovskite Probed with Two-Dimensional Electronic Spectroscopy. *Nat. Commun.* **2017**, *8* (1), 376. https://doi.org/10.1038/s41467-017-00546-z.

(22) Taghinejad, M.; Xia, C.; Hrton, M.; Lee, K.-T.; Kim, A. S.; Li, Q.; Guzelturk, B.; Kalousek, R.; Xu, F.; Cai, W.; Lindenberg, A. M.; Brongersma, M. L. Determining Hot-Carrier Transport Dynamics from Terahertz Emission. *Science* **2023**, *382* (6668), 299–305. https://doi.org/10.1126/science.adj5612.

(23) Cushing, S. K.; Porter, I. J.; de Roulet, B. R.; Lee, A.; Marsh, B. M.; Szoke, S.; Vaida, M. E.; Leone, S. R. Layer-Resolved Ultrafast Extreme Ultraviolet Measurement of Hole Transport in a Ni-TiO_2-Si Photoanode. *Sci. Adv.* **2020**, *6* (14), eaay6650. https://doi.org/10.1126/sciadv.aay6650.

(24) Lin, M.-F.; Verkamp, M. A.; Leveillee, J.; Ryland, E. S.; Benke, K.; Zhang, K.; Weninger, C.; Shen, X.; Li, R.; Fritz, D.; Bergmann, U.; Wang, X.; Schleife, A.; Vura-Weis, J. Carrier-Specific Femtosecond XUV Transient Absorption of PbI_2 Reveals Ultrafast Nonradiative Recombination. *J. Phys. Chem. C* **2017**, *121* (50), 27886–27893. https://doi.org/10.1021/acs.jpcc.7b11147.

(25) Zürch, M.; Chang, H.-T.; Kraus, P. M.; Cushing, S. K.; Borja, L. J.; Gandman, A.; Kaplan, C. J.; Oh, M. H.; Prell, J. S.; Prendergast, D.; Pemmaraju, C. D.; Neumark, D. M.; Leone, S. R. Ultrafast Carrier Thermalization and Trapping in Silicon-Germanium Alloy Probed by Extreme Ultraviolet Transient Absorption Spectroscopy. *Struct. Dyn.* **2017**, *4* (4), 044029. https://doi.org/10.1063/1.4985056.

(26) Liu, H.; Michelsen, J. M.; Mendes, J. L.; Klein, I. M.; Bauers, S. R.; Evans, J. M.; Zakutayev, A.; Cushing, S. K. Measuring Photoexcited Electron and Hole Dynamics in ZnTe and Modeling Excited State Core-Valence Effects in Transient Extreme

Ultraviolet Reflection Spectroscopy. *J. Phys. Chem. Lett.* **2023**, *14* (8), 2106–2111. https://doi.org/10.1021/acs.jpclett.2c03894.

(27) Park, S. H.; Katoch, A.; Chae, K. H.; Gautam, S.; Miedema, P.; Cho, S. W.; Kim, M.; Wang, R.-P.; Lazemi, M.; de Groot, F.; Kwon, S. Direct and Real-Time Observation of Hole Transport Dynamics in Anatase TiO_2 Using X-Ray Free-Electron Laser. *Nat. Commun.* **2022**, *13* (1), 2531. https://doi.org/10.1038/s41467-022-30336-1.

(28) Cushing, S. K.; Li, J.; Bright, J.; Yost, B. T.; Zheng, P.; Bristow, A. D.; Wu, N. Controlling Plasmon-Induced Resonance Energy Transfer and Hot Electron Injection Processes in Metal@TiO_2 Core–Shell Nanoparticles. *J. Phys. Chem. C* **2015**, *119* (28), 16239–16244. https://doi.org/10.1021/acs.jpcc.5b03955.

(29) Cushing, S. K.; Chen, C.-J.; Dong, C. L.; Kong, X.-T.; Govorov, A. O.; Liu, R.-S.; Wu, N. Tunable Nonthermal Distribution of Hot Electrons in a Semiconductor Injected from a Plasmonic Gold Nanostructure. *ACS Nano* **2018**, *12* (7), 7117–7126. https://doi.org/10.1021/acsnano.8b02939.

(30) Zhou, J.-J.; Park, J.; Lu, I.-T.; Maliyov, I.; Tong, X.; Bernardi, M. Perturbo: A Software Package for *Ab Initio* Electron–Phonon Interactions, Charge Transport and Ultrafast Dynamics. *Comput. Phys. Commun.* **2021**, *264*, 107970. https://doi.org/10.1016/j.cpc.2021.107970.

(31) Leenheer, A. J.; Narang, P.; Lewis, N. S.; Atwater, H. A. Solar Energy Conversion via Hot Electron Internal Photoemission in Metallic Nanostructures: Efficiency Estimates. *J. Appl. Phys.* **2014**, *115* (13), 134301. https://doi.org/10.1063/1.4870040.

(32) Zheng, B. Y.; Zhao, H.; Manjavacas, A.; McClain, M.; Nordlander, P.; Halas, N. J. Distinguishing between Plasmon-Induced and Photoexcited Carriers in a Device Geometry. *Nat. Commun.* **2015**, *6* (1), 7797. https://doi.org/10.1038/ncomms8797.

(33) Varache, R.; Leendertz, C.; Gueunier-Farret, M. E.; Haschke, J.; Muñoz, D.; Korte, L. Investigation of Selective Junctions Using a Newly Developed Tunnel Current Model for Solar Cell Applications. *Sol. Energy Mater. Sol. Cells* **2015**, *141*, 14–23. https://doi.org/10.1016/j.solmat.2015.05.014.

(34) Hirose, M. Electron Tunneling through Ultrathin SiO_2. *Mater. Sci. Eng. B* **1996**, *41* (1), 35–38. https://doi.org/10.1016/S0921-5107(96)01619-4.

(35) De Groot, F. M. F.; Grioni, M.; Fuggle, J. C.; Ghijsen, J.; Sawatzky, G. A.; Petersen, H. Oxygen 1*s* x-Ray-Absorption Edges of Transition-Metal Oxides. *Phys. Rev. B* **1989**, *40* (8), 5715–5723. https://doi.org/10.1103/PhysRevB.40.5715.

(36) Leapman, R. D.; Grunes, L. A.; Fejes, P. L. Study of the $L_{2,3}$ Edges in the 3*d* Transition Metals and Their Oxides by Electron-Energy-Loss Spectroscopy with Comparisons to Theory. *Phys. Rev. B* **1982**, *26* (2), 614–635. https://doi.org/10.1103/PhysRevB.26.614.

(37) Klein, I. M.; Liu, H.; Nimlos, D.; Krotz, A.; Cushing, S. K. Ab Initio Prediction of Excited-State and Polaron Effects in Transient XUV Measurements of α-Fe_2O_3. *J. Am. Chem. Soc.* **2022**, *144* (28), 12834–12841. https://doi.org/10.1021/jacs.2c03994.

(38) Klein, I. M.; Krotz, A.; Lee, W.; Michelsen, J. M.; Cushing, S. K. Ab Initio Calculations of XUV Ground and Excited States for First-Row Transition Metal Oxides. *J. Phys. Chem. C* **2023**, *127* (2), 1077–1086. https://doi.org/10.1021/acs.jpcc.2c06548.

(39) Barnard, A. S.; Curtiss, L. A. Prediction of TiO_2 Nanoparticle Phase and Shape Transitions Controlled by Surface Chemistry. *Nano Lett.* **2005**, *5* (7), 1261–1266. https://doi.org/10.1021/nl050355m.

(40) Zhang, H.; Banfield, J. F. Understanding Polymorphic Phase Transformation Behavior during Growth of Nanocrystalline Aggregates: Insights from TiO_2. *J. Phys. Chem. B* **2000**, *104* (15), 3481–3487. https://doi.org/10.1021/jp000499j.

(41) Zhang, H.; Banfield, J. F. Thermodynamic Analysis of Phase Stability of Nanocrystalline Titania. *J. Mater. Chem.* **1998**, *8* (9), 2073–2076. https://doi.org/10.1039/A802619J.

(42) Zhang, H.; Chen, B.; Banfield, J. F.; Waychunas, G. A. Atomic Structure of Nanometer-Sized Amorphous TiO_2. *Phys. Rev. B* **2008**, *78* (21), 214106. https://doi.org/10.1103/PhysRevB.78.214106.

(43) Gloter, A.; Ewels, C.; Umek, P.; Arcon, D.; Colliex, C. Electronic Structure of Titania-Based Nanotubes Investigated by EELS Spectroscopy. *Phys. Rev. B* **2009**, *80* (3), 035413. https://doi.org/10.1103/PhysRevB.80.035413.

(44) Nunez, P.; Richter, M. H.; Piercy, B. D.; Roske, C. W.; Cabán-Acevedo, M.; Losego, M. D.; Konezny, S. J.; Fermin, D. J.; Hu, S.; Brunschwig, B. S.; Lewis, N. S. Characterization of Electronic Transport through Amorphous TiO_2 Produced by Atomic Layer Deposition. *J. Phys. Chem. C* **2019**, *123* (33), 20116–20129. https://doi.org/10.1021/acs.jpcc.9b04434.

(45) Hu, S.; Richter, M. H.; Lichterman, M. F.; Beardslee, J.; Mayer, T.; Brunschwig, B. S.; Lewis, N. S. Electrical, Photoelectrochemical, and Photoelectron Spectroscopic Investigation of the Interfacial Transport and Energetics of Amorphous TiO_2/Si

Heterojunctions. *J. Phys. Chem. C* **2016**, *120* (6), 3117–3129. https://doi.org/10.1021/acs.jpcc.5b09121.

(46) Vlachos, D.; Craven, A. J.; McComb, D. W. Specimen Charging in X-Ray Absorption Spectroscopy: Correction of Total Electron Yield Data from Stabilized Zirconia in the Energy Range 250–915 eV. *J. Synchrotron Rad.* **2005**, *12* (2), 224–233. https://doi.org/10.1107/S0909049504030146.

(47) Frazer, B. H.; Gilbert, B.; Sonderegger, B. R.; De Stasio, G. The Probing Depth of Total Electron Yield in the Sub-keV Range: TEY-XAS and X-PEEM. *Surface Science* **2003**, *537* (1), 161–167. https://doi.org/10.1016/S0039-6028(03)00613-7.

(48) Govorov, A. O.; Richardson, H. H. Generating Heat with Metal Nanoparticles. *Nano Today* **2007**, *2* (1), 30–38. https://doi.org/10.1016/S1748-0132(07)70017-8.

(49) Hummer, D. R.; Heaney, P. J.; Post, J. E. Thermal Expansion of Anatase and Rutile between 300 and 575 K Using Synchrotron Powder X-Ray Diffraction. *Powder Diffr.* **2007**, *22* (4), 352–357. https://doi.org/10.1154/1.2790965.

(50) Zeng, N.; Murphy, A. B. Heat Generation by Optically and Thermally Interacting Aggregates of Gold Nanoparticles under Illumination. *Nanotechnology* **2009**, *20* (37), 375702. https://doi.org/10.1088/0957-4484/20/37/375702.

(51) Jørgensen, J. T.; Norregaard, K.; Tian, P.; Bendix, P. M.; Kjaer, A.; Oddershede, L. B. Single Particle and PET-Based Platform for Identifying Optimal Plasmonic Nano-Heaters for Photothermal Cancer Therapy. *Sci. Rep.* **2016**, *6* (1), 30076. https://doi.org/10.1038/srep30076.

(52) Yu, L.; Du, A.; Yang, L.; Hu, Y.; Xie, W. Quantifying Hot Electron Energy Contributions in Plasmonic Photocatalysis Using Electrochemical Surface-Enhanced Raman Spectroscopy. *J. Phys. Chem. Lett.* **2022**, *13* (24), 5495–5500. https://doi.org/10.1021/acs.jpclett.2c01213.

(53) Warkentin, C. L.; Frontiera, R. R. Quantifying the Ultrafast and Steady-State Molecular Reduction Potential of a Plasmonic Photocatalyst. *Proc. Natl. Acad. Sci. U.S.A.* **2023**, *120* (44), e2305932120. https://doi.org/10.1073/pnas.2305932120.

(54) Bertoluzzi, L.; Herraiz-Cardona, I.; Gottesman, R.; Zaban, A.; Bisquert, J. Relaxation of Electron Carriers in the Density of States of Nanocrystalline TiO_2. *J. Phys. Chem. Lett.* **2014**, *5* (4), 689–694. https://doi.org/10.1021/jz4027584.

(55) Selberherr, S. *Analysis and Simulation of Semiconductor Devices*; Springer Science & Business Media, 1984. https://doi.org/10.1007/978-3-7091-8752-4

(56) Vinson, J.; Rehr, J. J.; Kas, J. J.; Shirley, E. L. Bethe-Salpeter Equation Calculations of Core Excitation Spectra. *Phys. Rev. B* **2011**, *83* (11), 115106. https://doi.org/10.1103/PhysRevB.83.115106.

(57) Gilmore, K.; Vinson, J.; Shirley, E. L.; Prendergast, D.; Pemmaraju, C. D.; Kas, J. J.; Vila, F. D.; Rehr, J. J. Efficient Implementation of Core-Excitation Bethe–Salpeter Equation Calculations. *Comput. Phys. Commun.* **2015**, *197*, 109–117. https://doi.org/10.1016/j.cpc.2015.08.014.

(58) Giannozzi, P.; Baroni, S.; Bonini, N.; Calandra, M.; Car, R.; Cavazzoni, C.; Ceresoli, D.; Chiarotti, G. L.; Cococcioni, M.; Dabo, I.; Corso, A. D.; Gironcoli, S. de; Fabris, S.; Fratesi, G.; Gebauer, R.; Gerstmann, U.; Gougoussis, C.; Kokalj, A.; Lazzeri, M.; Martin-Samos, L.; Marzari, N.; Mauri, F.; Mazzarello, R.; Paolini, S.; Pasquarello, A.; Paulatto, L.; Sbraccia, C.; Scandolo, S.; Sclauzero, G.; Seitsonen, A. P.; Smogunov, A.; Umari, P.; Wentzcovitch, R. M. QUANTUM ESPRESSO: A Modular and Open-Source Software Project for Quantum Simulations of Materials. *J. Phys.: Condens. Matter* **2009**, *21* (39), 395502. https://doi.org/10.1088/0953-8984/21/39/395502.

(59) Giannozzi, P.; Andreussi, O.; Brumme, T.; Bunau, O.; Buongiorno Nardelli, M.; Calandra, M.; Car, R.; Cavazzoni, C.; Ceresoli, D.; Cococcioni, M.; Colonna, N.; Carnimeo, I.; Dal Corso, A.; de Gironcoli, S.; Delugas, P.; DiStasio, R. A.; Ferretti, A.; Floris, A.; Fratesi, G.; Fugallo, G.; Gebauer, R.; Gerstmann, U.; Giustino, F.; Gorni, T.; Jia, J.; Kawamura, M.; Ko, H.-Y.; Kokalj, A.; Küçükbenli, E.; Lazzeri, M.; Marsili, M.; Marzari, N.; Mauri, F.; Nguyen, N. L.; Nguyen, H.-V.; Otero-de-la-Roza, A.; Paulatto, L.; Poncé, S.; Rocca, D.; Sabatini, R.; Santra, B.; Schlipf, M.; Seitsonen, A. P.; Smogunov, A.; Timrov, I.; Thonhauser, T.; Umari, P.; Vast, N.; Wu, X.; Baroni, S. Advanced Capabilities for Materials Modelling with Quantum ESPRESSO. *J. Phys.: Condens. Matter* **2017**, *29* (46), 465901. https://doi.org/10.1088/1361-648X/aa8f79.

(60) Wemple, S. H. Optical Oscillator Strengths and Excitation Energies in Solids, Liquids, and Molecules. *J. Chem. Phys.* **2008**, *67* (5), 2151–2168. https://doi.org/10.1063/1.435102.

C H A P T E R 3

NANOSCALE AND ELEMENT-SPECIFIC LATTICE TEMPERATURE MEASUREMENTS USING CORE-LOSS ELECTRON ENERGY-LOSS SPECTROSCOPY

Adapted with permission from the following:

Palmer, L. D.; Lee, W.; Durham, D. B.; Fajardo, J., Jr.; Liu, Y.; Talin, A. A.; Gage, T. E.; Cushing, S. K. Nanoscale and Element-Specific Lattice Temperature Measurements using Core-Loss Electron Energy-Loss Spectroscopy. *ACS Phys. Chem. Au* **2025**, *5* (6), 589–598. https://doi.org/10.1021/acsphyschemau.5c00044.

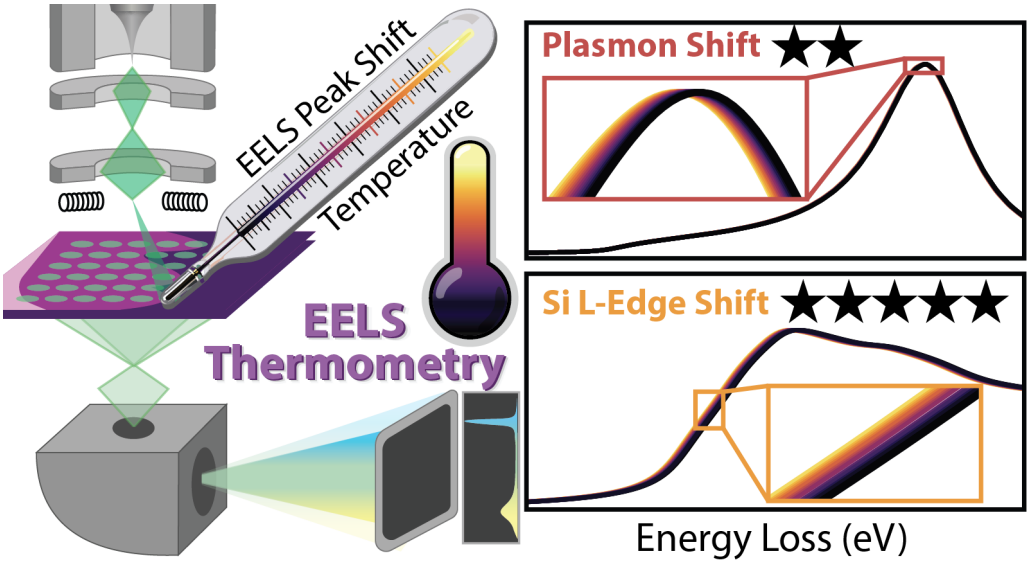

3.1 Introduction

Accurate temperature measurements at the nanoscale are essential for understanding and managing thermal gradients in modern electronic, photonic, and energy conversion/storage devices. During operation, local thermal variations significantly influence device performance and reliability. For example, the breakdown of Dennard scaling for transistors and the increasing challenge of heat removal have limited transistor density and clock speeds in central processing units since the early 2000s.[1] Similarly, semiconductor devices used in transportation, renewable energy systems, and the electric grid require precise thermal control to ensure efficient switching and prevent degradation.[2] In contrast, modest temperature increases in semiconductor-based photocatalytic systems have recently been reported to substantially improve solar hydrogen generation.[3,4] Understanding when local heating is detrimental or beneficial to each application requires robust and accurate *in situ* temperature measurements with nanometer spatial resolution.

Plasmon energy expansion thermometry (PEET) is one technique that, in principle, enables sub-nm thermal imaging.[5–10] PEET measures temperature-induced shifts in a material's volume plasmon energy according to the free electron model following thermal expansion. In a scanning TEM (STEM) with electron energy-loss spectroscopy (EELS), PEET has been used to image nanoscale temperatures and thermal lattice expansion coefficients for nanoparticles, membranes, and two-dimensional materials.[5–11] Time-resolved PEET is also possible in optically-coupled electron microscopes.[12] However, recent studies show that the volume plasmon can vary with sample thickness and local dielectric properties.[13] The resolution in momentum (k) space can also obscure accurate PEET measurements because plasmon energies typically vary quadratically with momentum.[14–16] Local strain can also exceed the thermal expansion, especially at junctions and interfaces.[17] PEET also has difficulty measuring temperature in materials with small thermal expansion coefficients that result in <0.1 meV/K plasmon energy shifts. PEET's challenges necessitate additional spectromicroscopy tools for nanoscale thermal imaging.[18]

We propose core-loss thermometry as a complementary or alternative method to PEET that also has expanded utility at X-ray beamlines. Core-loss edges, such as those measured by core-loss EELS and X-ray absorption, are sensitive to changes in a material's electronic structure and valence states. While extended X-ray absorption fine structure (EXAFS) spectra can quantify lattice temperatures, its need for high-energy core-level transitions prohibit the signal and spatial resolution for core-loss EELS.[19,20] Ultrafast and photoexcited X-ray spectroscopy studies have found that core-level edges of semiconductors redshift with temperature, but the exact redshift mechanism is not well understood.[21–23] We aim to understand and predict this temperature-dependent redshift using EELS simulations to develop core-loss thermometry.

In this work, we use *in situ* STEM-EELS with controlled temperature-dependent low- and core-loss EEL spectra across multiple thickness regions of a crystalline Si lamella with native oxide. We evaluate PEET's and core-loss thermometry's accuracy across different thickness regions of the lamella and extract temperature-induced shifts of the Si $L_{2,3}$ edge ($2p \rightarrow 3s+d$ transition). To interpret these shifts, we incorporate *ab initio* simulations of the Si plasmon and $L_{2,3}$ edge using density functional theory (DFT), linearized time-dependent DFT (TDDFT), and the Bethe-Salpeter equation (BSE). Our analysis finds that the core-loss spectrum redshifts according to the reduction of Si temperature-dependent bandgap as predicted by the Varshni equation.[24,25] Compared to PEET, core-loss thermometry of semiconductors is less sensitive to effects from multiple plasmons, multiple scattering, temperature-dependent strain, small thermal expansion coefficients, surface contamination, and multi-element stacked junctions. We also find core-loss thermometry more accurate than PEET at measuring the thermal expansion coefficient when the temperature-dependent dielectric constant and environment are not fully characterized. Further, a standard spectral denoising algorithm can improve core-loss thermometry's accuracy. Ultimately, core-loss thermometry is a promising route for element-specific, nanoscale temperature mapping during operando or ultrafast measurements.

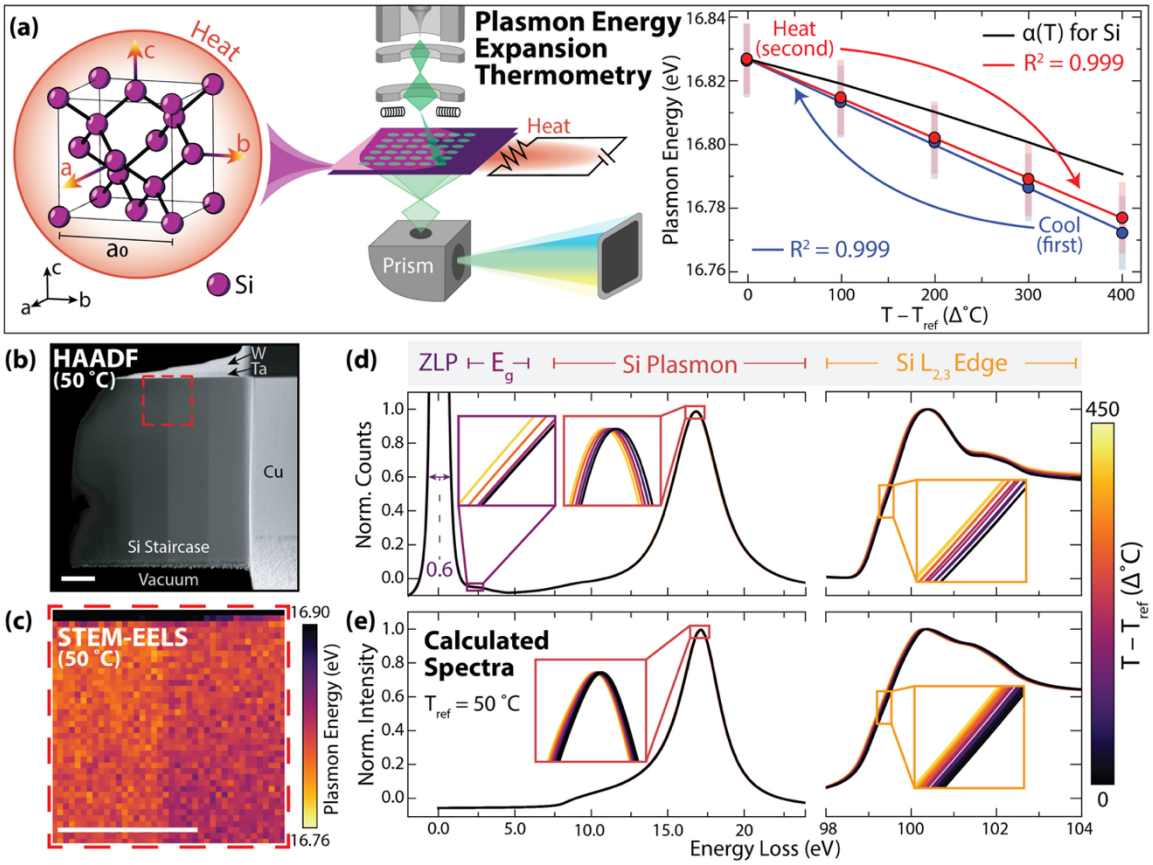

Figure 3.1. Temperature-dependent scanning TEM electron energy-loss spectroscopy (STEM-EELS). (**a**) Plasmon energy expansion thermometry: thermal expansion of crystalline Si due to resistive heating is measured by STEM-EELS using a cold field-emission gun. The inset depicts the image-averaged plasmon energy shift while heating and cooling the Si lamella as compared to the plasmon energy calculated using the temperature-dependent thermal expansion coefficient (α(T)). Shaded bars are the plasmon energy standard deviation in each STEM image, and error bars were calculated using reduced χ^2 but smaller than each datapoint, T_{ref} = 50˚C. (**b**) A high-angular annular dark-field STEM image of the membrane at T_{ref}, with the Cu grid, 200 nm Ta, and a W capping layer apparent as bright contrast. The dashed red square represents the STEM-EELS acquisition region in (**c**). Scale bars are 1 μm. False coloration represents hot colors as "warmer" sample regions, and Lorentzian fits were used to determine the plasmon energy. See supplementary movies for temperature-dependent dark-field and plasmon energy images. (**d**) Temperature-dependent spectra of the Si lamella collected using dualEELS and aligned to the zero-loss

peak (ZLP). Each spectrum is an average of spectra in each 40×40 pixel STEM-EELS image with the first two rows used for image alignment. The direct bandgap (E_g) and Si $L_{2,3}$ edge are power-law background-subtracted. (**e**) Calculated Si EEL spectra modeled over a range of expanded lattice parameters using the temperature-dependent, isotropic thermal expansion coefficient of Si [ref. 27]. The unit cell's energy-optimized lattice parameter (a_0) was 10.33 Bohr (5.47 Å). A scissor shift was applied to the calculated Si $L_{2,3}$ edge according to the temperature-dependent band gap [ref. 24], and the edge was broadened by an energy-dependent Lorentzian broadening.

3.2 Results

Figure 3.1 depicts the experimental setup used to measure PEET and core-loss thermometry. When integrated with STEM-EELS, PEET can accurately map the plasmon energy shift (**Figure 3.1a**). The measured dual-thickness Si lamella (82.5 ± 2.2 and 106.0 ± 3.5 nm thicknesses) with native oxide was prepared by focused ion beam lift out, thinning, and polishing of >10 kΩ · cm Si (<4.4×10^{11} cm^{-3} intrinsic N_D).[26] The inset shows that the Si plasmon energy redshifts linearly with increasing temperature with minor hysteresis across the thermal sweep.

The volume plasmon energy (E_p) redshifts due to thermal lattice expansion according to the free electron model in **Eq. 3.1**:

$$E_p(T) = \hbar\omega_p(T) = \hbar\sqrt{\frac{n(T)e^2}{m_{eff}\epsilon_\infty}}. \quad (3.1)$$

As the Si lattice expands, the carrier density n(T) decreases (ϵ_∞, e, and m_{eff} are the specimen's dielectric constant, electron charge, and valence band effective mass, respectively). The electron's temperature-dependent effective mass and dielectric constant vary with temperature but are typically ignored by PEET studies by interpreting the *relative* change in the plasmon energy according to the thermal expansion coefficient α(T) using **Eq. 3.2**:

$$E_p(T) = E_{p0} * \left(1 - \frac{3}{2} * \int_{T_{ref}}^{T} \alpha(T) dT\right). \quad (3.2)$$

Here, E_{p0} is the plasmon energy at the reference temperature (T_{ref}) and $\alpha(T)$ is the temperature-dependent thermal expansion coefficient of Si.[27] **Equation 3.2** was used to calculate the temperature-dependent plasmon energy, black trend-line in **Fig. 3.1a**(inset). However, it is apparent that the plasmon shifts 1 meV, or ~25%, more than the predicted value over this temperature range. This shift could be due to a wide variety of factors. The plasmon's absolute energy and redshift can only be directly related to the thermal lattice expansion if approximations for fixed momentum, strain, and dielectric environment across the specimen hold true. We believe that the lamella contains built-in stress from milling and welding with materials of differing thermal expansion coefficients that manifests as temperature-dependent tensile strain. The inset also features two types of error bars (1) capped and (2) shaded. The capped error bars were calculated using a reduced χ^2 analysis of the averaged data points' deviation from a linear fit, normalized to the degrees of freedom but are largely unnoticeable due to the minimal error. The shaded error bars are the standard deviation of the plasmon energy calculated across all the pixels in the STEM-EELS image at each temperature. About half of this ~13 meV standard deviation results from the two different thicknesses of the Si staircase measured in **Figure 3.1b**. The Si surface-to-volume ratio is thickness dependent because the Si surface plasmon near 10 eV redshifts the volume plasmon with decreasing thickness. The other half of the ~13 meV standard deviation results from suboptimal signal-to-noise ratio in peak fitting. Although each pixel's plasmon signal-to-noise is comparable to other manuscripts in this field, μeV accuracy is needed to properly perform PEET. The experimental PEET uncertainty would improve using higher magnification over a uniform thickness region and dualEELS to separately acquire the ZLP and plasmon spectra.

STEM-EELS (**Figure 3.1b,c**) was performed on an electron-transparent region of the Si lamella over two different regions of uniform thickness, as indicated by the dashed red square in the high-angle annular dark-field (HAADF) image survey. The 40×40 pixel STEM-EELS

image in **Figure 3.1c** was collected with the sample at T_{ref} = 50 ˚C. The plasmon energy was determined for each pixel where the zero-loss peak (ZLP) was aligned using a center-of-mass fit, three Lorentzian functions were used to fit the Si plasmon peaks, and the energy difference of the ZLP and most intense, first plasmon peak was calculated (see Supplementary Information for fitting details). The thin and thick regions of the specimen are clearly apparent due to the plasmon energy differences. However, the thickness dependence has no noticeable effect on the plasmon energy difference with temperature (see movies in Supporting Information).

During the STEM-EELS mapping, dualEELS spectral acquisition allowed for sequential acquisition of the ZLP, plasmon, multiple scattering, and Si $L_{2,3}$ edge. The spectra averaged across each 40×40 px STEM-EELS image are shown in **Figure 3.1d**. Collecting the ZLP through dualEELS is highly critical for core-loss thermometry in a (S)TEM as it allows for longer acquisitions of the low-intensity core-loss spectrum while still offering a method for spectral alignment. The spectral redshift with temperature is apparent in the experimental and calculated plasmon and $L_{2,3}$ edge spectra (insets in **Figure 3.1d,e**).

The direct bandgap ($E_{g,direct}$) of Si, Si main plasmon, and Si $L_{2,3}$ edge are highlighted with insets showing the magnified features' redshifts. The Si surface plasmon around 10 eV is ignored, as well as the SiO_2 plasmon that is not resolvable at this thickness. Temperature-dependent spectra in **Figure 3.1e** were modeled using TDDFT for the ~16.8 eV volume plasmon (turboEELS) and DFT/BSE for the ~99 eV Si $L_{2,3}$ edge (OCEAN). Thermal lattice expansion was modeled using lattice parameters spanning a/a_0 = 1.000 – 1.002 according to the temperature-dependent thermal expansion coefficient.[27] The lattice parameter was the only input parameter modified across simulations, and the band gap was corrected after the calculation to account for the well-known band gap underestimation using DFT.[28] The reference lattice parameter (a_0 = 10.33 Bohr) was selected by minimizing the total cell energy.

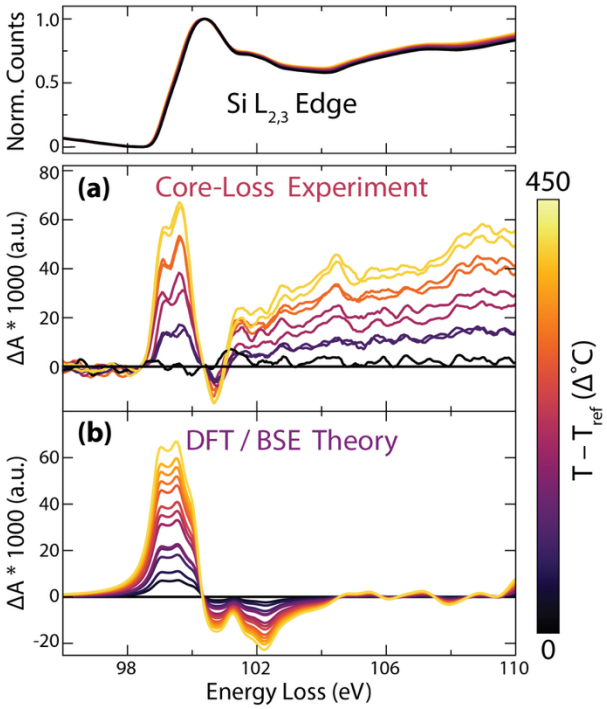

Figure 3.2. Si $L_{2,3}$ core-loss differential EEL spectra. (**a**) Measured and (**b**) modeled differential spectra of the Si $L_{2,3}$ edge from **Figure 3.1d,e**. Spectra are calculated as (A_T – A_{Tref}) × 1000. The measured differential is smoothed by a Savitsky-Golay filter (window = 17, order = 3). Two measurements were taken at each temperature, one for both the cooling and subsequent heating ramps in the **Figure 3.1a**, inset. Modeled spectra were calculated using *ab initio* DFT / BSE theory with a scissor shift applied according to the temperature-dependent band gap [ref. 24]. The as-measured temperature-dependent Si $L_{2,3}$ edge spectra are shown above for reference, and the measured spectra exclude any pixels over the Ta alignment layer.

The *ab initio* TDDFT calculations match the analytical approach for PEET as apparent in the **Figure 3.1e** insets. For PEET on Si, *ab initio* calculations are generally not needed as the thermal lattice expansion is well-studied.[6] However, more complex materials like transition metal oxides and multi-material stacks/interfaces that contain multiple plasmon and low-loss features are challenging to deconvolute. Instead, an *ab initio* TDDFT approach like the one used here would have to be applied.[7] Core-loss thermometry is therefore motivated because its element-specificity leads to well-separated spectral features in complex materials.

However, we first must test whether a simple analytical procedure can sufficiently predict the temperature-dependent core-loss spectra without relying on an *ab initio* approach.

Conceptually, the interpretation of temperature-dependent core-level spectra is complicated by complex dependencies of the specimen's band gap, band curvature, and dielectric function following thermal lattice expansion, lattice vibrational modes, and strain; thus, the mechanism for the previously reported redshift of core-level spectra with temperature remains unclear.[21–23] To help discern the origin of the redshift, we measure the temperature-dependent differential spectra and compare these results to calculated spectra using a DFT/BSE approach (**Figure 3.2**). The core-loss spectra were aligned for each STEM-EELS pixel using the center-of-mass-fit ZLP and averaged across each STEM-EELS map. This approach assumes that drift tube hysteresis does not occur tube at each pixel. The differential spectra were calculated by first normalizing each core-loss spectrum to span zero to one for the core-loss near edge's minimum and maximum. The spectrum at T_{ref} = 50 ˚C = ~325 K was then subtracted from the corresponding spectrum at each elevated temperature and multiplied by 1000 for visualization (**Figure 3.2a**). The differential spectra for the DFT/BSE-calculated spectra were similarly obtained (**Figure 3.2b**).

The differential spectra in **Figure 3.2** have positive features at the edge onset, indicating the redshift of the core-loss spectra with temperature and lattice expansion as apparent in the **Figure 3.1d,e** insets. The positive differential feature is almost identical to a rigid spectral shift (Figure S8), which suggests the conduction band's density of states is minimally modified at the measured temperatures. X-ray studies often normalize to an intensity far past the edge onset, but multiple scattering and temperature-dependent constructive interference effects in EELS prevented this normalization method.[29] These effects appear as increasing intensity with temperature beyond the edge (>101 eV). The DFT/BSE approach used here is also optimized for near-edge features instead of post-edge effects.

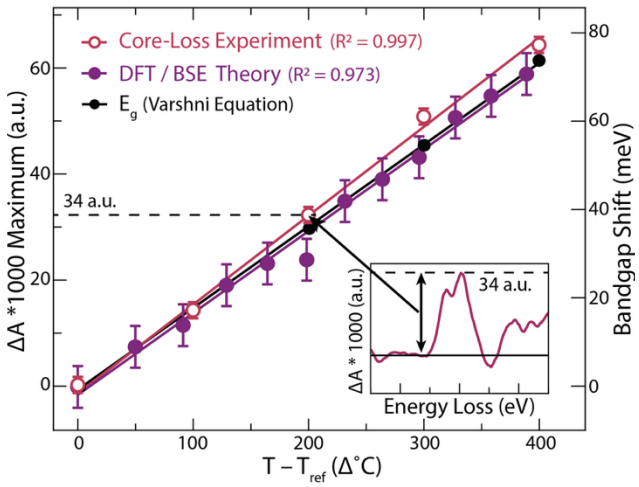

Figure 3.3. Comparing the modeled and measured Si $L_{2,3}$ edge's differential amplitude and redshift. The average maximum differential amplitude of the measured (magenta open circles) and simulated (purple filled circles) core-loss differential spectra from Figure 3.2. On the right axis, the amplitude is converted to the band gap's redshift according to a rigid shift model. The temperature-dependent band gap of Si from the Varshni equation is shown for reference (black filled circles). T_{ref} = 50 ˚C. The inset shows an example differential spectrum where the maximum amplitude was measured.

The maximum differential intensity is calculated to graph the relationship between the temperature-dependent band gap shift for the core-loss experiment and theory (**Figure 3.3**). To convert the differential intensity into the energy of the edge's redshift, a rigid shift of the spectrum at T_{ref} is performed (5 meV shift steps up to 150 meV), and linear regression is used to convert the differential intensity into the meV of the redshift. Both the measured and calculated core-loss spectra are found to follow the Varshni equation. A Varshni equation is an empirical formula that predicts a semiconductor's band gap (E_g) as a function of temperature (T).[24,25] A Varshni equation typically has the form $E_g = E_0 - (a \times T^2) / (T + b)$ where a and b are derived constants and E_0 is the band gap at 0 K. Whether experimentally measured or computationally derived, an accurate Varshni equation will take into consideration both the thermal lattice expansion and lattice vibrations from electron-phonon renormalization. For covalently bonded materials like Si, the electron-phonon vibrational term dominates because the lattice only minimally expands.

Figure 3.3 verifies that the core-loss redshift magnitude can be used to determine the Si lattice temperature according to the Varshni equation. Similarly, core-loss thermometry could enable a new approach to directly determine the constants in the Varshni equation for semiconductors with sub-nm resolution. By determining the constants for bulk specimens using simpler methods (e.g., quantifying the bandgap with UV-Vis spectroscopy), core-loss thermometry could then be used to derive the Varshni equation's empirical constants in compositionally complex materials without relying on DFT/BSE calculations.

The novelty of performing thermometry in the STEM is the ability to measure temperature with nanoscale precision, and thus, the accuracy of core-loss thermometry imaging must be tested. **Figure 3.4** compares the difference images for $\Delta T = 400$ ˚C. Our PEET imaging result (**Figure 3.4a**) indicates that the average temperature is measurable at 400 ± 68 ˚C, 17% error. This error is the standard deviation across the difference image, and it indicates that dualEELS is also necessary to improve the signal-to-noise ratio of plasmon spectra for accurate PEET. Notably, this error could be minimized by increasing the magnification and acquisition time, but the larger relative sample drift and beam-induced heating should still be considered. Minimal error resulted from the two different specimen thicknesses at this level of accuracy, which has been tested in the literature.[13] Each pixel was analyzed using Lorentzian fits of the Si plasmons, where the main plasmon's Lorentzian fit center at each temperature is a proxy for lattice temperature (**Figure 3.4b**). The PEET image is generated by calculating the difference in the plasmon energy between T_{ref} and $T = 450$ ˚C at each pixel ($\Delta T = 400$ ˚C), and the plasmon energy difference is converted to temperature using linear regression from **Figure 3.1a**, inset.

Core-loss thermometry imaging was similarly performed for each pixel but instead analyzed using the Si $L_{2,3}$ edge differential intensity as in **Figure 3.2a** and linear regression from **Figure 3.3**. Each spectrum in the image is smoothed using a Savitsky-Golay third-order smoothing function over 51-spectral pixels (**Figure 3.4c**). The core-loss thermometry image's average temperature with spectral smoothing considered is 411 ± 106 ˚C (26% error). This relatively high standard deviation is a result of the poor signal-to-noise ratio at

each pixel. Therefore, by applying a standard denoising function, trained by 10% of the STEM-EELS core-loss spectra, we further optimize the differential signal while minimizing the background noise (**Figure 3.4d**). The denoised core-loss spectral image obtains a measured temperature of 403 ± 44 ˚C (11% error). This 58% reduction in absolute uncertainty from the non-denoised core-loss thermal image can be further optimized for samples of uniform thickness or more robust denoising algorithms.

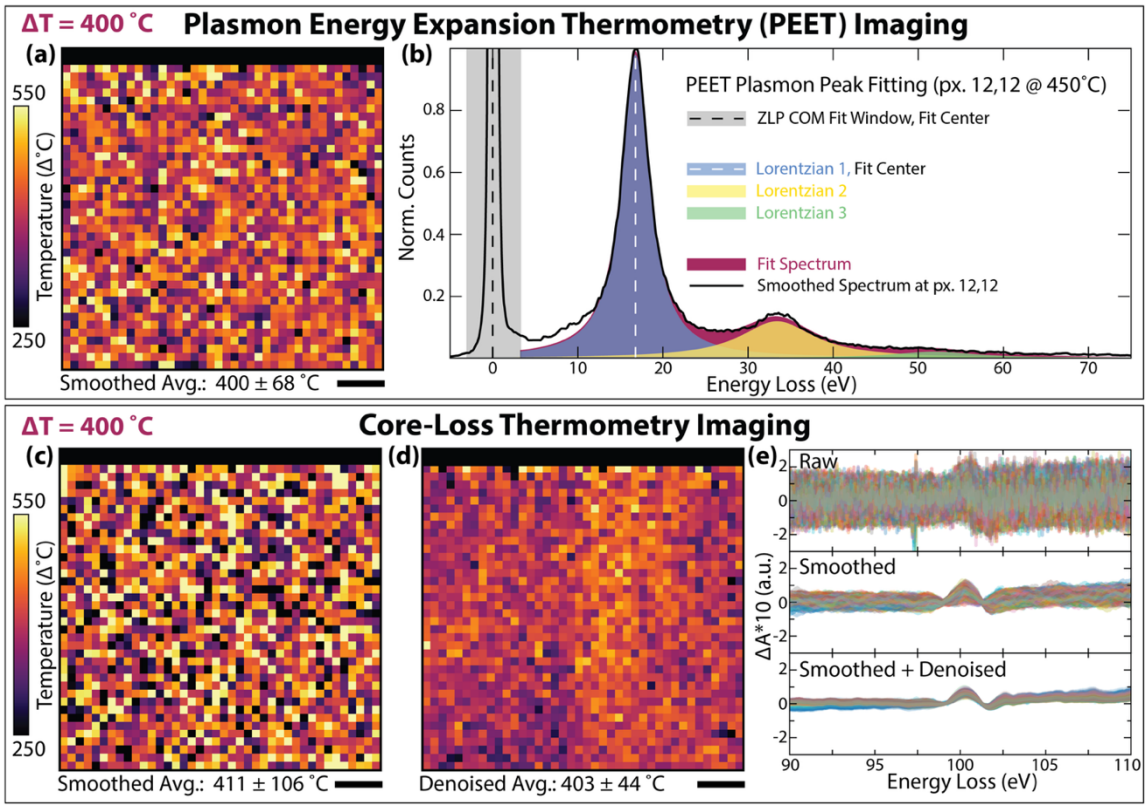

Figure 3.4. Comparing the accuracy of plasmon energy expansion and core-loss thermometry imaging. (a) A plasmon energy expansion thermometry (PEET) image of the Si lamella for ΔT = 400 ˚C. (b) Each pixel's spectrum was smoothed and aligned using a center-of-mass (COM) fit of the zero-loss peak (ZLP). The Si plasmon energy was calculated in the 450 ˚C and T_{ref} images, and each pixel's plasmon energy difference between 450 ˚C and T_{ref} was converted to a measured temperature using linear regression from **Figure 3.1a**(inset). (c) A core-loss thermometry image of the Si lamella for ΔT = 400 ˚C. Each pixel's core-loss spectrum was again aligned using the ZLP COM, and a differential

spectrum was calculated and smoothed for each pixel. The amplitude of the differential peak resulting from bandgap reduction was converted to temperature using linear regression from **Figure 3.3**. (d) A core-loss thermometry image denoised using a 3-layer bottleneck autoencoder from scikit-learn's MLPRegressor. (e) The denoiser uses self-supervised learning by leveraging the smoothed spectral output trained on 10% of the data. All scale bars below the STEM-EELS images are 250 nm.

Table 3.1. Thermal lattice expansion calculation methods in this work. All measurements were performed on crystalline Si with native oxide. The reported temperature-dependent thermal expansion coefficient (TEC) of Si was used for all inputs [ref. 27], and its fit error represents the nonlinearity in this temperature range of 50 – 450 ˚C.

Measurement	**Method**	**Required Inputs**	**TEC [10^{-6} K^{-1}]**	**Fit Error×100 (and R^2)**
Reported TEC [ref. 27]	–	–	4.09	0.37 (0.996)
Plasmon thermometry	Low-loss EELS	Free electron model (ϵ_∞, m_{eff})	5.06	0.32 (0.998)
Plasmon thermometry	TDDFT	Free electron model (ϵ_∞, m_{eff}), TEC	3.51	0.41 (0.994)
Core-loss thermometry	Core-loss EELS	Varshni equation[a], TEC	3.89	0.52 (0.993)
Core-loss thermometry	DFT/BSE	Varshni equation[a], TEC	3.98	0.59 (0.989)

[a] The Varshni equation's constants can be taken from literature or derived using the core-loss spectral shift

3.3 Discussion

Figure 3.5 and **Table 3.1** compare the thermal expansion coefficients derived using PEET and core-loss thermometry to literature-reported values of crystalline Si. In PEET, the plasmon energy shift is converted to lattice expansion using the free-electron model (**Equation 3.1**) as: $a(T) / a(T_{ref}) = (E_p(T) / E_p(T_{ref}))^{2/3}$, where a is the lattice parameter. This approach assumes isotropic expansion. To derive the lattice parameter change from core-loss thermometry, we convert the as-measured Si $L_{2,3}$ and bandgap redshift with temperature by using the reported Varshni equation for Si.[24]

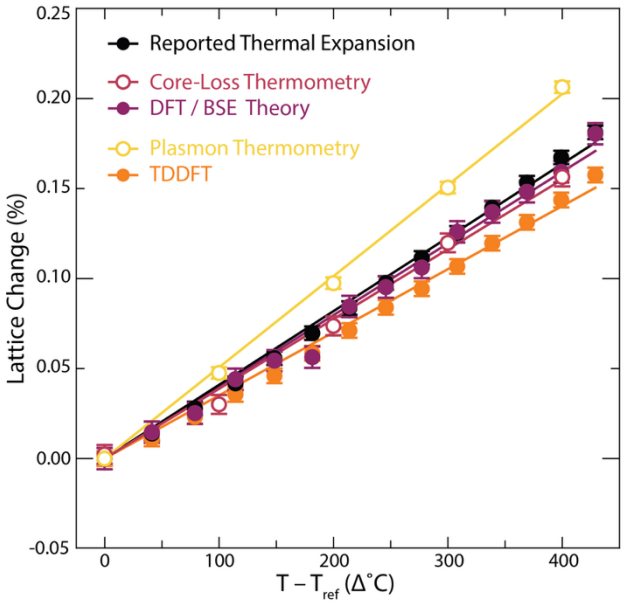

Figure 3.5. Thermal lattice expansion quantified using low- and core-loss EELS. Four methods are compared against the reported thermal expansion of crystalline Si [ref. 27]. Core-loss thermometry (magenta) quantifies lattice expansion via shifts in the Si $L_{2,3}$ edge arising from the temperature-dependent band gap, while plasmon thermometry (yellow) tracks the plasmon energy shift according to the free-electron model. DFT/BSE (core-loss) and TDDFT (plasmon) simulations were performed by isotropically expanding the Si unit cell; DFT/BSE spectra were corrected for the intrinsic bandgap. The slope of each fit corresponds to the thermal expansion coefficient (see Table 3.1), with y-intercepts fixed at 0%. Error bars are determined from reduced χ^2 analysis of the linear fits.

PEET overestimates the thermal expansion coefficient by 1.03×10^{-6} K^{-1}, approximately 25% higher than the literature-reported value. This discrepancy may arise from temperature-dependence of the dielectric constant, valence band effective mass, sub-pixel specimen drift, or lamella strain. While the effective mass is known to increase by ~5-10% over this temperature range, a substantial shift in the dielectric constant would also be required to fully explain the observed error.[30,31] In contrast, core-loss thermometry provides a more accurate measure of the thermal expansion coefficient at 3.89×10^{-6} K^{-1}, with reduced uncertainty in the image-averaged dataset even without spectral denoising. TDDFT and DFT/BSE simulations, based on isotropic lattice expansion, show relatively good agreement with both respective thermometry methods.

One primary drawback of core-loss thermometry is that its temperature-dependence arises from more complex physical phenomena than the direct lattice expansion captured by PEET. For example, the thermal core-loss change would likely be more subtle for metals without a band gap. PEET is best suited for measuring thermal expansion of pure, uniform metals with a single, well-defined plasmon peak. As such, the two methods are highly complementary. This study introduces core-loss thermometry as a new approach for semiconductors and still requires validation for other materials with complex temperature-dependent changes in the electronic structure.

Other practical factors of this experiment must be considered. While the intrinsic defects or native SiO_2 layer could potentially introduce local variations in the thermal expansion, their concentrations were negligible (4.4×10^{11} / 5×10^{22}; 4 nm / 90 nm = 4% SiO_2 concentration).[26,32] Potential phase transitions and contamination were avoided by specimen annealing, and the immeasurable oxygen K-edge further confirms the insignificant SiO_2 concentration. Future studies could quantify temperature-dependent strain, tilt, and momentum effects on the accuracy of PEET and core-loss thermometry.[33] To investigate any microscope- and sample-induced STEM-EELS artifacts, we tested correlations between the dark-field, PEET, plasmon energy, core-loss thermometry, and thickness images across the 40×40 pixel scan area. The results show a strong statistically significant correlation between

thickness and plasmon energy (0.733, p-value = ~0; apparent in **Figure 3.1c**) and a weak yet significant correlation between the denoised core-loss temperature map and thickness (0.226, p-value = ~0; apparent in **Figure 3.4d**). See Supplementary Information for all correlations. PEET datasets show no correlations. Balancing the beam current, length scale, and pixel view time will be important to approach sub-nm spatial resolutions without inducing beam damage and heating (see Supplementary Information). High-stability MEMS *in situ* heating holders will allow enhanced stability needed for atomic-scale STEM-EELS thermometry.

To improve pixel-level precision in core-loss thermometry, we implemented an open-source, self-supervised autoencoder to denoise the differential core-loss spectra. Denoising is an emerging approach to electron microscopy, enabling faster acquisition times of features even beyond existing resolution limits.[34–37] Our autoencoder was trained on 10% of the data to reconstruct spectra by distinguishing intrinsic signals from noise. This approach reduced uncorrelated pixel-level noise by 58% while preserving the shape and position of spectral features, far more accurate than smoothing alone. However, the specimen's thickness variability posed challenges for model training. Models trained on mismatched thicknesses introduced noticeable artifacts due to differences in the plasmons' multiple scattering background. This artifact is apparent in the denoised core-loss thermometry image in **Figure 3.4d**, where thicker regions appear as brighter contrast (hotter temperatures) due to the rising background. Therefore, optimal denoising occurs when the training set's background matches that of the test set. Additionally, smoothing spectra prior to denoising improved model performance by supressing the high-requency noise poorly modeled by this network. Despite these considerations, our denoising strategy is a promising step toward reliable, high-resolution core-loss thermometry. Continued optimization of data acquisition and denoising model robustness will be essential for advancing core-loss thermometry's accuracy.

Through a combination of *in situ* STEM-EELS and first-principles simulations, we demonstrate core-loss thermometry for imaging element-specific lattice temperatures in semiconductors with nanometer-scale precision. By directly probing temperature-dependent changes in electronic structure, core-loss thermometry is used to capture the redshift of the

Si $L_{2,3}$ edge – an effect that tracks the bandgap's redshift as driven by thermal lattice expansion and electron-phonon renormalization. As a result, this technique not only enables temperature mapping but also extracts Varshni equation constants with sub-nanometer precision. Despite the inherent complexity of core-loss EELS, our findings show that core-loss thermometry yields an interpretable signal that does not rely on *ab initio* calculations, making the approach broadly accessible to the X-ray spectroscopy and electron microscopy communities. Compared to PEET, core-loss thermometry offers improved accuracy for semiconductors with low thermal expansion coefficients or non-uniform composition and strain. With continued development in spectral alignment, denoising, and acquisition, core-loss thermometry will map temperatures at sub-nanometer spatial resolutions during operando or ultrafast experiments. We envision future investigations of thermal strain and heat transfer in multi-element junctions and at nanoscale interfaces relevant to microelectronics, photonics, and photocatalysts.

3.4 Methods

Temperature-dependent STEM-EELS

All TEM measurements were performed on a JEOL NeoARM microscope with a cold field-emission gun (zero-loss peak FWHM = 0.6 eV). STEM-EELS data was acquired at 200 kV in 40kx STEM magnification mode using a 3 cm camera length. The sample was measured at ~0˚ tilt, approximately on the [100] zone axis. The tilt angle was not controlled during the thermal sweep. The beam current was approximately 100 pA or 55,800 pA/μm^2 in STEM. The Gatan Continuum Imaging Filter was aligned using a 2.5 mm entrance aperture with 30 meV/ch dispersion and a K3 detector. The Gatan sub-scan feature (32×32/pixel) was enabled to diffuse the beam over the scanning region on the sample and minimize beam-induced heating. The acquisition time was fixed at a 0.25 s view time in dualEELS (1% live time low-loss with 0 eV shift, 100% live time high-loss with 20 eV shift). Specimen drift was corrected every 40 pixels and managed using Gatan drift-correction software over three image-averaged passes. The specimen drift was 10 – 20 % of the 42.33 nm pixel size between each drift correction step.

The Si lamella was prepared from a 200 nm Ta-capped, 100-oriented intrinsic Si wafer substrate (>10 kΩ · cm), University Wafer. The autoTEM lift-out feature on a ThermoFisher Helios Ga FIB was utilized to lift-out the specimen with a W capping layer deposited on the sample via ion-beam induced deposition (IBID) at 30 kV prior to lift-out. The lamella was mounted on a Cu lift-out grid. It was thinned into the staircase shape using 30 kV ions. Accelerating voltages of 5 kV and 2 kV were subsequently used for final thinning and polishing. A Gatan 652-TA model heating holder was used for all temperature-dependent STEM-EELS measurements. The specimen was first loaded into a vacuum pumping station and heated to 450 ˚C for 30 min to anneal and minimize surface carbon contamination, and it was again heated to 450 ˚C for 30 min inside the microscope column to minimize transfer-induced contamination. During STEM-EELS measurements, the holder temperature was first set to 450 ˚C and the temperature was ramped down in 100 ˚C steps to 50 ˚C and then ramped up to check for heating hysteresis. Between each temperature set point, 5 min was allotted for thermal equilibration. Gatan reports a ±5 ˚C accuracy for the heating controller.

All STEM-EELS data was analyzed using the HyperSpy python loader.[38] A 19 pixel-wide median filter was applied to all data to remove hot pixels. Center-of-mass fitting was used for ZLP peak fitting, and three Lorentzian functions were used to fit the three Si plasmons. Additional fitting and spectral denoising parameters are detailed in the Supplementary Information. All analysis scripts can be provided upon request.

Ab Initio Theory

Density Functional Theory (DFT) Parameters. A 200 Ry cutoff energy was used for all DFT calculations based on convergence tests with a 10.33 Bohr lattice parameter (see test results in Supplementary Information). All DFT self-consistent field calculations utilize a 1×10^{-10} Ry convergence threshold, 16×16×16 *k*-point mesh, 6 electronic states (bands), and standard atomic positions for crystalline Si in the diamond cubic crystal structure (fcc lattice with a two-atom basis). The silicon pseudopotential file for all calculations was produced using the ONCVPSP code.[39] This norm-conserving pseudo was calculated using a PBE functional and nonlinear core correction.

Low-Loss EELS Theory. turboEELS was used to simulate the Si volume plasmon, a program integrated within the Quantum ESPRESSO package.[40,41] turboEELS calculates the low-loss volume plasmon spectra using a Liouville–Lanczos approach to linearized time-dependent DFT (TDDFT). By calculating the charge-density susceptibility with the quantum Liouville equation, the inverse of the imaginary/longitudinal component of the dielectric function (the EEL spectrum) is simulated. EEL spectra were calculated using DFT and BSE theory.

Core-Loss EELS Theory. To simulate the Si $L_{2,3}$ edge core-loss spectrum, we leverage the Obtaining Core Excitations from the *Ab initio* electronic structure and the NIST BSE solver (OCEAN) package.[42] The OCEAN workflow uses Quantum ESPRESSO to perform DFT calculations of silicon's electronic structure and subsequently calculates the core-hole exciton effects and core-level spectrum through BSE calculations. OCEAN 3.0.1 and Quantum ESPRESSO 7.0 were used for all calculations. Due to DFT's well-known inaccuracy in calculating the band gap of materials, a scissor shift corresponding to the temperature-dependent band gap is incorporated for each lattice parameter simulated. The BSE and non-self-consistent field and screening calculations simulate 100 electronic states (bands). The relative permittivity is fixed to $\varepsilon = 11.4$.[43]

3.5 Supporting Information

The supporting information, containing figures and data labelled S[X], is available free of charge at: https://doi.org/10.22002/wheak-c7d39

3.6 References

(1) Shafique, M.; Garg, S.; Henkel, J.; Marculescu, D. The EDA Challenges in the Dark Silicon Era: Temperature, Reliability, and Variability Perspectives. In *Proceedings of the 51st Annual Design Automation Conference*; DAC '14; Association for Computing Machinery: New York, NY, USA, 2014; pp 1–6. https://doi.org/10.1145/2593069.2593229.

(2) Ibrahim, A.; Salem, M.; Kamarol, M.; Delgado, M. T.; Desa, M. K. M. Review of Active Thermal Control for Power Electronics: Potentials, Limitations, and Future Trends. *IEEE Open J. Power Electron.* **2024**, *5*, 414–435. https://doi.org/10.1109/OJPEL.2024.3376086.

(3) Zhou, P.; Navid, I. A.; Ma, Y.; Xiao, Y.; Wang, P.; Ye, Z.; Zhou, B.; Sun, K.; Mi, Z. Solar-to-Hydrogen Efficiency of More than 9% in Photocatalytic Water Splitting. *Nature* **2023**, *613* (7942), 66–70. https://doi.org/10.1038/s41586-022-05399-1.

(4) Kim, H.; Seo, J. W.; Chung, W.; Narejo, G. M.; Koo, S. W.; Han, J. S.; Yang, J.; Kim, J.-Y.; In, S.-I. Thermal Effect on Photoelectrochemical Water Splitting Toward Highly Solar to Hydrogen Efficiency. *ChemSusChem* **2023**, *16* (11), e202202017. https://doi.org/10.1002/cssc.202202017.

(5) Mecklenburg, M.; Hubbard, W. A.; White, E. R.; Dhall, R.; Cronin, S. B.; Aloni, S.; Regan, B. C. Nanoscale Temperature Mapping in Operating Microelectronic Devices. *Science* **2015**, *347* (6222), 629–632. https://doi.org/10.1126/science.aaa2433.

(6) Mecklenburg, M.; Zutter, B.; Regan, B. C. Thermometry of Silicon Nanoparticles. *Phys. Rev. Appl.* **2018**, *9* (1), 014005. https://doi.org/10.1103/PhysRevApplied.9.014005.

(7) Hu, X.; Yasaei, P.; Jokisaari, J.; Öğüt, S.; Salehi-Khojin, A.; Klie, R. F. Mapping Thermal Expansion Coefficients in Freestanding 2D Materials at the Nanometer Scale. *Phys. Rev. Lett.* **2018**, *120* (5), 055902. https://doi.org/10.1103/PhysRevLett.120.055902.

(8) Abe, H.; Terauchi, M.; Kuzuo, R.; Tanaka, M. Temperature Dependence of the Volume-Plasmon Energy in Aluminum. *J. Electron Microsc.* **1992**, *41* (6), 465–468. https://doi.org/10.1093/oxfordjournals.jmicro.a050994.

(9) Hubbard, W. A.; Mecklenburg, M.; Lodico, J. J.; Chen, Y.; Ling, X. Y.; Patil, R.; Kessel, W. A.; Flatt, G. J. K.; Chan, H. L.; Vareskic, B.; Bal, G.; Zutter, B.; Regan, B. C. Electron-Transparent Thermoelectric Coolers Demonstrated with Nanoparticle and Condensation Thermometry. *ACS Nano* **2020**, *14* (9), 11510–11517. https://doi.org/10.1021/acsnano.0c03958.

(10) Shen, L.; Mecklenburg, M.; Dhall, R.; Regan, B. C.; Cronin, S. B. Measuring Nanoscale Thermal Gradients in Suspended MoS_2 with STEM-EELS. *Appl. Phys. Lett.* **2019**, *115* (153108), 1–5. https://doi.org/10.1063/1.5094443.

(11) Chmielewski, A.; Ricolleau, C.; Alloyeau, D.; Wang, G.; Nelayah, J. Nanoscale Temperature Measurement during Temperature Controlled in Situ TEM Using Al Plasmon Nanothermometry. *Ultramicroscopy* **2020**, *209*, 112881. https://doi.org/10.1016/j.ultramic.2019.112881.

(12) Castioni, F.; Auad, Y.; Blazit, J.-D.; Li, X.; Woo, S. Y.; Watanabe, K.; Taniguchi, T.; Ho, C.-H.; Stéphan, O.; Kociak, M.; Tizei, L. H. G. Nanosecond Nanothermometry in

an Electron Microscope. *Nano Lett.* **2025**, *25* (4), 1601–1608. https://doi.org/10.1021/acs.nanolett.4c05692.

(13) Yang, Y.-C.; Serafini, L.; Gauquelin, N.; Verbeeck, J.; Jinschek, J. R. Improving the Accuracy of Temperature Measurement on TEM Samples Using Plasmon Energy Expansion Thermometry (PEET): Addressing Sample Thickness Effects. *Ultramicroscopy* **2025**, *270*, 114102. https://doi.org/10.1016/j.ultramic.2025.114102.

(14) Manzke, R. Wavevector Dependence of the Volume Plasmon of GaAs and InSb. *J. Phys. C: Solid State Phys.* **1980**, *13* (5), 911. https://doi.org/10.1088/0022-3719/13/5/021.

(15) *momentum transfer resolved electron energy-loss spectroscopy, q-EELS | Glossary | JEOL Ltd.* momentum transfer resolved electron energy-loss spectroscopy, q-EELS | Glossary | JEOL Ltd. https://www.jeol.com/ (accessed 2024-11-01).

(16) Roth, F.; König, A.; Fink, J.; Büchner, B.; Knupfer, M. Electron Energy-Loss Spectroscopy: A Versatile Tool for the Investigations of Plasmonic Excitations. *J. Electron Spectrosc. Relat. Phenom.* **2014**, *195*, 85–95. https://doi.org/10.1016/j.elspec.2014.05.007.

(17) Liao, K.; Shibata, K.; Mizoguchi, T. Nanoscale Investigation of Local Thermal Expansion at $SrTiO_3$ Grain Boundaries by Electron Energy Loss Spectroscopy. *Nano Lett.* **2021**, *21* (24), 10416–10422. https://doi.org/10.1021/acs.nanolett.1c03735.

(18) Park, W.-W.; Olshin, P. K.; Kim, Y.-J.; Nho, H.-W.; Mamonova, D. V.; Kolesnikov, I. E.; Medvedev, V. A.; Kwon, O.-H. Nanoscale Cathodoluminescence Thermometry with a Lanthanide-Doped Heavy-Metal Oxide in Transmission Electron Microscopy. *ACS Nano* **2024**, *18* (6), 4911–4921. https://doi.org/10.1021/acsnano.3c10020.

(19) Espinosa, A.; Castro, G. R.; Reguera, J.; Castellano, C.; Castillo, J.; Camarero, J.; Wilhelm, C.; García, M. A.; Muñoz-Noval, Á. Photoactivated Nanoscale Temperature Gradient Detection Using X-Ray Absorption Spectroscopy as a Direct Nanothermometry Method. *Nano Lett.* **2021**, *21* (1), 769–777. https://doi.org/10.1021/acs.nanolett.0c04477.

(20) Rosen, D. J.; Yang, S.; Marino, E.; Jiang, Z.; Murray, C. B. In Situ EXAFS-Based Nanothermometry of Heterodimer Nanocrystals under Induction Heating. *J. Phys. Chem. C* **2022**, *126* (7), 3623–3634. https://doi.org/10.1021/acs.jpcc.2c00608.

(21) Palmer, L. D.; Lee, W.; Dong, C.-L.; Liu, R.-S.; Wu, N.; Cushing, S. K. Determining Quasi-Equilibrium Electron and Hole Distributions of Plasmonic Photocatalysts Using Photomodulated X-Ray Absorption Spectroscopy. *ACS Nano* **2024**, *18* (13), 9344–9353. https://doi.org/10.1021/acsnano.3c08181.

(22) Rossi, T. C.; Dykstra, C. P.; Haddock, T. N.; Wallick, R.; Burke, J. H.; Gentle, C. M.; Doumy, G.; March, A. M.; van der Veen, R. M. Charge Carrier Screening in Photoexcited Epitaxial Semiconductor Nanorods Revealed by Transient X-Ray Absorption Linear Dichroism. *Nano Lett.* **2021**, *21* (22), 9534–9542. https://doi.org/10.1021/acs.nanolett.1c02865.

(23) Nemausat, R.; Gervais, C.; Brouder, C.; Trcera, N.; Bordage, A.; Coelho-Diogo, C.; Florian, P.; Rakhmatullin, A.; Errea, I.; Paulatto, L.; Lazzeri, M.; Cabaret, D. Temperature Dependence of X-Ray Absorption and Nuclear Magnetic Resonance Spectra: Probing Quantum Vibrations of Light Elements in Oxides. *Phys. Chem. Chem. Phys.* **2017**, *19* (8), 6246–6256. https://doi.org/10.1039/C6CP08393E.

(24) Zhang, Y.; Wang, Z.; Xi, J.; Yang, J. Temperature-Dependent Band Gaps in Several Semiconductors: From the Role of Electron–Phonon Renormalization. *J. Phys.: Condens. Matter* **2020**, *32* (47), 475503. https://doi.org/10.1088/1361-648X/aba45d.

(25) Ponce, S.; Gillet, Y.; Laflamme Janssen, J.; Marini, A.; Verstraete, M.; Gonze, X. Temperature Dependence of the Electronic Structure of Semiconductors and Insulators. *J. Chem. Phys.* **2015**, *143* (102813). https://doi.org/10.1063/1.4927081.

(26) Oh-ishi, K.; Ohsuna, T. Inelastic Mean Free Path Measurement by STEM-EELS Technique Using Needle-Shaped Specimen. *Ultramicroscopy* **2020**, *212*, 112955. https://doi.org/10.1016/j.ultramic.2020.112955.

(27) Watanabe, H.; Yamada, N.; Okaji, M. Linear Thermal Expansion Coefficient of Silicon from 293 to 1000 K. *Int. J. Thermophys.* **2004**, *25* (1), 221–236. https://doi.org/10.1023/B:IJOT.0000022336.83719.43.

(28) Perdew, J. P. Density Functional Theory and the Band Gap Problem. *Int. J. Quantum Chem.* **1985**, *28* (S19), 497–523. https://doi.org/10.1002/qua.560280846.

(29) Zoric, M. R.; Basera, P.; Palmer, L. D.; Aitbekova, A.; Powers-Riggs, N.; Lim, H.; Hu, W.; Garcia-Esparza, A. T.; Sarker, H.; Abild-Pedersen, F.; Atwater, H. A.; Cushing, S. K.; Bajdich, M.; Cordones, A. A. Oxidizing Role of Cu Cocatalysts in Unassisted Photocatalytic CO_2 Reduction Using p-GaN/Al_2O_3/Au/Cu Heterostructures. *ACS Nano* **2024**, *18* (30), 19538–19548. https://doi.org/10.1021/acsnano.4c02088.

(30) Lautenschlager, P.; Garriga, M.; Vina, L.; Cardona, M. Temperature Dependence of the Dielectric Function and Interband Critical Points in Silicon. *Phys. Rev. B* **1987**, *36* (9), 4821–4830. https://doi.org/10.1103/PhysRevB.36.4821.

(31) Green, M. Intrinsic Concentration, Effective Densities of States, and Effective Mass in Silicon. *J. Appl. Phys.* **1990**, *67*, 2944–2954.

(32) Bohling, C.; Sigmund, W. Self-Limitation of Native Oxides Explained. *Silicon* **2016**, *8* (3), 339–343. https://doi.org/10.1007/s12633-015-9366-8.

(33) Palmer, L. D.; Lee, W.; Gage, T. E.; Cushing, S. K. Mapping Nanoscale Anisotropic Thermal Expansion and Strain through Correlative Diffraction, Imaging, and Spectroscopy in the TEM. *Microsc. Microanal.* **2024**, *30* (Supplement_1), ozae044.682. https://doi.org/10.1093/mam/ozae044.682.

(34) Wang, Y.; Tan, M.; Fernandez-Granda, C.; Crozier, P. A. Revealing Information from Weak Signal in Electron Energy-Loss Spectroscopy with a Deep Denoiser. Ver. 1, *arXiv*, May 20, 2025. https://doi.org/10.48550/arXiv.2505.14032.

(35) Pate, C. M.; Hart, J. L.; Taheri, M. L. RapidEELS: Machine Learning for Denoising and Classification in Rapid Acquisition Electron Energy Loss Spectroscopy. *Sci. Rep.* **2021**, *11* (1), 19515. https://doi.org/10.1038/s41598-021-97668-8.

(36) Kim, J.; Rhee, J.; Kang, S.; Jung, M.; Kim, J.; Jeon, M.; Park, J.; Ham, J.; Kim, B. H.; Lee, W. C.; Roh, S.-H.; Park, J. Self-Supervised Machine Learning Framework for High-Throughput Electron Microscopy. *Sci. Adv.* **2025**, *11* (14), eads5552. https://doi.org/10.1126/sciadv.ads5552.

(37) Kim, B. H.; Heo, J.; Kim, S.; Reboul, C. F.; Chun, H.; Kang, D.; Bae, H.; Hyun, H.; Lim, J.; Lee, H.; Han, B.; Hyeon, T.; Alivisatos, A. P.; Ercius, P.; Elmlund, H.; Park, J. Critical Differences in 3D Atomic Structure of Individual Ligand-Protected Nanocrystals in Solution. *Science* **2020**, *368* (6486), 60–67. https://doi.org/10.1126/science.aax3233.

(38) Peña, F. de la; Prestat, E.; Fauske, V. T.; Lähnemann, J.; Burdet, P.; Jokubauskas, P.; Furnival, T.; Francis, C.; Nord, M.; Ostasevicius, T.; MacArthur, K. E.; Johnstone, D. N.; Sarahan, M.; Taillon, J.; Aarholt, T.; pquinn-dls; Migunov, V.; Eljarrat, A.; Caron, J.; Nemoto, T.; Poon, T.; Mazzucco, S.; actions-user; Tappy, N.; Cautaerts, N.; Somnath, S.; Slater, T.; Walls, M.; pietsjoh; Ramsden, H. Hyperspy/Hyperspy: V2.1.1, 2024. https://doi.org/10.5281/zenodo.12724131.

(39) Hamann, D. R. Optimized Norm-Conserving Vanderbilt Pseudopotentials. *Phys. Rev. B* **2013**, *88* (8), 085117. https://doi.org/10.1103/PhysRevB.88.085117.

(40) Timrov, I.; Vast, N.; Gebauer, R.; Baroni, S. turboEELS—A Code for the Simulation of the Electron Energy Loss and Inelastic X-Ray Scattering Spectra Using the Liouville–Lanczos Approach to Time-Dependent Density-Functional Perturbation Theory. *Comput. Phys. Commun.* **2015**, *196*, 460–469. https://doi.org/10.1016/j.cpc.2015.05.021.

(41) Giannozzi, P.; Baroni, S.; Bonini, N.; Calandra, M.; Car, R.; Cavazzoni, C.; Ceresoli, D.; Chiarotti, G. L.; Cococcioni, M.; Dabo, I.; Corso, A. D.; Gironcoli, S. de; Fabris, S.; Fratesi, G.; Gebauer, R.; Gerstmann, U.; Gougoussis, C.; Kokalj, A.; Lazzeri, M.; Martin-Samos, L.; Marzari, N.; Mauri, F.; Mazzarello, R.; Paolini, S.; Pasquarello, A.; Paulatto, L.; Sbraccia, C.; Scandolo, S.; Sclauzero, G.; Seitsonen, A. P.; Smogunov, A.; Umari, P.; Wentzcovitch, R. M. QUANTUM ESPRESSO: A Modular and Open-Source Software Project for Quantum Simulations of Materials. *J. Phys.: Condens. Matter* **2009**, *21* (39), 395502. https://doi.org/10.1088/0953-8984/21/39/395502.

(42) Vinson, J. Advances in the OCEAN-3 Spectroscopy Package. *Phys. Chem. Chem. Phys.* **2022**, *24* (21), 12787–12803. https://doi.org/10.1039/D2CP01030E.

(43) Baroni, S.; Resta, R. Ab Initio Calculation of the Macroscopic Dielectric Constant in Silicon. *Phys. Rev. B* **1986**, *33* (10), 7017–7021. https://doi.org/10.1103/PhysRevB.33.7017.

C H A P T E R 4

IMAGING NANOSCALE PHOTOCARRIER TRAPS IN SOLAR WATER-SPLITTING CATALYSTS

Adapted with permission from the following:

Palmer, L. D.; Lee, W.; Prasad, P. R.; Layne, B. W.; Wu, H.-H.; Chen, Z.; Wen, J.; Liu, Y.; Pan, X.; Talin, A. A.; Kudo, A.; Ardo, S.; Patterson, J. P.; Gage, T. E.; Cushing, S. K. Imaging nanoscale photocarrier traps in solar water splitting catalysts. Ver. 1. *arXiv*, Dec 31, 2025. https://doi.org/10.48550/arXiv.2512.24543.

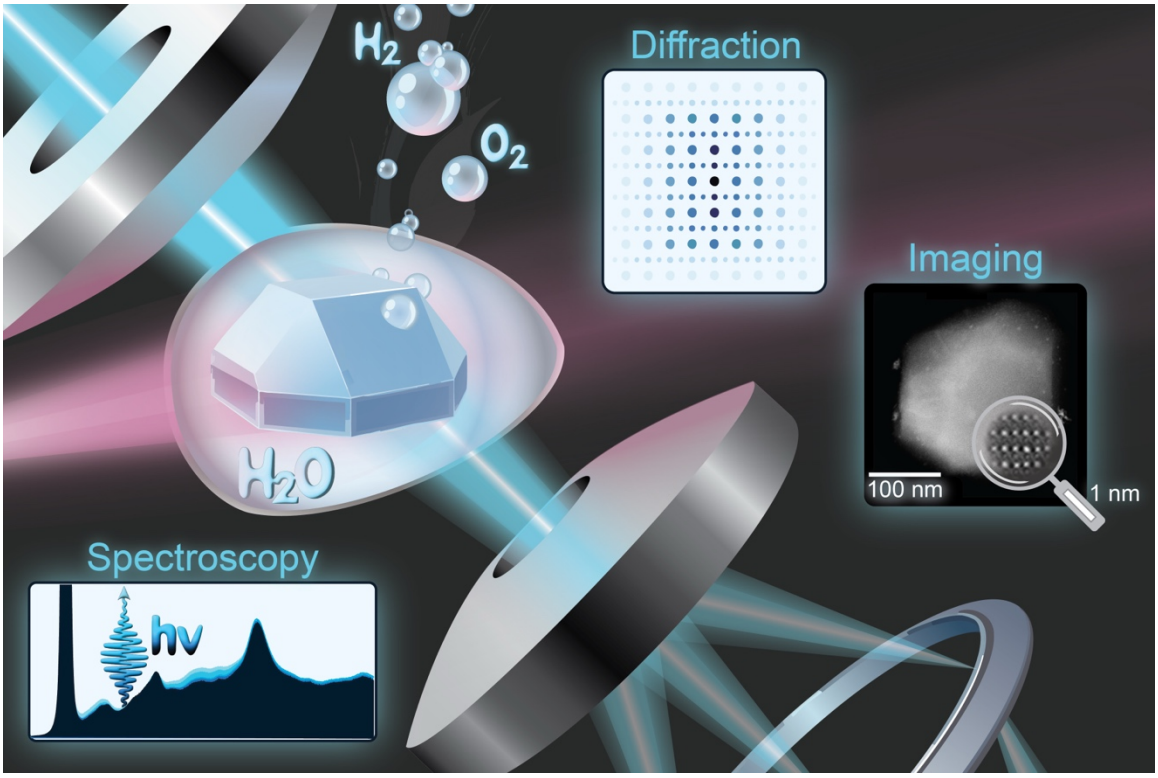

4.1 Introduction

Efficient solar water splitting requires long photocarrier lifetimes to ensure that carriers can sufficiently transport to catalytic sites.[1] Nanoparticle photocatalysts are often engineered to suppress carrier recombination and to spatially separate electron–hole pairs. Common strategies to increase photocarrier lifetimes are cocatalysts that separate charge carriers, doping strategies that suppress trap sites, and flux treatments that increase crystallinity, enabling nearly 100% internal quantum efficiency for one select catalyst composition.[2,3] However, most photocatalysts remain plagued by photocarrier traps and recombination sites.[4,5]

Although these trap and recombination sites drive carrier recombination and impede carrier transport, they have not been directly imaged under steady-state illumination conditions relevant to solar water splitting. Steady-state illumination results in photothermal and photocarrier effects that must be separately resolved. Stroboscopic scattering microscopy accurately images photocarriers and temperature down to the micrometer-scale optical diffraction limit.[6] Ultrafast scanning probe microscopy images photocarrier dynamics with 1–100 nm resolution, but its contrast mechanism provides only indirect information about bulk carrier dynamics and is insensitive to heat.[7,8] Electron energy-loss spectroscopy (EELS) thermometry in the scanning transmission electron microscope (STEM) directly images angstrom-scale temperatures from femtoseconds to seconds.[9–12] STEM-EELS has yet to resolve excited-state photocarriers on the same length scale.

We develop photomodulated STEM-EELS in an optically coupled STEM to directly image steady-state photocarriers in 1 wt% rhodium-doped strontium titanate ($SrTiO_3$:Rh) nanoparticles with angstrom-scale resolution. We first use core-loss STEM-EELS and atomic-resolution STEM imaging to identify carrier trap sites, including surface oxygen vacancies and copper cocatalysts. We then image photoexcited carriers in these traps with photomodulated STEM-EELS of low-loss bulk plasmons. The loss function measured by EELS is traditionally elusive, especially for metal oxide semiconductors that do not follow the free electron model, resulting in overlapping bulk plasmon and interband transition peaks.

We perform time-dependent density functional theory (TDDFT) calculations to determine which valence band electrons contribute to each peak of the loss function. As a result, we distinguish how heat and photocarriers separately influence select plasmon modes, supported by experimental heating control experiments. We image trapped photocarriers at the $SrTiO_3$:Rh nanoparticle's surface at a concentration roughly 70% higher than the nanoparticle's bulk. Overall, we use photomodulated STEM-EELS imaging to visualize nanoscale carrier trapping in nanoparticle photocatalysts—directly imaging carrier trapping phenomena previously inferred by ensemble-averaged measurements. We demonstrate how photomodulated STEM-EELS imaging can be used to resolve carriers and heat in nanostructured photocatalysts, optoelectronics, and quantum photonics.

4.2 Platform for Imaging Photocarrier Trap States

We perform photomodulated STEM-EELS in an optically coupled STEM equipped with a continuous-wave laser (**Fig. 4.1A**). The 3.1 eV laser induces photocarriers by photoexciting $SrTiO_3$:Rh nanoparticles above their 2.8 eV absorption onset.[13] A resistive heater is used for temperature-dependent control measurements. Simultaneous EEL spectral acquisition is performed with angstrom-scale precision. EELS acquisition is achieved using a prism and a direct electron detector. This combined platform enables photomodulated STEM-EELS imaging, thereby resolving photocarrier trapping at angstrom-to-micrometer structural features that govern solar water splitting efficiencies (**Fig. 4.1B**). Photographs of the experimental setup are shown in Fig. S1.

Prior studies report that $SrTiO_3$:Rh nanoparticles' photocarriers are (1) spatially separated by cocatalysts, (2) trapped at oxygen vacancy sites, and (3) localized to rhodium dopants (**Fig. 4.1B).**[3,13–15] $SrTiO_3$ must be doped to enable visible light absorption. However, these dopants often create defect states that restrict photocarrier mobilities and lifetimes. For example, rhodium dopants introduce occupied and unoccupied Rh *4d* states above the O *2p* valence band maximum of undoped $SrTiO_3$ (**Fig. 4.1C**). Visible light photoexcitation of $SrTiO_3$:Rh promotes electrons from Rh *4d* states in the valence band (VB) to Ti *3d* states in the

conduction band (CB). These rhodium-localized midgap states, as well as oxygen vacancies, create recombination and trap sites, posing an engineering challenge.

Photomodulated STEM-EELS resolves excited-state photocarrier localization both spatially (**Fig. 4.1B**) and energetically (**Fig. 4.1C**). For photomodulated STEM-EELS, both low-loss and core-loss spectra are measurable, each with distinct advantages. While element-specific core-level excitations are proven to distinguish carrier and heat signatures,[16–18] bulk plasmons in low-loss EELS yield orders of magnitude more signal and directly measure free carrier density. However, unlike core-loss spectroscopy, photothermal and photoexcited carrier effects have not been separated for low-loss EELS. We therefore employ TDDFT calculations to project select low-loss bulk plasmon modes onto the $SrTiO_3$ band structure. This spectrally resolved approach allows us to interpret the origin of the electronic structure of each plasmon mode and elucidate how each mode is influenced by either photothermal heating or photoexcited carriers.

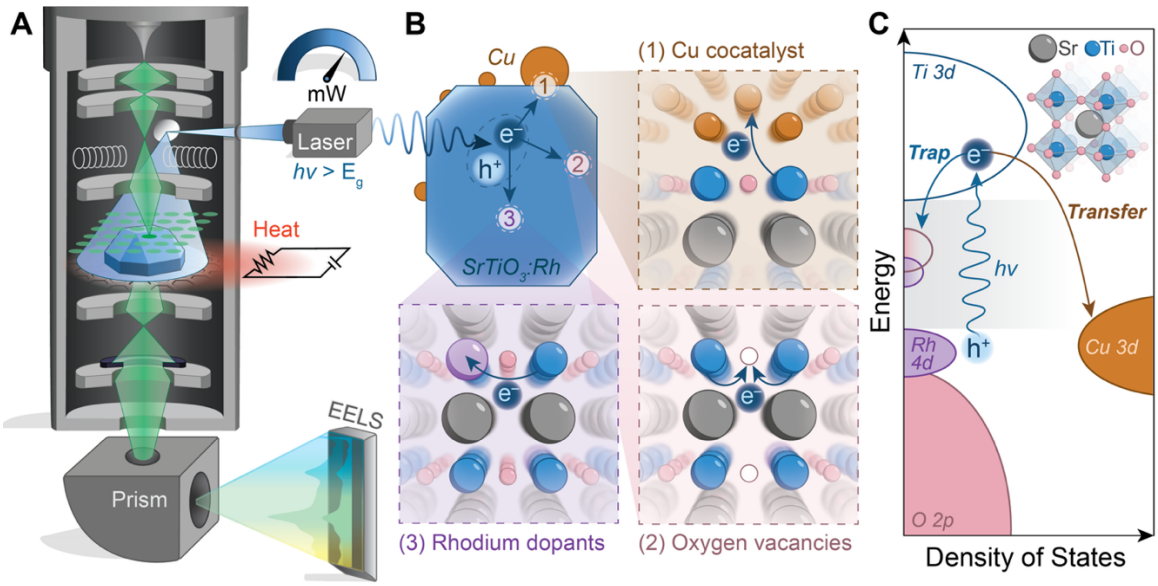

Figure 4.1. Photomodulated STEM-EELS images excited-state photocarrier localization. (**A**) Schematic of the photomodulated STEM-EELS platform, in which continuous-wave laser illumination is coupled into the electron microscope. A resistive heater enables control experiment to differentiate photothermal and photocarrier effects. (**B**) Photocarrier trapping mechanisms in a $SrTiO_3$:Rh nanoparticle. Photogenerated electrons (e^-

) and holes (h^+) may (1) transfer to cocatalysts, (2) trap at oxygen vacancies, or (3) localize at rhodium dopants. (**C**) An energetic landscape of photocarrier relaxation pathways in $SrTiO_3$:Rh. The $SrTiO_3$ unit cell is inset. Trapping at midgap Rh *4d* and oxygen-vacancy states (shaded), along with transfer to the Cu cocatalyst, constitute primary decay channels for photoexcited electrons. Photomodulated STEM-EELS images these localization processes with angstrom-scale spatial and sub-eV spectral sensitivities.

4.3 Ground-State STEM Characterization

We characterize the ground-state properties of potential electron traps in a $SrTiO_3$:Rh nanoparticle (**Fig. 4.2A**). Fig. S2 shows an annular dark-field (ADF) images of the nanoparticle without false coloration. Our prior work investigated the location of rhodium dopants at atomic resolution, demonstrating that rhodium can substitute for both strontium and titanium atoms in the $SrTiO_3$ lattice, with a preference for titanium substitution and a uniform dopant distribution across the nanoparticle.[19] Meanwhile, oxygen vacancies in $SrTiO_3$ nanoparticles are localized at the surface.[20–22] Oxygen vacancies are thermodynamically favored defects in $SrTiO_3$. These well-studied vacancies form readily under high-temperature synthesis conditions and are further promoted by aliovalent Rh dopants and excess Sr used in our synthetic approach.[15,23,24]

We characterize the $SrTiO_3$:Rh surface oxygen vacancies using core-loss STEM-EELS (**Fig. 4.2B**). Oxygen vacancies act as n-type dopants in $SrTiO_3$ while increasing polaron formation, introducing trap states, and ultimately limiting carrier mobility.[14,24,25] Core-loss EELS probes core electrons transitioning into the $SrTiO_3$:Rh CBs, relaying the nanoparticle's electronic structure and composition with elemental specificity.[26] We measure the Ti $L_{2,3}$ and O K edges of $SrTiO_3$:Rh with 2 nm resolution (**Fig. 4.2B**). Comparing spectra averaged at the nanoparticle's surface and bulk indicates that oxygen vacancies broaden the Ti $L_{2,3}$ edge and decrease the O K edge signal.[27,28] We employ DFT and the Bethe–Salpeter equation (BSE) (DFT+BSE) to model core-loss spectra of bulk $SrTiO_3$, shown as the overlaid solid lines in **Fig. 4.2B**. The calculated spectra of undoped $SrTiO_3$ calculations are consistent with the measured spectra of $SrTiO_3$:Rh at this 1 wt% rhodium dopant concentration.

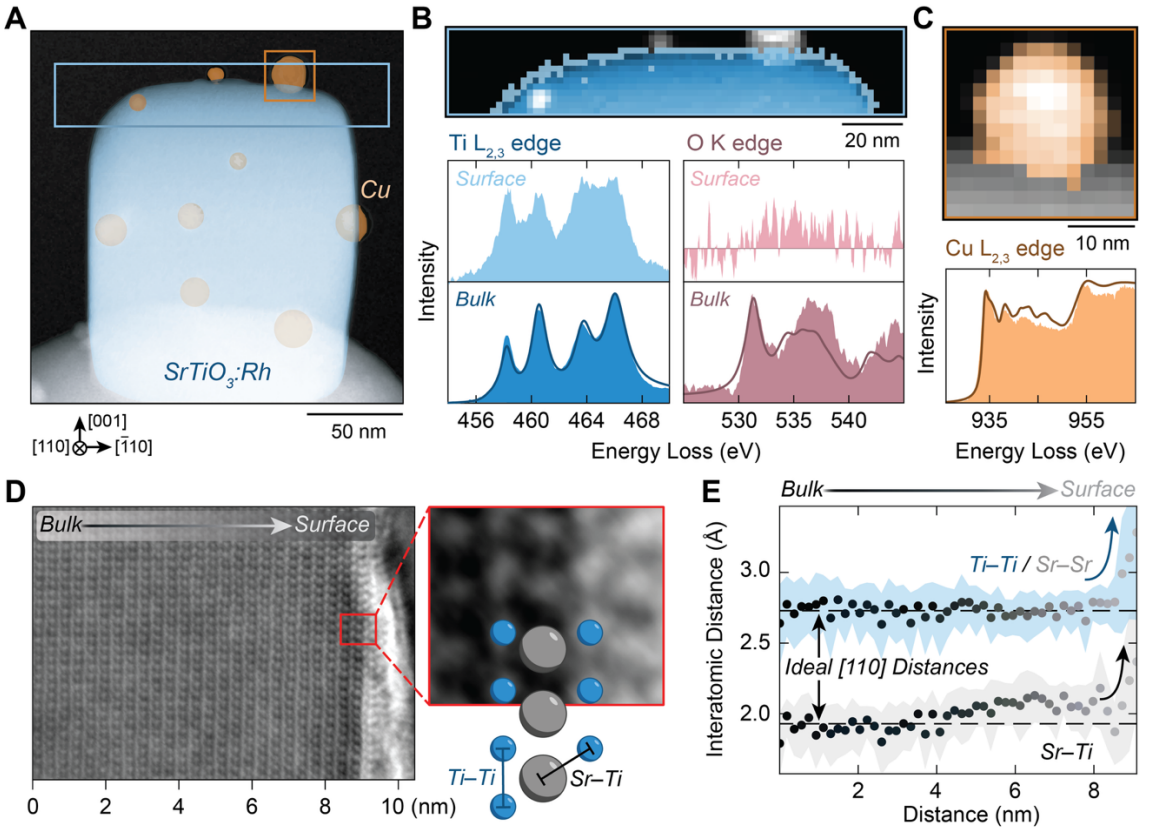

Figure 4.2. Ground-state imaging of photocarrier trap sites in $SrTiO_3$:Rh. (**A**) False-colored ADF image of a $SrTiO_3$:Rh/Cu nanoparticle on sintered $SrTiO_3$:Rh. The STEM-EELS acquisition regions are outlined; $SrTiO_3$:Rh is shown in blue and Cu in orange. (**B**) Spatially resolved STEM-EELS map and corresponding Ti $L_{2,3}$- and O K-edge spectra from the $SrTiO_3$:Rh nanoparticle. DFT+BSE-calculated spectra of both edges for crystalline $SrTiO_3$ are overlaid. (**C**) STEM-EELS map of the Cu $L_{2,3}$ edge, indicating a Cu (80%) and Cu_2O (20%) blend via DFT+BSE calculations. (**D**) Atomic-resolution iDPC-STEM image of an undoped $SrTiO_3$ nanoparticle, highlighting the oxygen-deficient $SrTiO_{3-x}$ surface. Sr and Ti atomic column positions are fitted to quantify deviations in lattice spacing as a function of depth. (**E**) Extracted Ti–Ti/Sr–Sr and Sr–Ti interatomic distances indicate tensile strain at the nanoparticle surface, consistent with strain induced by oxygen vacancies. Shading denotes the standard deviation of the extracted interatomic distance. All nanoparticles are imaged along the [110] zone axis.

Cocatalysts on doped $SrTiO_3$ spatially isolate photoexcited electrons and holes, increasing the photocarriers' excited-state lifetimes by minimizing electron–hole recombination.[3,29,30] For a Cu–$SrTiO_3$:Rh junction, photoexcited electrons are expected to transfer into copper due to the heterojunction's Fermi level alignment.[31] We use core-loss STEM-EELS to characterize a copper nanoparticle on the $SrTiO_3$:Rh surface (**Fig. 4.2C**). We measure the nanoparticle as 80% Cu and 20% Cu_2O, determined using a non-negative least squares linear combination fit of Cu(0) metal and Cu_2O oxide DFT+BSE-calculated spectra.[32,33] Spatially-averaged STEM-EEL spectra further indicate 100% metallic Cu at the Cu–$SrTiO_3$:Rh interface, likely due to preferential oxidation along the nanoparticle's facets or interfacial electron accumulation suppressing oxidation.[34,35] Nanoprobe diffraction measurements show that both the Cu and $SrTiO_3$ nanoparticles are [110]-oriented. Spectral DFT+BSE calculations and fitting, as well as diffraction data, are presented in the Supplementary Text and Figs. S3 and S4.

We perform atomic-resolution integrated differential phase contrast (iDPC) STEM imaging of the $SrTiO_3$:Rh surface atoms (**Fig. 4.2D**). iDPC simultaneously resolves the atomic positions of both strontium and titanium atomic columns, oxygen columns yield weaker contrast and are not resolved. We map the Sr and Ti atomic columns by identifying circular atomic features via template matching and fit their position with a 2D Gaussian profile. We analyze these fit positions to calculate the interatomic distances between Sr–Ti and Ti–Ti / Sr–Sr (**Fig. 4.2E**). The interatomic distances both increase by >0.5 Å at the nanoparticle's surface and indicate a ~1–2 nm oxygen-vacancy layer. Our iDPC image analysis is consistent with prior findings that increasing tensile strain in $SrTiO_3$ correlates with oxygen vacancy concentration, as evidenced by larger lattice parameters in oxygen-depleted $SrTiO_{3-x}$.[36] We attribute the bright contrast of the surface layer to the high oxygen vacancy concentration and the misorientation of atoms off zone axis. Atomic-resolution image fitting and analysis are shown in Figs. S5 and S6.

4.4 Low-Loss EELS Modeling

Photomodulated STEM-EELS readily resolves a material's loss function with low-loss EELS, as the signal-to-noise ratio is much higher than core-loss excitations. However, the loss function is complicated by overlapping interband transitions and bulk plasmon oscillations, and it remains poorly understood for semiconductors. Although the free electron model readily predicts metals' bulk plasmon energies, multi-element semiconductors like $SrTiO_3$ host complex plasmon modes confined to the valence band.[37] The bulk plasmons in $SrTiO_3$ are quantized oscillations of valence band electrons. Prior work utilized vacuum ultraviolet reflectivity to characterize the low-loss modes in $SrTiO_3$.[38] Attempting to interpret plasmon energy shifts in situ, following heating or photoexcitation, introduces further complexity. The spectral effects induced by locally trapped photocarriers as opposed to photothermal heating must be differentiated. We implement band-structure-projected DFT and TDDFT calculations to interpret the origin of $SrTiO_3$'s loss function in both the ground and excited electronic states (**Fig. 4.3**).

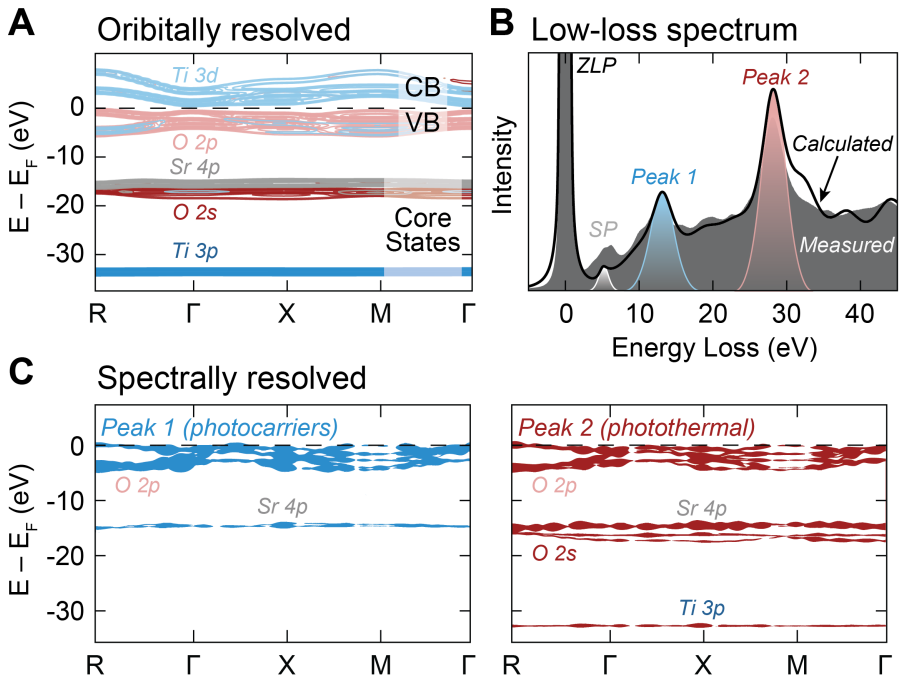

Figure 4.3. Identifying the origin of $SrTiO_3$ low-loss EELS peaks. **(A)** Orbitally resolved band structure of $SrTiO_3$ calculated by DFT. Sr, Ti, and O orbitals are mapped onto the

$SrTiO_3$ band structure with the band energy calibrated to the Fermi level (E_F). (**B**) Measured low-loss EELS from a $SrTiO_3$ nanoparticle with the TDDFT-calculated spectrum overlaid as the solid black line. Spectra are aligned using the zero-loss peak (ZLP). One surface plasmon (SP) and two bulk plasmon resonance peaks are identified for subsequent analysis. (**C**) Spectrally resolved band structure projections for the two bulk plasmon peaks in (B) are calculated using TDDFT. Peak 1 predominantly couples to O *2p* electrons near the valence band maximum, whereas peak 2 is produced from plasmon oscillations of valence electrons in all orbitals.

We first use DFT to orbitally resolve the band structure of $SrTiO_3$ (**Fig. 4.3A**). We project the atomic orbitals of $SrTiO_3$ into energy and momentum space. The calculation indicates that the CB and VB are composed of Ti *3d* and O *2p* orbitals, respectively. Photoexcited electron and hole distributions in the steady state predominantly thermalize to the CB minimum and VB maximum, respectively. Otherwise, the photocarriers become trapped in midgap states. The lower energy Sr *4p*, O *2s*, and Ti *3p* core-level orbitals will not host photocarrier dynamics. While our pseudopotentials underestimate the $SrTiO_3$ bandgap due to the commonly reported self-interaction error and derivative discontinuity, our band structure and TDDFT EELS calculations nevertheless align with the experiment.[39,40] Figure S7 shows the calculated band structure without orbitals projected.

We use TDDFT to accurately interpret the low-loss spectrum of undoped $SrTiO_3$ (**Fig. 4.3B**). Low-loss EEL spectra are aligned by setting the zero-loss peak (ZLP) to 0 eV. The ZLP consists of elastically scattered electrons, defining the measurement's 0.45 eV spectral resolution. For $SrTiO_3$, numerous plasmon modes and interband transitions are resolved. This includes the first plasmon mode at 5 eV, which corresponds to surface plasmon (SP) modes of electrons at the VB maximum (Fig. S8). Two intense bulk plasmon modes labeled "peak 1" and "peak 2" are highlighted. Both peaks exhibit multiple shoulder peaks. A TDDFT-calculated spectrum is overlaid on the experimental measurement in **Fig. 4.3B**. The TDDFT spectrum is calculated using the open-source Liouville-Lanczos solver in the turboEELS package (see Materials and Methods).[41]

We next determine which electrons in $SrTiO_3$ correspond to each plasmon peak (**Fig. 4.3C**). We modify the turboEELS solver to project select peaks in the loss function onto the band structure, thereby identifying the valence electrons that produce each peak. The developed spectral projection method follows our previously reported work and that of others.[42–44] As shown in **Fig. 4.3C**, peak 1 corresponds to higher-lying VB states, while additional core states contribute to peak 2. As a result, peak 1 is highly sensitive to photoexcited carriers in the VBs. Peak 2, by contrast, is delocalized across multiple atoms and core states, making it more sensitive to lattice expansion following photothermal heating and less sensitive to localized photocarriers. The SP and a 40 eV bulk plasmon are projected and spectrally resolved in Fig. S9, and Movie S1 depicts an iterative spectral projection from 2–50 eV.

4.5 Photomodulated STEM-EELS Imaging

Photomodulated STEM-EELS enables direct imaging of trapped photocarriers in $SrTiO_3$:Rh by spectrally resolving peak 1 (primarily sensitive to photocarriers) and 2 (probing photothermal heating as a control) as a function of laser illumination power. While all modes in the spectrum are sensitive to both photocarriers and heating, our spectral assignment differentiates photothermal temperature from photocarriers. Continuous-wave photoexcitation of the $SrTiO_3$:Rh nanoparticle induces subtle shifts in its average EEL spectrum acquired across a STEM-EELS image (**Fig. 4.4A**). Temperature-dependent measurements using a resistive heating holder are used as a control for photothermal heating effects. We perform and average two cycles of power- and temperature-dependent STEM-EELS to control current and hysteresis effects, reported in Figs. S10 and S11 and Table S1 and S2.

We first analyze our photomodulated low-loss measurements by calculating image-averaged differential spectra, which facilitiates interpretation of the subtle spectral changes (**Fig. 4.4B**). The pronounced amplitude modulation over 2–8 eV likely reflects a near-surface electromagnetic (EM) response associated with surface polaritonic excitations, rather than only a static field or plasma. Denoted as “EM field,” this signal may arise from surface phonon polaritons or surface plasmon-phonon polaritons (SPPs) commonly reported in

$SrTiO_3$.[45–47] Its intensity depends on both the electron-beam current and the laser irradiance, consistent with beam coupling to photoinduced near-surface modes. These excitations extended 1–3 px beyond the dark-field image intensity and the spatially-resolved carrier and heating signatures. Prior Lorentz imaging measurements on $SrTiO_3$:Rh mapped phase shifts associated with photoinduced fields with high precision,[48] whereas the present STEM-EELS measurements additionally probe electron energy loss into these excitations and therefore provide more direct information about the character of the states contributing to the near-surface response.

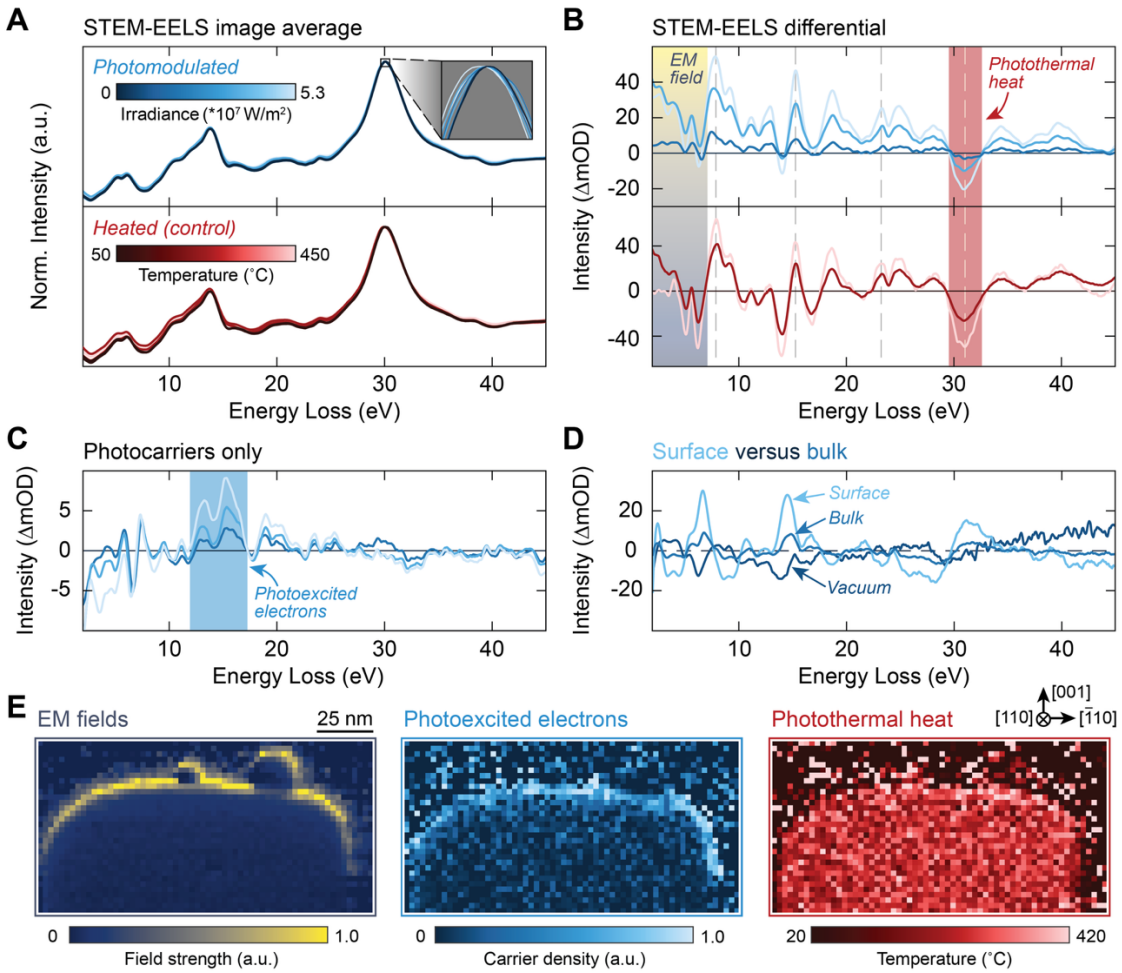

Figure 4.4. Photomodulated STEM-EELS imaging. (**A**) Laser power- and temperature-dependent STEM-EEL spectra averaged across a spectral image of the $SrTiO_3$:Rh/Cu nanoparticle in **Fig. 4.2**. The color bars indicate the irradiance and temperature set throughout

two hysteresis cycles, and the inset highlights the redshift of bulk plasmon peak 2. (**B**) Corresponding differential spectra averaged over both cycles. Differential spectra were calculated using reference "ground state" spectra at 0 W · m^{-2} irradiance and 50 °C temperature, respectively. Spectral regions used to map local EM fields and photothermal heating are highlighted. (**C**) Photomodulated EEL spectra for 5.3×10^7 W·m^{-2} laser irradiance with EM field and photothermal heat backgrounds subtracted. The spectral region used to map photoexcited electrons is highlighted. (**D**) Differential photomodulated spectra at select regions of the photomodulated, background-subtracted STEM-EELS image. Arrows indicate the region on the nanoparticle where spectra were acquired. (**E**) Photomodulated STEM-EELS maps for 5.3×10^7 W·m^{-2} laser irradiance. Angstrom-scale EM fields, photoexcited electrons, and photothermal heat are mapped using the differential spectral amplitude over spectral regions highlighted in (B) and (C).

Temperature-dependent effects manifest in both the photomodulated and heated STEM-EELS differential spectra (**Fig. 4.4B**). The differential peaks from the heating control can be directly mapped onto the photomodulated spectrum, and nearly all the differential amplitude corresponds to thermal effects. These thermal spectral shifts are a result of the $SrTiO_3$ thermal lattice expansion, used as a contrast mechanism in prior EELS thermometry studies.[9–11] We employ temperature-dependent TDDFT calculations to investigate the spectral shifts induced by thermal lattice expansion (Fig. S12). The multi-mode $SrTiO_3$ peak shifts are more complex than that of single-element metals and semiconductors reported in prior plasmon thermometry studies.[9,10]

The effects of photocarriers become more apparent after subtracting the EM-field and photothermal-heating backgrounds (**Fig. 4.4C**). The primary feature in the differential spectrum is a positive signal at bulk plasmon peak 1 induced by photocarriers. The differential signal induced by the EM field (<8 eV) and the photocarriers (12–16 eV) matches well with our ab initio TDDFT calculations of photocarriers in $SrTiO_3$ (Fig. S13). We model the influence of photoexcited electrons and holes using two chemical potentials, one for electrons and one for holes in respective CBs and VBs, by using constrained density

functional perturbation theory (cDFPT) as an input for our TDDFT calculations (see Materials and Methods).[41,49] EM-field and photothermal-heating background fits are shown in Fig S14.

The angstrom-scale STEM-EEL spectra vary across the nanoparticle due to heterogeneity of Cu cocatalysts, surface oxygen vacancies, and vacuum background (Figs. S15–S17). To isolate photoexcited carriers from these spatially varying spectral backgrounds, we implement a rigid-shift analysis at every pixel in the photomodulated STEM-EELS image. For each pixel, we begin with the background-subtracted photomodulated differential spectrum, calculated as the natural logarithm acquired with the laser on divided by laser off, where the laser power is set to 5.3×10^{7} W•m^{-2}. We then rigidly shift the underlying ground-state spectrum to best match the differential spectrum's spectral intensity. The best match is then directly subtracted from the photomodulated differential spectrum. As a result, we remove pixel-dependent heating effects resulting from the photothermal heating spectral redshift. Averaging spectra in the thermal and background-corrected photomodulated image shows that the photocarrier differential signal increases at the nanoparticle's surface, and the nanoparticle's bulk signal amplitude is comparable to the vacuum without photocarriers (**Fig. 4.4D**).

We spatially map the differential spectral amplitude at the highest 5.3×10^{7} W · m^{-2} laser irradiance (**Fig. 4.4E**). The nanoparticle is imaged along the [110] zone axis with 14 Å STEM-EELS resolution. We resolve an EM field strength highest at the nanoparticle's [001] facet, like prior Lorentz imaging studies (**Fig. 4.4E**, left panel).[48] Photoexcited electrons are measured to be localized at the [001] facet where the SSPs EM field is highest (**Fig. 4.4E**, middle panel). We quantify the photocarrier density by integrating the spectral intensity predicted by *ab initio* TDDFT calculations, reporting a surface photocarrier density of $\sim1\times10^{19}$ cm^{-3} at this irradiance, ~70% greater than the bulk photocarrier density. Fig. S18 compares the relative intensity of the measured dark-field signal, differential EM fields, temperature, and photocarrier density as quantified by the STEM-EELS mapping along the [001] and [$\bar{1}$10] zone axes. The relative contribution from electrons and holes is difficult to

quantify due to the inseparability of electrons and holes in our cDFPT model. However, photoexcited electrons more dramatically influence the low-loss spectrum by introducing new modes after filling previously unoccupied CB states. The nanoparticle's uniform photothermal heating serves as an experimental control, which we map using the raw differential intensity of bulk plasmon peak 2 in **Fig. 4.4B**. Thermal dissipation reaches an equilibrium at nanometer length scales in the steady state, so any signal fluctuations within the nanoparticle result from signal-to-noise limits (**Fig. 4.4E**, right panel). Additional experimental controls for the spatially resolved SP, image drift, nanoparticle thickness, and the energetic shifts of bulk plasmon peak 2 are presented in Figs. S19–22. Supplementary Movies S2–S6 highlight these irradiance-dependent differential shifts.

While photomodulated STEM-EELS provides critical insights, it is not without challenges. First, access to an optically coupled STEM with high spatial and energy resolution remains a significant barrier. Although recent advances in direct electron detectors and imaging filters greatly improve signal-to-noise, long acquisition times are still required. These acquisitions also entail precise specimen spatial drift control and minimal ZLP energy drift (see Supplementary Text). Second, interpreting differential STEM-EEL spectra is analytically challenging, aided here by TDDFT calculations. It is already difficult to distinguish bulk plasmons from interband transitions in the loss function. Our TDDFT calculations of the $SrTiO_3$ dielectric function emphasize the complex interplay between interband transitions and bulk plasmons. The real component of the dielectric function does not cross zero at the plasmon modes due to lossy modes and screening.[50] Third, the specimen must remain stable under electron irradiation, resistive heating, and photoexcitation. In this work, the beam current and scan rate were optimized to minimize the formation of additional oxygen vacancies during irradiance-dependent hysteresis cycles, and pretreatment conditions with high power laser exposure and 450 ˚C heating were conducted in vacuum to further reduce structural changes during STEM-EELS imaging.[51]

4.6 Conclusion

The development of photomodulated STEM-EELS introduces new spatial limits for imaging photoexcited carrier and thermal distributions. The combined spectral and spatial resolutions exceed those of existing imaging techniques, including scanning probe microscopy, optical interferometric scattering, Lorentz microscopy, and EELS thermometry. In this work, we quantitatively map the photoexcited electron density in $SrTiO_3$:Rh/Cu. Directly imaging the photocarrier-induced EM fields extending beyond the nanoparticle's surface, as well as photothermal heating uniform across the nanoparticle's bulk, indicates the utility of the photomodulated STEM-EELS approach. Our imaging results agree well with previous synthetic methods used to design doped $SrTiO_3$ photocatalysts with near-unity photocatalytic quantum efficiencies. Specifically, photocarriers selectively transport along the nanoparticle's [001] facet and transfer into surface cocatalysts. We also developed a TDDFT method that projects the EEL spectrum onto the material's band structure, thereby indicating the electronic origin of bulk plasmon modes. This new theoretical advance is critical for a deeper interpretation of the convoluted features in low-loss spectra. The proposed technique offers a general approach to spatially resolving carrier- and thermal-induced phenomena in nanoscale structures, thereby broadening its appeal.

4.7 Supporting Information

The supporting information—containing figures and data labelled S[X], Materials and Methods, Supplementary Text, Figs. S1 to S23, Tables S1 to S2, Movies S1 to S6—is available free of charge at: https://doi.org/10.22002/wheak-c7d39

4.8 References

(1) Sachs, M.; Harnett-Caulfield, L.; Pastor, E.; Davies, B.; Sowood, D. J. C.; Moss, B.; Kafizas, A.; Nelson, J.; Walsh, A.; Durrant, J. R. Metal-Centred States Control Carrier Lifetimes in Transition Metal Oxide Photocatalysts. *Nat. Chem.* **2025**, *17* (9), 1348–1355. https://doi.org/10.1038/s41557-025-01868-y.

(2) Luo, H.; Vequizo, J. J. M.; Ye, Z.; Han, F.; Chi, J.; Yan, J.; Yamakata, A.; Shangguan, W.; Jiang, Z. Facet-Engineered $SrTiO_3$:Rh via Solid-State Ionic Doping for Efficient Z-Scheme Overall Water Splitting. *J. Catal.* **2026**, *453*, 116551. https://doi.org/10.1016/j.jcat.2025.116551.

(3) Takata, T.; Jiang, J.; Sakata, Y.; Nakabayashi, M.; Shibata, N.; Nandal, V.; Seki, K.; Hisatomi, T.; Domen, K. Photocatalytic Water Splitting with a Quantum Efficiency of Almost Unity. *Nature* **2020**, *581* (7809), 411–414. https://doi.org/10.1038/s41586-020-2278-9.

(4) Zhang, P.; Wang, T.; Chang, X.; Gong, J. Effective Charge Carrier Utilization in Photocatalytic Conversions. *Acc. Chem. Res.* **2016**, *49* (5), 911–921. https://doi.org/10.1021/acs.accounts.6b00036.

(5) Xue, J.; Fujitsuka, M.; Tachikawa, T.; Bao, J.; Majima, T. Charge Trapping in Semiconductor Photocatalysts: A Time- and Space-Domain Perspective. *J. Am. Chem. Soc.* **2024**, *146* (13), 8787–8799. https://doi.org/10.1021/jacs.3c14757.

(6) Delor, M.; Weaver, H. L.; Yu, Q.; Ginsberg, N. S. Imaging Material Functionality through Three-Dimensional Nanoscale Tracking of Energy Flow. *Nat. Mater.* **2020**, *19* (1), 56–62. https://doi.org/10.1038/s41563-019-0498-x.

(7) Chen, R.; Fan, F.; Dittrich, T.; Li, C. Imaging Photogenerated Charge Carriers on Surfaces and Interfaces of Photocatalysts with Surface Photovoltage Microscopy. *Chem. Soc. Rev.* **2018**, *47* (22), 8238–8262. https://doi.org/10.1039/C8CS00320C.

(8) Chen, R.; Ren, Z.; Liang, Y.; Zhang, G.; Dittrich, T.; Liu, R.; Liu, Y.; Zhao, Y.; Pang, S.; An, H.; Ni, C.; Zhou, P.; Han, K.; Fan, F.; Li, C. Spatiotemporal Imaging of Charge Transfer in Photocatalyst Particles. *Nature* **2022**, *610* (7931), 296–301. https://doi.org/10.1038/s41586-022-05183-1.

(9) Castioni, F.; Auad, Y.; Blazit, J.-D.; Li, X.; Woo, S. Y.; Watanabe, K.; Taniguchi, T.; Ho, C.-H.; Stéphan, O.; Kociak, M.; Tizei, L. H. G. Nanosecond Nanothermometry in an Electron Microscope. *Nano Lett.* **2025**, *25* (4), 1601–1608. https://doi.org/10.1021/acs.nanolett.4c05692.

(10) Mecklenburg, M.; Hubbard, W. A.; White, E. R.; Dhall, R.; Cronin, S. B.; Aloni, S.; Regan, B. C. Nanoscale Temperature Mapping in Operating Microelectronic Devices. *Science* **2015**, *347* (6222), 629–632. https://doi.org/10.1126/science.aaa2433.

(11) Palmer, L. D.; Lee, W.; Durham, D. B.; Fajardo, J. Jr.; Liu, Y.; Talin, A. A.; Gage, T. E.; Cushing, S. K. Nanoscale and Element-Specific Lattice Temperature Measurements Using Core-Loss Electron Energy-Loss Spectroscopy. *ACS Phys. Chem. Au* **2025**, *5* (6), 589–598. https://doi.org/10.1021/acsphyschemau.5c00044.

(12) Liu, F.; Mao, R.; Liu, Z.; Du, J.; Gao, P. Probing Phonon Transport Dynamics across an Interface by Electron Microscopy. *Nature* **2025**, *642* (8069), 941–946. https://doi.org/10.1038/s41586-025-09108-6.

(13) Moss, B.; Wang, Q.; Butler, K. T.; Grau-Crespo, R.; Selim, S.; Regoutz, A.; Hisatomi, T.; Godin, R.; Payne, D. J.; Kafizas, A.; Domen, K.; Steier, L.; Durrant, J. R. Linking in Situ Charge Accumulation to Electronic Structure in Doped $SrTiO_3$ Reveals Design Principles for Hydrogen-Evolving Photocatalysts. *Nat. Mater.* **2021**, *20* (4), 511–517. https://doi.org/10.1038/s41563-020-00868-2.

(14) Zutter, B.; Chen, Z.; Barrera, L.; Gaieck, W.; Lapp, A. S.; Watanabe, K.; Kudo, A.; Esposito, D. V.; Bala Chandran, R.; Ardo, S.; Talin, A. A. Single-Particle Measurements Reveal the Origin of Low Solar-to-Hydrogen Efficiency of Rh-Doped $SrTiO_3$ Photocatalysts. *ACS Nano* **2023**, *17* (10), 9405–9414. https://doi.org/10.1021/acsnano.3c01448.

(15) Modak, B.; Ghosh, S. K. Exploring the Role of La Codoping beyond Charge Compensation for Enhanced Hydrogen Evolution by Rh–$SrTiO_3$. *J. Phys. Chem. B* **2015**, *119* (34), 11089–11098. https://doi.org/10.1021/acs.jpcb.5b02906.

(16) Liu, H.; Michelsen, J. M.; Mendes, J. L.; Klein, I. M.; Bauers, S. R.; Evans, J. M.; Zakutayev, A.; Cushing, S. K. Measuring Photoexcited Electron and Hole Dynamics in ZnTe and Modeling Excited State Core-Valence Effects in Transient Extreme Ultraviolet Reflection Spectroscopy. *J. Phys. Chem. Lett.* **2023**, *14* (8), 2106–2111. https://doi.org/10.1021/acs.jpclett.2c03894.

(17) Cushing, S. K.; Molesky, I. J. P.; de Roulet, B. R.; Lee, A.; Marsh, B. M.; Szoke, S.; Vaida, M. E.; Leone, S. R. Layer-Resolved Ultrafast Extreme Ultraviolet Measurement of Hole Transport in a Ni-TiO_2-Si Photoanode. *Sci. Adv.* **2020**, *6* (14), eaay6650. https://doi.org/10.1126/sciadv.aay6650.

(18) Zürch, M.; Chang, H.-T.; Borja, L. J.; Kraus, P. M.; Cushing, S. K.; Gandman, A.; Kaplan, C. J.; Oh, M. H.; Prell, J. S.; Prendergast, D.; Pemmaraju, C. D.; Neumark, D. M.; Leone, S. R. Direct and Simultaneous Observation of Ultrafast Electron and Hole Dynamics in Germanium. *Nat. Commun.* **2017**, *8* (1), 15734. https://doi.org/10.1038/ncomms15734.

(19) Mulvey, J. T.; Prasad, P. R.; Chen, Z.; Palmer, L. D.; Layne, B. W.; Korican-Barlay, E.; Watanabe, K.; Xu, M.; Talin, A. A.; Pan, X.; Kudo, A.; Cushing, S. K.; Ardo, S.; Patterson, J. P. Direct Observation of Rh and La Dopant Positions in $SrTiO_3$ Nanoparticles with Atomic-Scale Electron Microscopy. *ACS Appl. Mater. Interfaces* **2025**, *17* (46), 63374–63383. https://doi.org/10.1021/acsami.5c15338.

(20) Day, M. L.; Hamza, M. A.; Evans, J. D.; Shearer, C. Excess Al Reduces Photocatalytic Activity of Al-Doped $SrTiO_3$ Nanostructures. *ACS Appl. Nano Mater.* **2026**, *9* (4), 1748–1759. https://doi.org/10.1021/acsanm.5c04384.

(21) Muller, D. A.; Nakagawa, N.; Ohtomo, A.; Grazul, J. L.; Hwang, H. Y. Atomic-Scale Imaging of Nanoengineered Oxygen Vacancy Profiles in $SrTiO_3$. *Nature* **2004**, *430* (7000), 657–661. https://doi.org/10.1038/nature02756.

(22) Shetty, S.; Sinha, S. K.; Ahmad, R.; Singh, A. K.; Van Tendeloo, G.; Ravishankar, N. Existence of Ti^{2+} States on the Surface of Heavily Reduced $SrTiO_3$ Nanocubes. *Chem. Mater.* **2017**, *29* (23), 9887–9891. https://doi.org/10.1021/acs.chemmater.7b04113.

(23) Liu, B.; Cooper, V. R.; Xu, H.; Xiao, H.; Zhang, Y.; Weber, W. J. Composition Dependent Intrinsic Defect Structures in $SrTiO_3$. *Phys. Chem. Chem. Phys.* **2014**, *16* (29), 15590–15596. https://doi.org/10.1039/C4CP01510J.

(24) Tan, H.; Zhao, Z.; Zhu, W.; Coker, E. N.; Li, B.; Zheng, M.; Yu, W.; Fan, H.; Sun, Z. Oxygen Vacancy Enhanced Photocatalytic Activity of Pervoskite $SrTiO_3$. *ACS Appl. Mater. Interfaces* **2014**, *6* (21), 19184–19190. https://doi.org/10.1021/am5051907.

(25) Janotti, A.; Varley, J. B.; Choi, M.; Van de Walle, C. G. Vacancies and Small Polarons in $SrTiO_3$. *Phys. Rev. B* **2014**, *90* (8), 085202. https://doi.org/10.1103/PhysRevB.90.085202.

(26) Kim, Y.-J.; Palmer, L. D.; Lee, W.; Heller, N. J.; Cushing, S. K. Using Electron Energy-Loss Spectroscopy to Measure Nanoscale Electronic and Vibrational Dynamics in a TEM. *J. Chem. Phys.* **2023**, *159* (5), 050901. https://doi.org/10.1063/5.0147356.

(27) Lee, S. A.; Jeong, H.; Woo, S.; Hwang, J.-Y.; Choi, S.-Y.; Kim, S.-D.; Choi, M.; Roh, S.; Yu, H.; Hwang, J.; Kim, S. W.; Choi, W. S. Phase Transitions via Selective Elemental Vacancy Engineering in Complex Oxide Thin Films. *Sci. Rep.* **2016**, *6* (1), 23649. https://doi.org/10.1038/srep23649.

(28) Klie, R. F.; Browning, N. D. Atomic Scale Characterization of Oxygen Vacancy Segregation at $SrTiO_3$ Grain Boundaries. *Appl. Phys. Lett.* **2000**, *77* (23), 3737–3739. https://doi.org/10.1063/1.1330572.

(29) Kikuchi, E.; Saito, N.; Yamaguchi, Y.; Kudo, A. Temperature Dependence of Photocatalytic Water Splitting under Visible Light Irradiation over Ir- and Sb-Codoped $SrTiO_3$:Al. *J. Phys. Chem. C* **2025**, *129* (5), 2381–2390. https://doi.org/10.1021/acs.jpcc.4c07699.

(30) Kaiya, K.; Ueki, Y.; Kawamoto, H.; Watanabe, K.; Yoshino, S.; Yamaguchi, Y.; Kudo, A. Water Splitting over Transition Metal-Doped $SrTiO_3$ Photocatalysts with Response to Visible Light up to 660 nm. *Chem. Sci.* **2024**, *15* (39), 16025–16033. https://doi.org/10.1039/D4SC03978E.

(31) Wei, W.; Dai, Y.; Lai, K.; Guo, M.; Huang, B. Atomic Cu Adsorption on Defect-Free $SrTiO_3$(001) Surface. *Chem. Phys. Lett.* **2011**, *510* (1), 104–108. https://doi.org/10.1016/j.cplett.2011.05.010.

(32) Chamorro, W.; Shyju, T. S.; Boulet, P.; Migot, S.; Ghanbaja, J.; Miska, P.; Kuppusami, P.; Pierson, J. F. Role of Cu^+ on ZnS:Cu p-Type Semiconductor Films Grown by Sputtering: Influence of Substitutional Cu in the Structural, Optical and Electronic Properties. *RSC Adv.* **2016**, *6* (49), 43480–43488. https://doi.org/10.1039/C6RA05819A.

(33) Nolan, M.; Elliott, S. D. The p-Type Conduction Mechanism in Cu_2O: A First Principles Study. *Phys. Chem. Chem. Phys.* **2006**, *8* (45), 5350–5358. https://doi.org/10.1039/B611969G.

(34) Li, J.; Li, Y.; Wang, Z.; Bian, H.; Hou, Y.; Wang, F.; Xu, G.; Liu, B.; Liu, Y. Ultrahigh Oxidation Resistance and High Electrical Conductivity in Copper-Silver Powder. *Sci. Rep.* **2016**, *6* (1), 39650. https://doi.org/10.1038/srep39650.

(35) Chung, K.; Bang, J.; Thacharon, A.; Song, H. Y.; Kang, S. H.; Jang, W.-S.; Dhull, N.; Thapa, D.; Ajmal, C. M.; Song, B.; Lee, S.-G.; Wang, Z.; Jetybayeva, A.; Hong, S.; Lee, K. H.; Cho, E. J.; Baik, S.; Oh, S. H.; Kim, Y.-M.; Lee, Y. H.; Kim, S.-G.; Kim, S. W. Non-Oxidized Bare Copper Nanoparticles with Surface Excess Electrons in Air. *Nat. Nanotechnol.* **2022**, *17* (3), 285–291. https://doi.org/10.1038/s41565-021-01070-4.

(36) Cai, H. L.; Wu, X. S.; Gao, J. Effect of Oxygen Content on Structural and Transport Properties in $SrTiO_{3-x}$ Thin Films. *Chem. Phys. Lett.* **2009**, *467* (4), 313–317. https://doi.org/10.1016/j.cplett.2008.11.071.

(37) Lee, W.; Palmer, L. D.; Gage, T. E.; Cushing, S. K. Imaging Nanoscale Carrier, Thermal, and Structural Dynamics with Time-Resolved and Ultrafast Electron Energy-Loss Spectroscopy. *Chem. Phys. Rev.* **2025**, *6* (4), 041303. https://doi.org/10.1063/5.0289128.

(38) Bäuerle, D.; Braun, W.; Saile, V.; Sprüssel, G.; Koch, E. E. Vacuum Ultraviolet Reflectivity and Band Structure of $SrTiO_3$ and $BaTiO_3$. *Z. Phys. B* **1978**, *29* (3), 179–184. https://doi.org/10.1007/BF01321179.

(39) Perdew, J. P. Size-Consistency, Self-Interaction Correction, and Derivative Discontinuity in Density Functional Theory. *Adv. Quantum Chem.* **1990**, *21*, 113–134. https://doi.org/10.1016/S0065-3276(08)60594-8.

(40) Bao, J. L.; Gagliardi, L.; Truhlar, D. G. Self-Interaction Error in Density Functional Theory: An Appraisal. *J. Phys. Chem. Lett.* **2018**, *9* (9), 2353–2358. https://doi.org/10.1021/acs.jpclett.8b00242.

(41) Motornyi, O.; Raynaud, M.; Dal Corso, A.; Vast, N. Simulation of Electron Energy Loss Spectra with the turboEELS and Thermo_pw Codes. *J. Phys.: Conf. Ser.* **2018**, *1136* (1), 012008. https://doi.org/10.1088/1742-6596/1136/1/012008.

(42) Begum-Hudde, V.; Lojewski, T.; Rothenbach, N.; Eggert, B.; Eschenlohr, A.; Ollefs, K.; Gruner, M. E.; Pentcheva, R. Nature of Excitons in the Ti L- and O K-Edges of x-Ray Absorption Spectra in Bulk $SrTiO_3$ from a Combined First Principles and Many-Body Theory Approach. *Phys. Rev. Res.* **2023**, *5* (1), 013199. https://doi.org/10.1103/PhysRevResearch.5.013199.

(43) Hinton, J. K.; Schacher, D.; Lee, W.; Smith, G. A.; Siska, E.; Park, C.; Ellison, P. B.; Cushing, S. K.; Schwartz, C. P.; Lawler, K. V.; Salamat, A. Electronic Topological Transitions in Cadmium under Pressure Studied via Theoretical and Experimental X-Ray Absorption Spectroscopy. *Phys. Rev. B* **2024**, *110* (20), 205118. https://doi.org/10.1103/PhysRevB.110.205118.

(44) Klein, I. M.; Krotz, A.; Lee, W.; Michelsen, J. M.; Cushing, S. K. Ab Initio Calculations of XUV Ground and Excited States for First-Row Transition Metal Oxides. *J. Phys. Chem. C* **2023**, *127* (2), 1077–1086. https://doi.org/10.1021/acs.jpcc.2c06548.

(45) Herrmann, H.; Oelschlaeger, A.; Widdra, W. Surface Vibrations, Polaritons and Their Coupling to a 2D Electron Gas: Interface-Bound Vibrations at the $SrTiO_3$(001) Surface. *Faraday Discuss.* **2026**. https://doi.org/10.1039/D5FD00166H.

(46) Lahneman, D. J.; Qazilbash, M. M. Hyperspectral Infrared Imaging of Surface Phonon-Polaritons in $SrTiO_3$. *Phys. Rev. B* **2021**, *104* (23), 235433. https://doi.org/10.1103/PhysRevB.104.235433.

(47) Yang, J.-Y.; Cheng, T.; Fei, T.; Zhang, C.; Liu, L. Temperature-Induced Surface Phonon Polaritons Dissipation in Perovskite $SrTiO_3$. *Opt. Lett.* **2021**, *46* (17), 4244–4247. https://doi.org/10.1364/OL.438993.

(48) Haluai, P.; McCartney, M. R.; Wang, Y.; Crozier, P. A. Correlating Photo-Induced Changes in Surface Charge and Electronic Conductivity in Oxide Nanoparticles with In Situ Electron Microscopy. *ACS Nano* **2025**, *19* (21), 19567–19577. https://doi.org/10.1021/acsnano.4c13539.

(49) Marini, G.; Calandra, M. Lattice Dynamics of Photoexcited Insulators from Constrained Density-Functional Perturbation Theory. *Phys. Rev. B* **2021**, *104* (14), 144103. https://doi.org/10.1103/PhysRevB.104.144103.

(50) Nelson, F. J.; Idrobo, J.-C.; Fite, J. D.; Mišković, Z. L.; Pennycook, S. J.; Pantelides, S. T.; Lee, J. U.; Diebold, A. C. Electronic Excitations in Graphene in the 1–50 eV Range: The π and π + σ Peaks Are Not Plasmons. *Nano Lett.* **2014**, *14* (7), 3827–3831. https://doi.org/10.1021/nl500969t.

(51) Li, Y.; Xia, J.; Li, X.; Tian, L.; Qiao, P.; Cao, J.; Zhang, Z.; Meng, Q.; Li, J.; Liu, C.; Meng, X. Atomic-Scale Imaging of Structural Evolution from Anatase TiO_2 to Cubic TiO under Electron Beam Irradiation. *Nano Today* **2024**, *59*, 102532. https://doi.org/10.1016/j.nantod.2024.102532.

C H A P T E R 5

OPTICALLY COUPLED LIQUID-PHASE ELECTRON MICROSCOPY AND THERMOMETRY OF LIGHT-DRIVEN WATER EVAPORATION

Adapted with permission from the following:

Palmer, L. D.[†], Zheng, Y.[†], Zhang, X., Alexander, K. H., Lee, W., Chen, J., Gage, T. E., Cushing, S. K. Optically Coupled Liquid-Phase Electron Microscopy and Thermometry of Light-Driven Water Evaporation. **2026**, In Preparation.

[†]Co-first author.

5.1 Introduction

Photocatalytic water splitting efficiencies are now approaching unity.[1–3] Yet, the nanoscale mechanisms governing photocarrier transport and hydrogen evolution under working conditions remain unresolved. Although recent studies probe carrier dynamics and hydrogen evolution under working conditions, they do not directly image these photoexcited processes at the catalyst–water interface's inherent nanometer length scale.[4–6] Electron energy-loss spectroscopy (EELS) performed with optically coupled liquid phase TEM (optically coupled LPTEM) are a promising route to simultaneously probe photoinduced electronic dynamics in liquids while imaging nanoscale structural evolution. Optically coupled LPTEM and EELS would therefore link photocarrier transport, interfacial restructuring, and hydrogen evolution at the single-particle level. However, further technique development is required to achieve optically coupled EELS and imaging in the liquid phase.

Most LPTEM studies of nanoparticle photocatalysts utilize the electron beam, rather than light, to induce dynamics in the confined aqueous environment. These studies have measured nanoparticle etching, Brownian motion, and radiolysis-driven nanobubble formation.[7–12] Pseudo-photocatalytic water splitting with controlled electron dose aims to mimic light-driven dynamics.[13] While in situ optically coupled LPTEM is rarely demonstrated (**Scheme 5.1**), several works have integrated optical illumination in the TEM to study nanoparticle reactivity in the liquid phase.[14–16] Yet, these prior studies do not often consider light-induced effects on the support membrane and liquid–membrane–gas interface, which can lead to structural changes to the membrane and extreme photothermal temperatures that obscure the nanoparticles' native photocatalytic activity. Although carbon film liquid cells' minimal elastic scattering and thin water thicknesses enable adequate imaging and EELS resolutions, amorphous carbon films (a-C) have low in-plane thermal conductivity and strongly absorb the incident laser. The resulting photothermal heating and thermal dissipation remain poorly understood and are rarely discussed. EELS plasmon thermometry offers one route to probe liquid cell heating by tracking thermally induced plasmon energy shifts associated with thermal expansion.[17,18] However, plasmon thermometry is typically performed to measure

solid-state materials in vacuum and has yet to quantify liquid-phase temperatures under light illumination conditions.

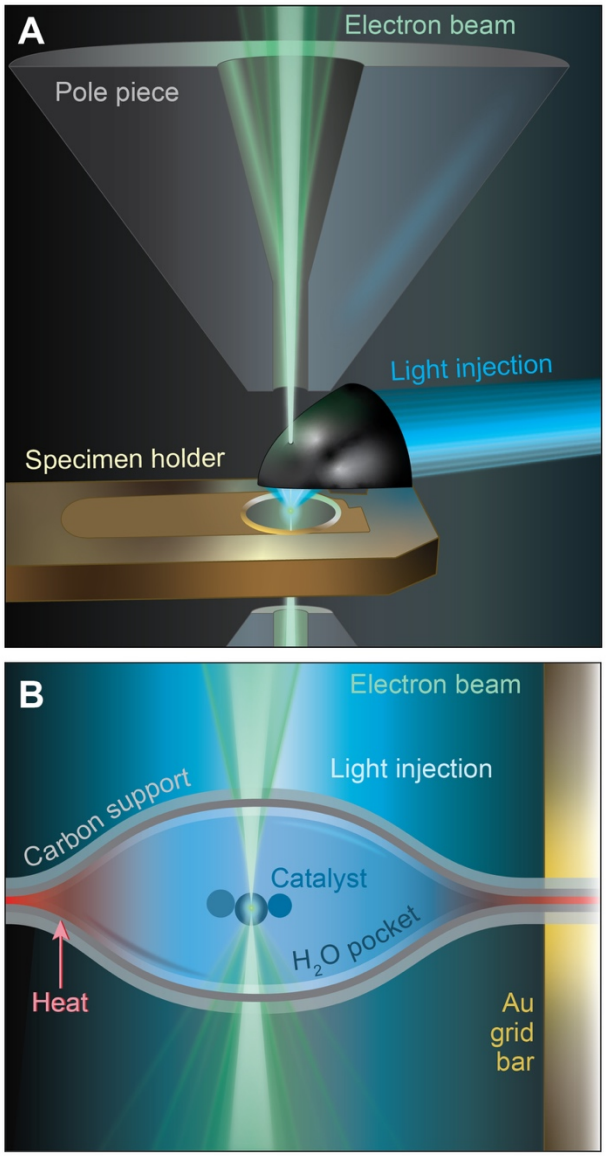

Scheme 5.1. Optically coupled liquid phase electron microscopy. (**A**) The pole piece gap in the optically coupled TEM. Continuous-wave 375 nm light injection is performed using a parabolic mirror. (**B**) A liquid H_2O pocket that contains photocatalytic nanoparticles and is encapsulated by ~25 nm carbon support films. Light injection heats the H_2O pocket and carbon film, and Au grid bars act as heat sinks.

In this work, we utilize a 375 nm continuous-wave laser to perform optically coupled LPTEM and EELS to quantify photothermal heating during light-driven water evaporation (**Scheme 5.1**). The optically coupled electron microscope integrates a parabolic mirror for light injection (**Scheme 5.1A**). The ~10 μm laser diameter illuminates an area larger than most relevant water pocket areas (Fig. S1). Laser illumination results in photothermal heating of both the carbon support film and water pocket. Nearby Au grid bars act as the primary heat sink (**Scheme 5.1B**). We disperse aluminum-doped strontium titanate ($SrTiO_3$:Al) nanoparticle photocatalysts in water. $SrTiO_3$:Al nanoparticles exhibit highly efficient, light-driven water splitting in pure H_2O.[1,2,19] We quantify the liquid cell's photothermal heating and water evaporation rate, factors which largely inhibit our ability to image the $SrTiO_3$:Al nanoparticles perform water splitting. Our results offer a route toward operando LPTEM with EELS.[20,21]

5.2 Results and Discussion

We first measured laser irradiance-dependent low-loss EELS of the a-C films in the absence of water to quantify photothermal heating and assess laser-induced phase changes in the carbon. The low-loss EEL spectrum of the a-C film exhibits features associated with both σ- and π-bonded carbon (**Fig. 5.1A**). Valence electrons in π bonds manifest as a peak centered at 5 eV, and the electrons in both σ and π bonds create a peak centered at 25 eV.[22] The heterogeneous mixture of σ and π bonding in the a-C film indicates a disordered graphitic structure. The non-hydrogenated a-C films utilized in this study were synthesized using thermal evaporation, and they are known to have a disordered graphitic structure.[23,24] EEL spectra acquired during 375 nm light injection have a gradually increasing π peak intensity, indicating that the film becomes more graphitic with laser irradiance. A large redshift of the π+σ peak following the initial light-injection event (**Fig. 5.1A**, inset) is also consistent with laser-induced modification of a-C, potentially indicating that the laser removes weakly bound surface carbon species. This hypothesized laser-induced carbon removal is further supported by a small decrease in apparent film thickness (~0.5 nm; Fig. S3). In addition, the π+σ peak redshifts systematically with increasing photothermal temperature.

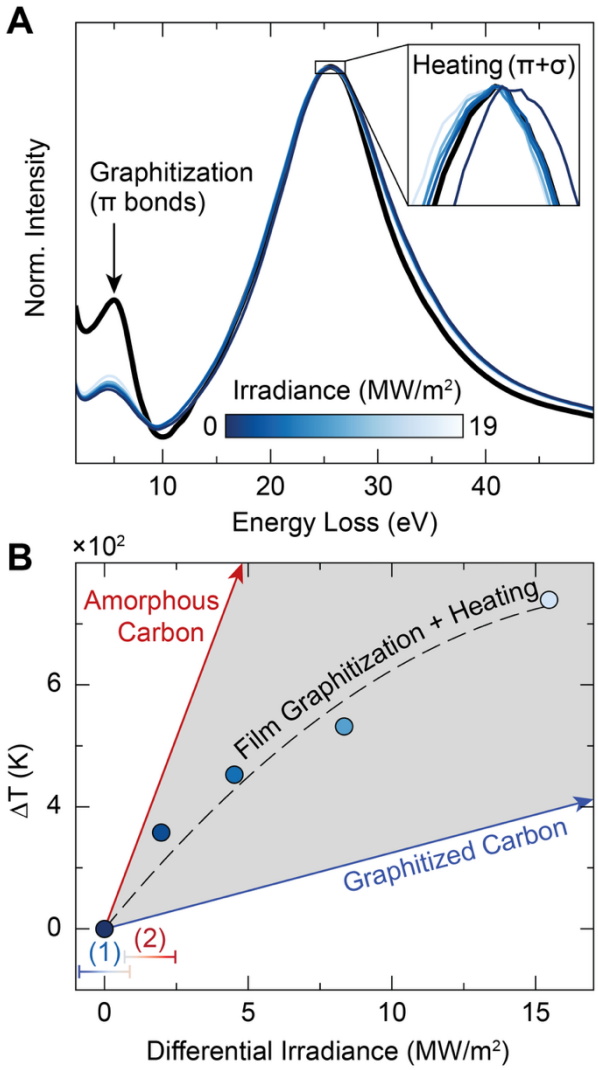

Figure 5.1. Irradiance-dependent plasmon thermometry of the a-C support film. (**A**) Low-loss EELS of the a-C support film acquired during 375 nm light illumination. The black spectrum of the film is measured at 0 MW/m^2 following a prior graphitization step induced by 155 MW/m^2 irradiance (not shown). The inset highlights the π+σ plasmon peak's redshift associated with film heating. (**B**) Plasmon thermometry of the support film compared with modeled heating for a-C and graphitized carbon. The trend indicates progressive support film graphitization and heating during illumination. Differential irradiance excludes the first data point (0 MW/m^2) because initial light exposure produced irreversible carbon removal. Labels indicate irradiance ranges that induce (1) water evaporation and (2) cell implosion during LPTEM, respectively.

We performed thermal modeling and plasmon thermometry to interpret photothermal heating in the a-C film (**Fig. 5.1B**). A Beer–Lambert-type expression was used to estimate heat accumulation in the film for fixed thermal conductivities (see Supporting Information). We model a wide range of plausible conductivity values because the thermal conductivity of a-C can vary from <1 $W \cdot m^{-1} \cdot K^{-1}$ for hydrogenated a-C:H to 10 $W \cdot m^{-1} \cdot K^{-1}$ for tetrahedral a-C (**Fig. 5.1B**).[24] This conductivity range predicts a photothermal temperature rise of approximately 400 to 4,000 K at the modeled irradiance, highlighting the potentially large variation in thermal response during optically coupled LPTEM. We then used plasmon thermometry to quantify the film temperature as a function of laser irradiance by tracking the $\pi+\sigma$ peak's redshift (**Fig. 5.1A**, inset).[25] Plasmon energy expansion thermometry relies on thermal expansion to quantify temperature induced by a resistive heater or in situ.[17,18,25,26] From plasmon thermometry, we find that the film reaches ~1000 ± 200 K, where the uncertainty arises primarily from the unknown extent of graphitization. The measured irradiance-dependent temperature trend is nonlinear because of progressive a-C graphitization at elevated temperature.[27–29] Although graphitization could ultimately mitigate heating because graphite has a much higher thermal conductivity, the heating and restructuring processes nevertheless led first to water pocket evaporation in range (1) and then to cell implosion in range (2) at the irradiances indicated in **Fig. 5.1B**.[30]

It is important to note that illumination produces a strongly nonuniform temperature distribution across larger a-C windows. The magnitude of this thermal gradient depends on the distance from the illumination region at the image center to the nearest Au grid bar, which acts as the primary heat sink. The thermal model in **Fig. 5.1B** treats the system as a 50 μm diameter, 50 nm thick circular a-C window bounded by a perfect heat sink. Although this model simplifies the true LPTEM geometry, the associated uncertainty is smaller than the order-of-magnitude variation in thermal behavior introduced by graphitization. Plasmon thermometry spectra in **Fig. 5.1** were acquired with the laser focused at the center of the window, whereas optically coupled LPTEM experiments probed water pockets located at variable distances from the Au grid bars. Consequently, the local temperature experienced

by an individual water pocket may differ significantly from the temperature of a-C measured at the center of the window.

Photothermal heating induces water pocket evaporation and cell implosion during optically coupled LPTEM (**Fig. 5.2**). To quantify the light-induced water evaporation rate, we track the water pocket's area during light illumination to relate irradiance to evaporation dynamics (see Supporting Information). The ~10 μm laser diameter at the specimen is notably larger than the field-of-view used for time-resolved imaging in this work. Water appears as dark contrast in bright-field images because it strongly scatters the electron beam (**Fig. 5.2A**). We fit the water's dark contrast in each frame of a time-resolved water evaporation movie under 5.5 MW/m^2 light irradiance until the cell implodes (**Fig. 5.2B**). By monitoring the liquid pocket area over time, we quantify how light illumination induces water evaporation (**Fig. 5.2C**). The water pocket area is stable during imaging alone, and our area fits indicate a 3% decrease of the water area in the first 16 s without light illumination. Once the water pocket is illuminated, heating causes the water pocket to shrink as it evaporates over the next 15 s. Movies of water evaporation and image analysis are in Supplementary Videos 1 and 2.

We similarly analyze the water evaporation dynamics of two water pockets, now with variable light irradiance (**Fig. 5.2D–F**). These two pockets have different sizes—Pocket 1 has a larger water volume, nanoparticle aggregate clusters, and asymmetry as compared to Pocket 2 (**Fig. 5.2D**). We acquired bright-field images while the laser irradiance was first ramped from 0 – 5.5 MW/m^2, then shut off, and again turned on at 5.5 MW/m^2 until cell implosion. We again mask the image to track the boundaries of the water pockets as they evaporate (**Fig. 5.2E**). Tracking the water pockets' areas over time reveals distinct, pocket-specific dynamics (**Fig. 5.2F**). For example, Pocket 1 is slower to heat and cool when light illumination is turned on and off, respectively. Delayed heating and cooling could be caused by the larger water bath's higher thermal capacitance or its greater distance from the Au grid bar heat sink. Pocket 1 also evaporates at a faster rate. Although the laser irradiance that induced implosion was identical to that used to acquire **Fig. 5.2A–C**, the two-pocket

evaporation rate is slower because the water pockets in this latter case are closer to the Au grid bar and thus at a lower temperature.

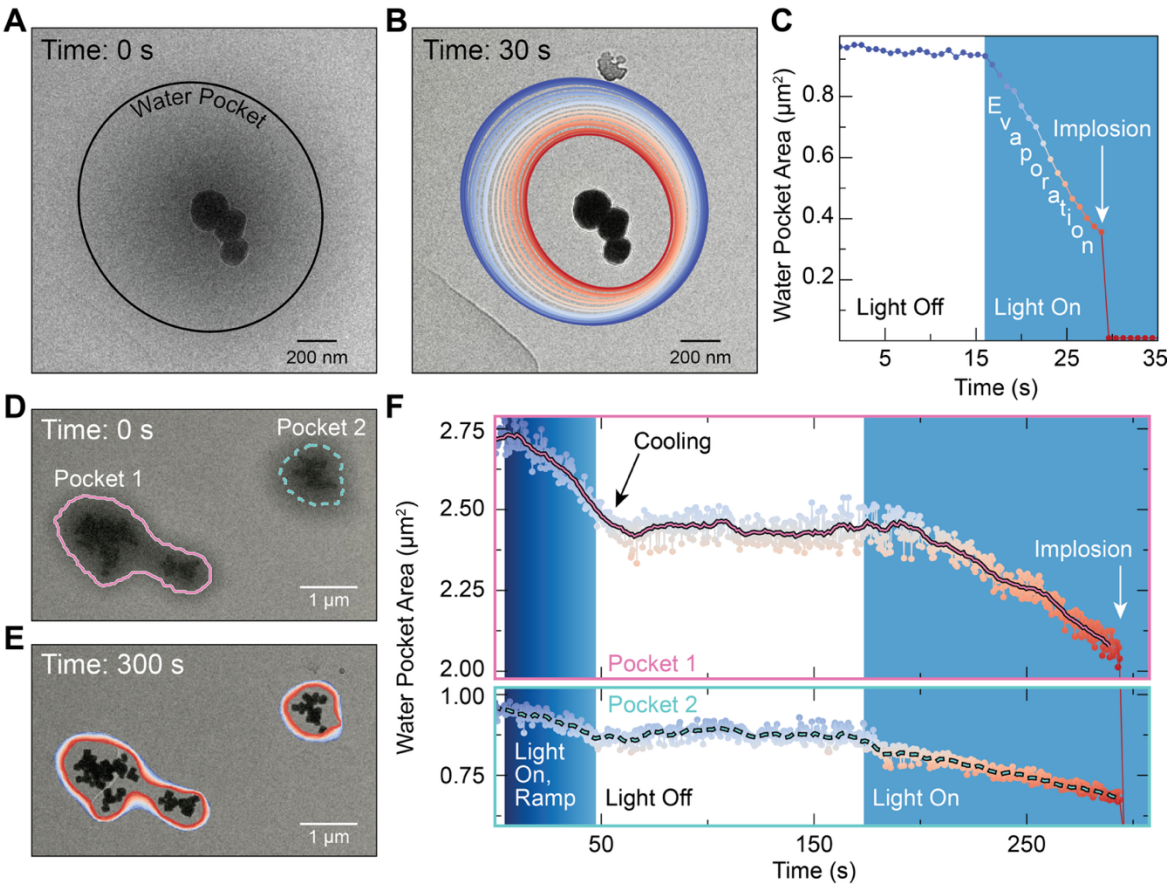

Figure 5.2. Time-resolved imaging of light-driven water evaporation. (**A**) A bright-field image of $SrTiO_3$:Al nanoparticles in a water pocket prior to illumination. (**B**) Evolution of the water pocket boundary during 5.5 MW/m^2 light irradiance overlaid on an image of the imploded cell. The color map corresponds to the fit water pocket area. (**C**) The water pocket area over time quantifies the light-driven water evaporation. Cell implosion occurs at the movie's ~30 s time point. (**D**) $SrTiO_3$:Al nanoparticles encapsulated in two water pockets prior to illumination. (**E**) The water pockets' boundaries are tracked during variable light illumination and overlaid on an image of the imploded cells. The color maps correspond to the water pockets' respective areas. (**F**) The water pocket areas over time quantify differences in light-driven water evaporation due to variable cell volume and irradiance. Movies of evaporation are in Supplementary Videos 1–3.

Water evaporation occurs at high temperatures produced during optically coupled LPTEM. These high temperatures result from absorption of ~60% of the 375 nm light by the 50 nm a-C support films. The membrane's temperature at the center of the window exceeds 1000 K because the a-C films implemented in this work are poor thermal conductors and tens of micrometers from a heat sink. This result underscores the critical need for liquid cell designs with proper thermal management for optically coupled and ultrafast LPTEM measurements. Key considerations for thermal management include the support film's composition, thickness, in-plane thermal conductivity, and wavelength-dependent absorptivity, along with the proximity of the region of interest to a heat sink. Few-layer graphene liquid cells are an optimal choice for optically coupled LPTEM due to their low light absorption and high in-plane thermal conductivity, but the graphene's stability under intense light illumination should be further characterized. SiN_x support films could be implemented but would require a heat sink within several micrometers of the specimen region of interest.

Although water strongly scatters the electron beam, in situ EELS during optically coupled LPTEM is able to image photocatalysts' nanoscale electronic properties in situ.[14] Low-loss EELS of catalysts in a liquid cell can access excitations below the 7 eV onset of the water plasmon, enabling measurement of inter- and intra-band transitions as well as plasmon resonances.[31–34] Core-loss edges of catalysts are also accessible, provided they do not overlap the oxygen K-edge. We implement low- and core-loss EELS of water during its evaporation to investigate methods to optimize future in situ EELS studies (**Fig. 5.3**).

As water in the cell evaporates with increasing laser irradiance, the water plasmon peak intensity counterintuitively increases (**Fig. 5.3A**). This increase arises because fewer zero-loss electrons undergo multiple inelastic scattering through water plasmon modes, thereby amplifying the relative intensity of both the ZLP and the singly scattered plasmon signal (see Figs. S7–9). At the ~300–600 nm water thickness, the spectral window below 7 eV remains accessible. The thickness of the a-C support film must also be considered in future experiments, since carbon low-loss peaks may obscure specimen dynamics of interest.

Thinner water pockets are therefore advantageous because they improve spectral resolution, increase the fraction of signal from the specimen, and enhance dose efficiency.

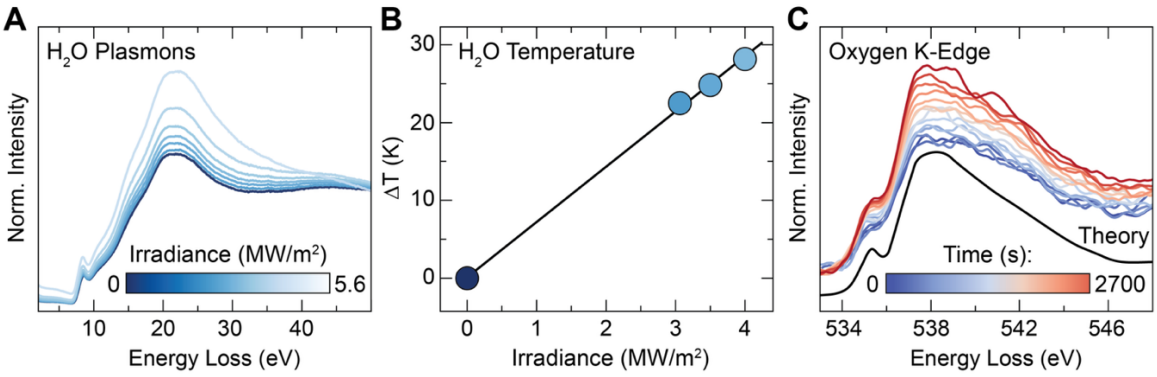

Figure 5.3. Plasmon thermometry and core-loss EELS during light-induced water evaporation. (**A**) Low-loss EELS of a water pocket while increasing the laser irradiance. Implosion occurs at 6.2 MW/m^2. (**B**) Plasmon thermometry of the 22 eV water plasmon at the first four irradiance values. (**C**) Time-resolved core-loss EELS of water's oxygen K edge during water evaporation resulting from fixed 5.1 MW/m^2 irradiance. The 1 s spectral acquisitions are averaged over 200 s increments and are smoothed for clarity. The theory spectrum is calculated with density functional theory, Bethe–Salpeter equation, and a GW many-pole self-energy correction, reproduced from ref.[35] Copyright 2012 American Physical Society.

We next performed plasmon thermometry on the liquid cell by fitting the irradiance-dependent water plasmon peak to quantify water temperature in situ (**Fig. 5.3B**). Plasmon thermometry under optical excitation has been performed on solids in vacuum, but it has not yet been expanded to LPTEM.[18,36] We measure an average water temperature increase of 20–30 K upon laser illumination. Although plasmon thermometry indicates only a 20–30 K increase in the average water temperature, this measurement does not capture the likely higher local temperature at the water–carbon interface, where heating is expected to be most intense. These water pockets are also only ~10 µm from the Au grid bars heat sink, mitigating water heating and evaporation. Only the first four spectra of water are analyzed because the

carbon peaks begin to influence the accuracy of thermometry as the water evaporates (Figs. S4, S9).

We also measure the water's oxygen K-edge during evaporation (**Fig. 5.3C**). Similar to our low-loss measurements, the core-loss signal increases with decreasing water volume. The core-loss spectral resolution also visibly increases as the water evaporates, approaching the theoretically calculated oxygen K-edge of water without multiple inelastic electron scattering.[35] These results further demonstrate the signal and resolution benefits of using thin liquid layers for optically coupled EELS in LPTEM. In addition, liquid thickness is tunable through laser-induced evaporation, which otherwise typically requires precise pressure controllers on SiN_x membrane cells .[37]

We further consider the mechanisms that may lead to liquid cell implosion. Implosion may occur through four pathways: (1), increasing strain on the evacuating cavity, (2) pocket-size-dependent internal pressure buildup, (3) implosion or fracture propagating from nearby pockets, and (4) graphitization and crack formation in the support film. As water evaporates and escapes, the evacuated cavity places increasing mechanical strain on the thin support membrane and can eventually initiate catastrophic failure. At the same time, the liquid cavity pressure increases nonlinearly as the water volume decreases.[38,39] During our evaporation and implosion measurements in **Fig. 5.2D–F** shown by Supplementary Video 3, neighboring water pockets collapsed before Pocket 1, suggesting that strain generated by nearby pockets may initiate another implosion event. Our a-C films also graphitize during light irradiance, observed both in the thermometry trend during our initial EELS measurements and during time-resolved imaging of water evaporation. After imaging the cell implosion, cracks and graphitic defects become apparent in the a-C films (**Figs. 5.2B,E**).

We lastly note that the unavoidable effects of electron beam radiolysis, damage, and heating were minimized by operating at low beam dose and current. We measure the water pockets using bright-field imaging mode with a parallel beam spot size larger than the water pocket diameter. During time-resolved imaging, the water pocket area did not decrease below the noise-level fluctuations when light illumination was off. Beam-induced heating during

plasmon thermometry was similarly minimized by acquiring spectra with a parallel beam at low magnification and a 1 μm probe size.

In conclusion, this work highlights the promise of optically coupled LPTEM for operando measurements during light-driven and photocatalytic processes. We measured light-induced thermal water evaporation and liquid pocket implosion for carbon film liquid cells. We implemented plasmon thermometry and photothermal modeling to quantify the potential temperature rise and graphitization of the illuminated a-C support films. We image liquid cells' water evaporation dynamics and expand plasmon thermometry to the liquid phase to quantify acqueous temperatures in situ. Our results underscore critical considerations for designing support films with adequate thermal dissipation for optically coupled LPTEM. Due to the high UV absorption coefficient of carbon, few-layer graphene membranes are effectively required for quantitative operando LPTEM with light illumination. Future studies will perform operando low-loss and core-loss EELS of photocatalytic nanomaterials, and these studies will benefit from tunable liquid thickness that are controlled by light-driven water evaporation.

5.3 Supporting Information

The supporting information—containing figures and data labelled S[X], methods and instrumentation details, laser alignment procedures, EELS thickness and thermometry calculations, photothermal temperature modeling, water pocket area fitting, EELS data, movies of water evaporation, descriptions of Supplementary Videos 1–3— is available free of charge at: https://doi.org/10.22002/wheak-c7d39

5.4 References

(1) Ham, Y.; Hisatomi, T.; Goto, Y.; Moriya, Y.; Sakata, Y.; Yamakata, A.; Kubota, J.; Domen, K. Flux-Mediated Doping of $SrTiO_3$ Photocatalysts for Efficient Overall Water Splitting. *J. Mater. Chem. A* **2015**, *4*. https://doi.org/10.1039/C5TA04843E.

(2) Takata, T.; Jiang, J.; Sakata, Y.; Nakabayashi, M.; Shibata, N.; Nandal, V.; Seki, K.; Hisatomi, T.; Domen, K. Photocatalytic Water Splitting with a Quantum Efficiency of Almost Unity. *Nature* **2020**, *581* (7809), 411–414. https://doi.org/10.1038/s41586-020-2278-9.

(3) Kikuchi, E.; Saito, N.; Yamaguchi, Y.; Kudo, A. Temperature Dependence of Photocatalytic Water Splitting under Visible Light Irradiation over Ir- and Sb-Codoped $SrTiO_3$:Al. *J. Phys. Chem. C* **2025**, *129* (5), 2381–2390. https://doi.org/10.1021/acs.jpcc.4c07699.

(4) Wilson, A. A.; Moss, B.; Riaz, A. A.; Kalha, C.; Thakur, P. K.; Lee, T.-L.; Regoutz, A.; Takata, T.; Hisatomi, T.; Domen, K.; Durrant, J. R. Long-Lived Hole Accumulation in Al:$SrTiO_3$/Rh–Cr Photocatalyst Systems under Continuous Irradiation and Its Correlation with Overall Water Splitting Efficiency. *J. Am. Chem. Soc.* **2025**, *147* (38), 34438–34448. https://doi.org/10.1021/jacs.5c07521.

(5) Askarova, G.; Xiao, C.; Barman, K.; Wang, X.; Zhang, L.; Osterloh, F. E.; Mirkin, M. V. Photo-Scanning Electrochemical Microscopy Observation of Overall Water Splitting at a Single Aluminum-Doped Strontium Titanium Oxide Microcrystal. *J. Am. Chem. Soc.* **2023**, *145* (11), 6526–6534. https://doi.org/10.1021/jacs.3c00663.

(6) Wang, Z.; Toyoshima, R.; Yoshida, M.; Mase, K.; Kondoh, H. In Situ Observation of Charge Transfer in the Cocatalyst-Loaded SrTiO3:Al Photocatalyst under UV Irradiation by Conversion-Electron-Yield Soft-X-Ray Absorption Spectroscopy. *J. Phys. Chem. C* **2024**, *128* (22), 9193–9201. https://doi.org/10.1021/acs.jpcc.4c02195.

(7) Hauwiller, M. R.; Ondry, J. C.; Chan, C. M.; Khandekar, P.; Yu, J.; Alivisatos, A. P. Gold Nanocrystal Etching as a Means of Probing the Dynamic Chemical Environment in Graphene Liquid Cell Electron Microscopy. *J. Am. Chem. Soc.* **2019**, *141* (10), 4428–4437. https://doi.org/10.1021/jacs.9b00082.

(8) Yesibolati, M. N.; Mortensen, K. I.; Sun, H.; Brostrøm, A.; Tidemand-Lichtenberg, S.; Mølhave, K. Unhindered Brownian Motion of Individual Nanoparticles in Liquid-Phase Scanning Transmission Electron Microscopy. *Nano Lett.* **2020**, *20* (10), 7108–7115. https://doi.org/10.1021/acs.nanolett.0c02352.

(9) Wang, W.; Xu, T.; Chen, J.; Shangguan, J.; Dong, H.; Ma, H.; Zhang, Q.; Yang, J.; Bai, T.; Guo, Z.; Fang, H.; Zheng, H.; Sun, L. Solid–Liquid–Gas Reaction Accelerated by Gas Molecule Tunnelling-like Effect. *Nat. Mater.* **2022**, *21* (8), 859–863. https://doi.org/10.1038/s41563-022-01261-x.

(10) Mohan, M. K. Nanobubble Dynamics Studied with Transmission Electron Microscopy, Nanyang Technological University. Ph.D. Dissertation, Nanyang Technological University, 2016. https://doi.org/10.32657/10356/69008.

(11) Hirokawa, S.; Teshima, H.; Solís-Fernández, P.; Ago, H.; Tomo, Y.; Li, Q.-Y.; Takahashi, K. Nanoscale Bubble Dynamics Induced by Damage of Graphene Liquid Cells. *ACS Omega* **2020**, *5* (19), 11180–11185. https://doi.org/10.1021/acsomega.0c01207.

(12) Shin, D., Park, J., Kim, YJ. et al. Growth dynamics and gas transport mechanism of nanobubbles in graphene liquid cells. *Nat. Commun.* **2015**, *6* (1), 6068. https://doi.org/10.1038/ncomms7068.

(13) Yin, Z.-W.; Betzler, S. B.; Sheng, T.; Zhang, Q.; Peng, X.; Shangguan, J.; Bustillo, K. C.; Li, J.-T.; Sun, S.-G.; Zheng, H. Visualization of Facet-Dependent Pseudo-Photocatalytic Behavior of TiO_2 Nanorods for Water Splitting Using In Situ Liquid Cell TEM. *Nano Energy* **2019**, *62*, 507–512. https://doi.org/10.1016/j.nanoen.2019.05.068.

(14) Lu, Y.; Yin, W.-J.; Peng, K.-L.; Wang, K.; Hu, Q.; Selloni, A.; Chen, F.-R.; Liu, L.-M.; Sui, M.-L. Self-Hydrogenated Shell Promoting Photocatalytic H_2 Evolution on Anatase TiO_2. *Nat. Commun.* **2018**, *9* (1), 2752. https://doi.org/10.1038/s41467-018-05144-1.

(15) Yu, S.; Jiang, Y.; Sun, Y.; Gao, F.; Zou, W.; Liao, H.; Dong, L. Real Time Imaging of Photocatalytic Active Site Formation during H_2 Evolution by In-Situ TEM. *Appl. Catal. B Environ.* **2021**, *284*, 119743. https://doi.org/10.1016/j.apcatb.2020.119743.

(16) Fu, X.; Chen, B.; Tang, J.; Zewail, A. H. Photoinduced Nanobubble-Driven Superfast Diffusion of Nanoparticles Imaged by 4D Electron Microscopy. *Sci. Adv.* **2017**, *3* (8), e1701160. https://doi.org/10.1126/sciadv.1701160.

(17) Palmer, L. D.; Lee, W.; Durham, D. B.; Fajardo, J. Jr.; Liu, Y.; Talin, A. A.; Gage, T. E.; Cushing, S. K. Nanoscale and Element-Specific Lattice Temperature Measurements Using Core-Loss Electron Energy-Loss Spectroscopy. *ACS Phys. Chem. Au* **2025**, *5* (6), 589–598. https://doi.org/10.1021/acsphyschemau.5c00044.

(18) Castioni, F.; Auad, Y.; Blazit, J.-D.; Li, X.; Woo, S. Y.; Watanabe, K.; Taniguchi, T.; Ho, C.-H.; Stéphan, O.; Kociak, M.; Tizei, L. H. G. Nanosecond Nanothermometry in an Electron Microscope. *Nano Lett.* **2025**, *25* (4), 1601–1608. https://doi.org/10.1021/acs.nanolett.4c05692.

(19) Kaiya, K.; Ueki, Y.; Kawamoto, H.; Watanabe, K.; Yoshino, S.; Yamaguchi, Y.; Kudo, A. Water Splitting over Transition Metal-Doped $SrTiO_3$ Photocatalysts with Response to Visible Light up to 660 nm. *Chem. Sci.* **2024**, *15* (39), 16025–16033. https://doi.org/10.1039/D4SC03978E.

(20) Lee, T. H.; Lee, S.; Yuan, L.; Dionne, J. A.; Park, J. Integrative Approaches to Reveal Catalyst Dynamics: Bridging Operando Techniques, Theory, and Artificial Intelligence. *ACS Nano* **2025**, *19* (42), 36827–36844. https://doi.org/10.1021/acsnano.5c10976.

(21) Sung, J.; Bae, Y.; Park, H.; Kang, S.; Choi, B. K.; Kim, J.; Park, J. Liquid-Phase Transmission Electron Microscopy for Reliable In Situ Imaging of Nanomaterials. *Annu. Rev. Chem. Biomol. Eng.* **2022**, *13*, 167–191. https://doi.org/10.1146/annurev-chembioeng-092120-034534.

(22) Nelson, F. J.; Idrobo, J.-C.; Fite, J. D.; Mišković, Z. L.; Pennycook, S. J.; Pantelides, S. T.; Lee, J. U.; Diebold, A. C. Electronic Excitations in Graphene in the 1–50 eV Range: The π and π + σ Peaks Are Not Plasmons. *Nano Lett.* **2014**, *14* (7), 3827–3831. https://doi.org/10.1021/nl500969t.

(23) Hopf, C.; Angot, T.; Aréou, E.; Dürbeck, T.; Jacob, W.; Martin, C.; Pardanaud, C.; Roubin, P.; Schwarz-Selinger, T. Characterization of Temperature-Induced Changes in Amorphous Hydrogenated Carbon Thin Films. *Diamond Relat. Mater.* **2013**, *37*, 97–103. https://doi.org/10.1016/j.diamond.2013.05.004.

(24) Robertson, J. Diamond-like Amorphous Carbon. *Mater. Sci. Eng. R Rep.* **2002**, *37* (4), 129–281. https://doi.org/10.1016/S0927-796X(02)00005-0.

(25) Marques, F. C.; Lacerda, R. G.; Champi, A.; Stolojan, V.; Cox, D. C.; Silva, S. R. P. Thermal Expansion Coefficient of Hydrogenated Amorphous Carbon. *Appl. Phys. Lett.* **2003**, *83* (15), 3099–3101. https://doi.org/10.1063/1.1619557.

(26) Mecklenburg, M.; Hubbard, W. A.; White, E. R.; Dhall, R.; Cronin, S. B.; Aloni, S.; Regan, B. C. Nanoscale Temperature Mapping in Operating Microelectronic Devices. *Science* **2015**, *347* (6222), 629–632. https://doi.org/10.1126/science.aaa2433.

(27) Nistor, L. C.; Van Landuyt, J.; Ralchenko, V. G.; Kononenko, T. V.; Obraztsova, E. D.; Strelnitsky, V. E. Direct Observation of Laser-Induced Crystallization of a-C:H Films. *Appl. Phys. A* **1994**, *58* (2), 137–144. https://doi.org/10.1007/BF00332170.

(28) Cappelli, E.; Scilletta, C.; Orlando, S.; Valentini, V.; Servidori, M. Laser Annealing of Amorphous Carbon Films. *Appl. Surf. Sci.* **2009**, *255* (10), 5620–5625. https://doi.org/10.1016/j.apsusc.2008.10.062.

(29) Grigonis, A.; Medvid, A.; Onufrijevs, P.; Babonas, J.; Rėza, A. Graphitization of Amorphous Diamond-like Carbon Films by Laser Irradiation. *Opt. Mater.* **2008**, *30* (5), 749–752. https://doi.org/10.1016/j.optmat.2007.02.027.

(30) Marsden, B.; Mummery, A.; Mummery, P. Modelling the Coefficient of Thermal Expansion in Graphite Crystals: Implications of Lattice Strain Due to Irradiation and Pressure. *Proc. R. Soc. A.* **2018**, *474* (2218), 20180075. https://doi.org/10.1098/rspa.2018.0075.

(31) Holtz, M. E.; Yu, Y.; Gao, J.; Abruña, H. D.; Muller, D. A. In Situ Electron Energy-Loss Spectroscopy in Liquids. *Microanal.* **2013**, *19* (4), 1027–1035. https://doi.org/10.1017/S1431927613001505.

(32) Serra-Maia, R.; Kumar, P.; Meng, A. C.; Foucher, A. C.; Kang, Y.; Karki, K.; Jariwala, D.; Stach, E. A. Nanoscale Chemical and Structural Analysis during In Situ Scanning/Transmission Electron Microscopy in Liquids. *ACS Nano* **2021**, *15* (6), 10228–10240. https://doi.org/10.1021/acsnano.1c02340.

(33) Keskin, S.; Pawell, C.; de Jonge, N. Verification of Water Presence in Graphene Liquid Cells. *Micron* **2021**, *149*, 103109. https://doi.org/10.1016/j.micron.2021.103109.

(34) Firlar, E.; Ouy, M.; Bogdanowicz, A.; Covnot, L.; Song, B.; Nadkarni, Y.; Shahbazian-Yassar, R.; Shokuhfar, T. Investigation of the Magnetosome Biomineralization in Magnetotactic Bacteria Using Graphene Liquid Cell – Transmission Electron Microscopy. *Nanoscale* **2019**, *11* (2), 698–705. https://doi.org/10.1039/C8NR08647H.

(35) Vinson, J.; Kas, J. J.; Vila, F. D.; Rehr, J. J.; Shirley, E. L. Theoretical Optical and X-Ray Spectra of Liquid and Solid H_2O. *Phys. Rev. B* **2012**, *85* (4), 045101. https://doi.org/10.1103/PhysRevB.85.045101.

(36) Palmer, L. D.; Lee, W.; Prasad, P. R.; Layne, B. W.; Chen, Z.; Watanabe, K.; Wen, J.; Liu, Y.; Wu, H. H.; Pan, X.; Talin, A. A.; Kudo, A.; Ardo, S.; Patterson, J. P.; Gage, T. E.; Cushing, S. K. Imaging Nanoscale Photocarrier Traps in Solar Water-Splitting Catalysts. Ver. 1. *arXiv*, Dec 31, 2025. https://doi.org/10.48550/arXiv.2512.24543.

(37) Keskin, S.; Kunnas, P.; de Jonge, N. Liquid-Phase Electron Microscopy with Controllable Liquid Thickness. *Nano Lett.* **2019**, *19* (7), 4608–4613. https://doi.org/10.1021/acs.nanolett.9b01576.

(38) Vasu, K. S.; Prestat, E.; Abraham, J.; Dix, J.; Kashtiban, R. J.; Beheshtian, J.; Sloan, J.; Carbone, P.; Neek-Amal, M.; Haigh, S. J.; Geim, A. K.; Nair, R. R. Van Der Waals Pressure and Its Effect on Trapped Interlayer Molecules. *Nat. Commun.* **2016**, *7* (1), 12168. https://doi.org/10.1038/ncomms12168.

(39) Hirokawa, S.; Teshima, H.; Solís-Fernández, P.; Ago, H.; Li, Q.-Y.; Takahashi, K. Random but Limited Pressure of Graphene Liquid Cells. *Ultramicroscopy* **2023**, *250*, 113747. https://doi.org/10.1016/j.ultramic.2023.113747.